Alma Mater Studiorum – University of Bologna

School of Science
Department of Physics and Astronomy
Master Degree Programme in Astrophysics and Cosmology

Searching for megahalos in galaxy clusters of the LOFAR Two Meter Sky Survey

Graduation Thesis

Presented by:
Matteo Cianfaglione

Supervisor:
Prof. Annalisa Bonafede

Co-supervisor:
Dr. Virginia Cuciti

Academic Year 2023/2024
Graduation Date 29/10/2024 - Session III

This Thesis work was done as part of the research activity of the Istituto di Radioastronomia - Istituto Nazionale di Astrofisica (INAF) in Bologna.

Contents

Abstract

Galaxy Clusters are the most massive gravitationally bound objects in the universe. These structures host thousands of galaxies and are permeated by magnetic fields and filled with relativistic electrons that emit in the radio band through the synchrotron mechanism. When clusters merge, cosmic ray electrons are re-accelerated by shocks and turbulence that amplify the magnetic field, leading to the formation of diffuse radio emission, such as radio relics and radio halos.

In a recent study, Cuciti et al. (2022) analysed a sample of more than 300 clusters observed with the LOw Frequency ARray (LOFAR) and discovered, in four clusters, a new type of diffuse radio emission, which fills a volume that is around 30 times larger than the one occupied by radio halos and has a lower surface brightness. The brightness is almost constant on scales of the order of hundreds of kiloparsecs and fills the cluster volume at least up to half the virial radius. This large scale emission has been named megahalo. Due to the very low brightness distributed on large spatial scales, they are best observed at low resolutions, i.e. 1 or 2 arcminutes, and at very low frequencies due to their steep spectra ($\alpha > 1.6$ when the flux density S is $S(\nu) \propto \nu^{-\alpha}$).

The four megahalos known so far have been found among the most massive clusters of the survey, suggesting that there might be a dependence of the megahalo brightness on the cluster mass. In the same mass and redshift range, however, there are also four additional clusters where megahalos have not been detected. **The aim of this thesis is to investigate the presence of megahalos in these four clusters: Abell 2219, Abell 2390, Abell 1763 and Abell 2261.**

To search for diffuse emission in clusters, sources that are embedded or projected into the cluster must be removed, and then a new image with a lower resolution has to be made to increase the sensitivity towards low surface brightness emission. When a large number of clusters must me analysed, as in the case of the LOFAR survey, this process is done through pipelines and can lead to subtraction artifacts in the presence of strong or extended sources. This is the case for the clusters studied in this thesis. Hence, we had to do "ad-hoc" subtractions for the different targets to detect possible diffuse emission.

Through this work, we detected giant radio halos in every studied cluster, confirming the presence of the debated radio halo in Abell 2390 and detecting for the first time a giant halo in Abell 1763. For every radio halo we estimated the central brightness I_0 and effective radius r_e through the fit of an exponential function and then computed the flux densities and radio powers at 150 MHz and the emissivity at 1.4 GHz, comparing them with the average values of radio halos. We plotted the results in the radio power-mass diagram alongside the other known radio halos from the LOFAR Two Meter Sky Survey, finding consistency between our measured powers and the expected relation.

We discover a powerful megahalo in the cluster A2219, with a flux density $S_{150\ \mathrm{MHz}} = 130 \pm 82$ mJy and a luminosity $P_{150\ \mathrm{MHz}} = (2.3 \pm 1.4) \cdot 10^{25}$ W/Hz. We also estimated the 5 SNR upper limit to the megahalo in the clusters Abell 2390 and Abell 2261, finding flux densities values comparable to the ones of observed megahalos, being $S_{150\ \mathrm{MHz}} = 106$ mJy and $S_{150\ \mathrm{MHz}} = 126$ mJy.

Finally, we investigated the position of all the detected megahalos in the radio power-mass diagram, finding hints of an increase of luminosity with the cluster mass, even though the statistics is still poor.

This thesis is organized in 7 Chapters:

1. in **Chapter 1** we introduce the main properties of galaxy clusters that can be estimated through the observation of thermal emission;
2. in **Chapter 2** we describe the non-thermal components present in clusters and classify the different diffuse radio emission that can be present;
3. in **Chapter 3** we describe the aim of this work and report the literature information of each target of the study;
4. in **Chapter 4** we briefly describe the LOFAR telescope, the survey from which our data are taken and make a short introduction to radio interferometry;
5. in **Chapter 5** we describe thoroughly the approach followed to produce the images and the data analysis, followed by the presentation of the results, such as flux density, luminosity and emissivity of the diffuse emission;
6. in **Chapter 6** we focus on the discussion of all the results obtained from the analysis, comparing them with literature data and investigating the possible existence of a radio power-mass relation for megahalos;
7. **Chapter 7** is the closing Chapter of the thesis. Here we summarize the entire work done alongside with the results. We also report our future prospects to continue the research on megahalos.

Chapter 1

Galaxy Clusters

Galaxy Clusters (GC) are the most massive gravitationally bound objects in the universe, with masses of the order of $M \sim 10^{14} - 10^{15}$ $M_\odot$ and virial radii of $R_{vir} \sim 1 - 3$ Mpc. These structures host from hundreds to thousands of galaxies, with dispersion velocities of the order of $\sigma_v \sim 1000$ km/s, and hot diffuse gas called Intra-Cluster Medium (ICM), with densities $n \sim 10^{-1} - 10^{-4}$ cm^{-3} and temperatures $T \sim 10^7 - 10^8$ K. Most of the mass is in the form of Dark Matter (DM, $\sim 80\%$) and the dominant baryonic component is the ICM ($\sim 15 - 17\%$), while the remaining mass is in form of galaxies and stars (Lin et al. 2003).

Clusters were firstly discovered in the optical band, since they are associations of galaxies, and were first classified by Abell (1958) based on their richness, morphology and compactness.

We can define the sound-crossing time, t_{cr}, as follows:

$$t_{cr} = \frac{R_{vir}}{\sigma_v} \approx 10^9 \text{ yr} \tag{1.1}$$

and since it is much shorter than the Hubble time ($\ll 13.7$ Gyr $= t_H$) and than the average cluster age at redshift $z = 0$ ($t_{age} \approx 10$ Gyr), we can say that clusters are gravitationally bound structures and we can get an estimate of the mass using the Virial Theorem:

$$M = \frac{3 R_{vir} \sigma_v^2}{G} \approx 10^{15} \left(\frac{\sigma_v}{10^3 \text{ km/s}} \right)^2 \left(\frac{R_{vir}}{1 \text{ Mpc}} \right) M_\odot \tag{1.2}$$

From the mass estimate of the Coma cluster, Zwicky (1933) found that, in order to obtain the observed dispersion velocities of galaxies, the average density should be 400 times greater than the one derived from observations, showing that dark matter exists in much larger quantities than luminous matter.

In the current cold dark matter (CDM) cosmological model (ΛCDM) the formation of clusters is explained through the collapse of the largest over-densities in the early Universe and the subsequent evolution happens through minor and major mergers with other clusters, forming the largest and most massive structures, as described in Kravtsov & Borgani (2012), this is also called the bottom-up scenario.
Mergers, and especially major mergers, are the most energetic events in the Universe after the Big Bang, releasing energies of the order of $E \sim 10^{63} - 10^{64}$ erg in a crossing time, causing turbulent motions and shocks in the ICM that heat the gas and are thought to be responsible for the (re-)acceleration of relativistic particles.

As we will see in the following sections, we can divide the emission in clusters in thermal and non-thermal emission (as shown in FIg. 1.1), adding layers to the complexity of these systems.

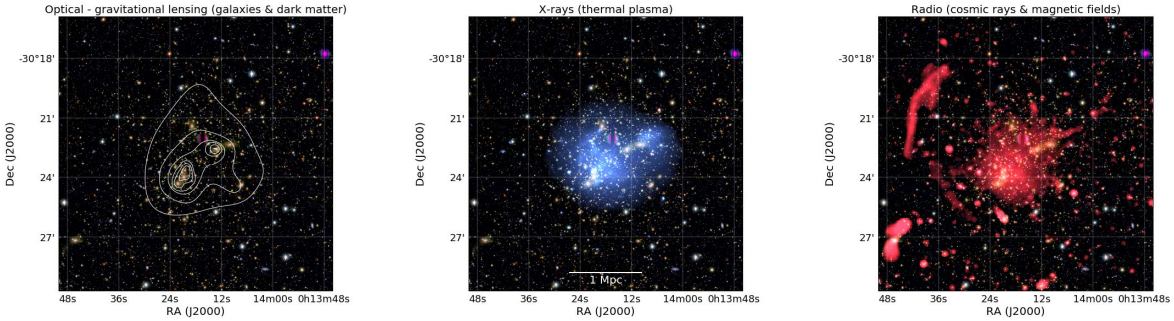

Figure 1.1: Composite images of the Abell 2744 galaxy cluster. *Left*: optical image (Subaru) of the cluster, the white contours represent the mass surface density derived from a weak lensing study. *Middle*: optical-X-ray (Chandra 0.5-2 keV band) composite image, the blue color shows the emission from the ICM. *Right*: optical-radio (Very Large Array (VLA), 1-4 GHz) composite image, with radio emission shown in red. From van Weeren et al. (2019).

1.1 Thermal emission in clusters

The thermal emission in clusters is produced by the gas of the ICM, in the soft X-ray band, and from galaxies emitting in the optical and infrared (IR) bands.
Optical observations can be used to classify different types of clusters (see Section 1.1.1) and to carry gravitational lensing studies to estimate the virial mass of the system (Section 1.2), to determine the mass distribution and to infer the dynamical properties (Section 1.3). High energy observations in the X-ray band can also be used to obtain the same properties, although through the exploitation of scaling relations for the mass and complex parameters to infer the dynamical state.
This highlights the importance of studying these objects through multi-wavelength observations to fully study every characteristic.

1.1.1 Abell classification

The first classification of GCs has been done by Abell (1958) when building the first galaxy cluster catalog by inspecting the Palomar Observatory Sky Survey. The catalog has been then expanded in Abell et al. (1989) by studying and classifying also the sources of the southern hemisphere. The classification is based on four parameters: richness class, morphology, compactness and distance.

The richness class defines an approximate number of galaxies present in the cluster, characterized by the number of objects within a magnitude range from m_3 to $m_3 + 2$, where m_3 is the magnitude of the third brightest member of the cluster. The richness is divided into six groups, going from *Group 0* with a number of galaxies between 30 and 49 up to *Group 5*, with a number of members greater than 299.

The compactness is based on the criterion that the number of galaxies must be > 50 in a "counting radius" (now known as Abell radius), which is defined as $R_A = 1.72/z$ arcmin, where z is the cluster's redshift. Most of Abell clusters are in a redshift range between $0.02 < z < 0.2$, even if there are some up to redshift $z = 0.4$.

Abell also made an optical classification of clusters based on morphology, dividing them into:

- regular clusters: virialized, relaxed and symmetric systems;
- irregular clusters: structures that are not relaxed with disturbed morphologies that do not show symmetries and that present substructures.

Another classification was proposed by Bautz & Morgan (1970), based on the emission from the Brightest Cluster Galaxy (BGC). They divided clusters in three main groups:

- type I: the cluster is dominated by a central Dominant (cD) elliptical galaxy;
- type II: the brightest members are intermediate in appearance between cD galaxies and normal giant ellipticals, it is an intermediate classification between type I and type III;
- type III: the cluster has no dominant galaxies.

Bahcall (1977) suggested another interesting classification between:

- cD clusters: regular and compact morphology and hints of mass segregation;
- spiral-rich clusters: irregular morphologies and little concentration, the distribution between elliptical and spiral galaxies is similar and there is no mass segregation;
- spiral-poor clusters: intermediate characteristics between cD and spiral-rich clusters.

Nowadays clusters are classified using other observational properties, based on observations also in other bands, as we will see in Section 1.3. This means that these historical classifications are not popular anymore.

1.1.2 X-ray emission

The X-ray emission in clusters comes from free electrons of the ICM emitting through bremsstrahlung processes. The X-ray luminosity ranges between $L_X \sim 10^{43}-10^{45}$ erg/s (Cimatti et al. 2019), making them the brightest X-ray sources in the Universe (alongside with Quasars). Galaxies and particles (ions and free electrons) are expected to move in the same gravitational potential, so if there is dynamical equilibrium we expect that the kinetic energy of the galaxies should be similar to the thermal energy of the gas. Thus, gas particles and galaxies should have a similar velocity dispersion. The kinetic energy of galaxies is $E_{kin} \approx m\sigma_v^2$ while the thermal energy of particles $E_{th} \approx kT$, hence assuming the equilibrium means that $\sigma_v \propto T^{1/2}$, from this we can estimate the average temperature of the gas:

$$kT \simeq \mu m_p \sigma_v^2 \simeq 6 \cdot \left(\frac{\sigma_v}{10^3 \text{ km/s}}\right)^2 \text{[keV]} \tag{1.3}$$

where m_p is the proton mass, k is the Boltzmann constant and μ is the mean molecular weight. Observations confirmed this relation, even if with some scatter, showing that the assumption is reasonable even if it is very simplistic.

As already said, the X-ray emission is due to the bremsstrahlung process, hence the monochromatic emissivity is given by:

$$j_\nu \propto T^{-1/2} n_e n_i g_{ff}(\nu, T) \exp(-h\nu/kT) \quad [\text{erg s}^{-1}\ \text{cm}^{-3}\ \text{Hz}^{-1}] \tag{1.4}$$

where n_e and n_i are the electron density and the ion density respectively and $g_{ff}(\nu, T) \propto \ln(kT/h\nu)$ is the Gaunt correction factor. Based on the exponential cut-off frequency in the continuum spectrum, we can estimate the temperature of the thermal plasma, giving us a relation between the two quantities. In clusters with ICM temperature $kT > 3$ keV the emission comes almost exclusively from the bremsstrahlung continuum, at lower temperatures, instead, emission lines from highly ionized metals give an important contribution to the total flux (e.g. the Fe-Kα). We can see an example of X-ray emission from the Coma cluster in the left image in Fig. 1.3.

1.1.3 Sunyaev-Zel'dovich effect

The ICM interacts with the cold photons from the Cosmic Microwave Background (CMB; $T \simeq 2.76$ K) through Inverse Compton (IC) scattering, producing the so called Sunyaev-Zel'dovich effect (SZE, Sunyaev & Zeldovich 1980), that causes a alteration of the Black Body spectrum, reducing the flux at frequencies lower than $\nu = 218$ GHz and increasing it at higher energies, as can be seen from Fig. 1.2.

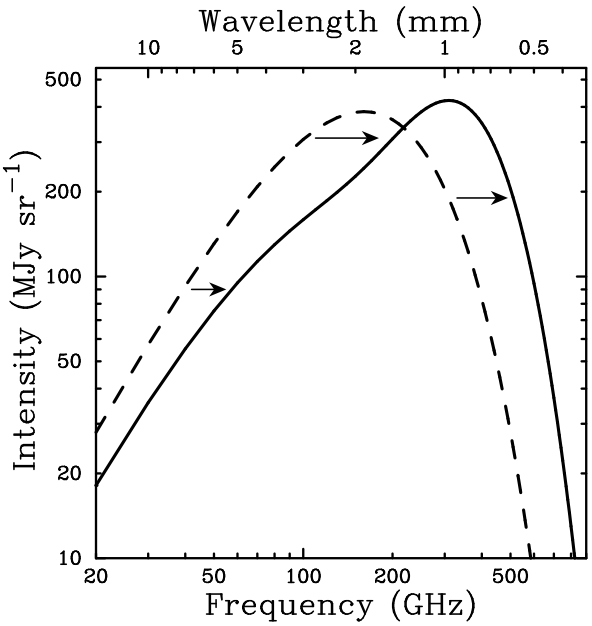

Figure 1.2: The undisturbed CMB spectrum (dashed line) compared with the modified spectrum (thick line) due to the SZE. This is a scheme derived from an idealized cluster with a mass 1000 times larger than the average cluster. From Carlstrom et al. (2002).

The intensity of the effect is determined by the Compton-y parameter, defined as:

$$y = \left(\frac{k\sigma_T}{m_e c^2}\right) \int_{los} n_e T_e \mathrm{d}l \tag{1.5}$$

where σ_T is the Thomson cross section, m_e is the electron mass and T_e is the gas temperature. This can be applied only to spatially resolved clusters, the value is

computed along the line of sight and for hot systems ($T \sim 10$ keV) has a value of $y \approx 10^{-4}$ (Carlstrom et al. 2002).
When it is not possible to spatially resolve the cluster through the SZE observation or if the total effect is needed, it is possible to compute the integrated Compton Y-parameter:

$$Y = \left(\frac{k\sigma_T}{m_e c^2}\right) \int n_e T_e \mathrm{d}V \tag{1.6}$$

The relative decrement of flux in the low frequency region is given by:

$$\frac{\Delta I_\nu}{I_\nu} = -2y \tag{1.7}$$

showing that the SZE does not depend on the distance of the cluster but only on the temperature of the ICM, thus on the thermal energy of the electrons, which is related to the clusters' mass. In Fig. 1.3 we can see the SZ flux from the Coma cluster.

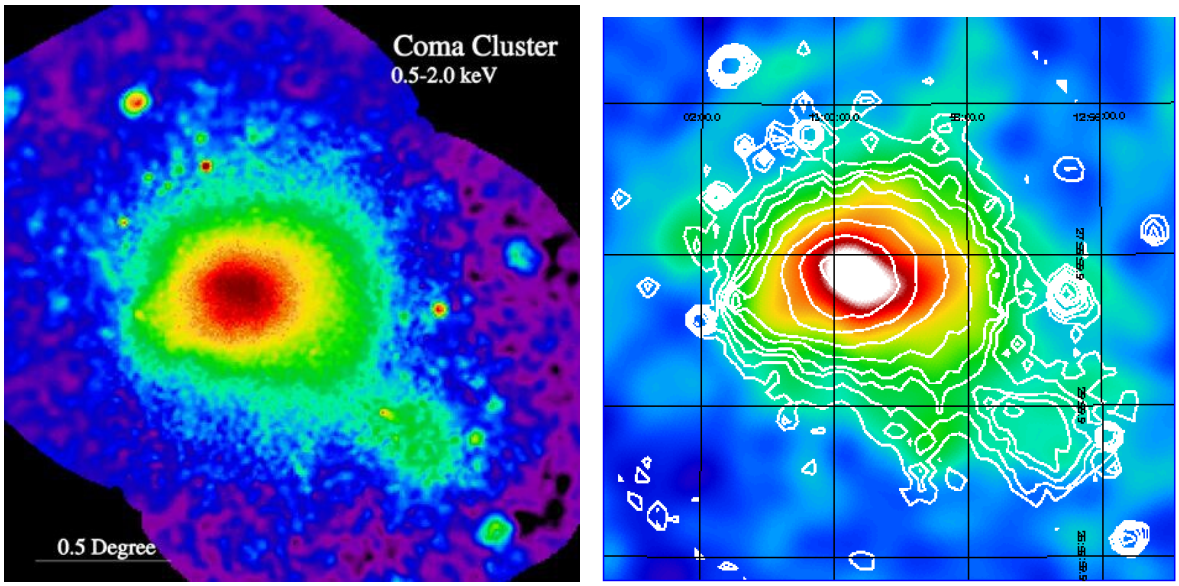

Figure 1.3: *Left*: X-ray view of the Coma cluster obtained with XMM-Newton in the 0.3 to 2.0 keV energy band (Briel et al. 2001, Neronov 2019). *Right*: Planck view of the Coma cluster with overlaid the contours from the ROSAT satellite (Planck Collaboration et al. 2011).

1.2 Mass estimates and scaling relations

In order to compute the mass of a cluster we can use different approaches and scaling relations, linking different properties of these systems. The first and most important approach is the application of the Virial Theorem to infer the virial mass, although it holds up only for relaxed clusters:

$$M_{vir} = \frac{3R_{vir}\sigma_v^2}{G} \approx 10^{15} \left(\frac{\sigma_v}{10^3 \text{ km/s}}\right)^2 \left(\frac{R_{vir}}{1 \text{ Mpc}}\right) \text{M}_\odot \tag{1.8}$$

where σ_v is the velocity dispersion of the galaxies and R_{vir} is the virial radius.

Another method, valid only for relaxed systems, is based on the assumption of hydrostatic equilibrium (Sarazin 1988, Vikhlinin et al. 2006):

$$\frac{\mathrm{d}P}{\mathrm{d}r} = -\frac{GM(r)}{r^2}\rho(r) \tag{1.9}$$

By retrieving the pressure from the equation of state of perfect gases, where $P = \rho kT/(\mu m_p)$, the mass inside a radius r is:

$$M(<r) = -\frac{kT(r)r}{G\mu m_p}\left(\frac{\mathrm{d}\ln\rho}{\mathrm{d}\ln r} + \frac{\mathrm{d}\ln T}{\mathrm{d}\ln r}\right) \tag{1.10}$$

If the gravitational potential is supporting both the galaxies and gas distribution, the radial density can be written through the β-model profile, proposed by Cavaliere & Fusco-Femiano (1978):

$$\rho_g(r) = \frac{\rho_0}{(1+(r/r_c)^2)^{3\beta/2}} \tag{1.11}$$

where ρ_0 is the central density, r_c is the core radius and $\beta = \mu m_p \sigma_v^2/(kT)$. The temperature profile, instead, is obtained by extracting X-ray profiles in annuli at different distances that are centered on the emission and then by estimating the temperature from the cut-off frequency of the bremsstrahlung emission (or from the flux of emission lines if the temperature is low enough).

A third way to estimate the mass of a cluster is to use strong and weak gravitational lensing studies to obtain the mass distribution (Bartelmann et al. 2003). The gravitational lensing phenomenon takes place when the light from background sources is deviated by the gravitational potential of an object, that acts like a lens, increasing the flux of the background source. The amount of the effect strictly depends on the mass of the lens. In general, and especially for clusters, when observing strong gravitational lensing, the main visual effect is the presence of galaxies that appear distorted, with elongated or arc-like shapes. Since clusters are the most massive structures in the Universe, they are also the best gravitational lenses that we can find (see Fig. 1.4), and thus the best case scenario to study the phenomenon and its effects, and to refine the mass estimates. By studying the weak and strong components of the lensing it is possible to produce an accurate bi-dimensional mass distribution of the lens.

Clusters' mass can also be estimated through various scaling relations with different parameters, such as ICM temperature T_X, ICM X-ray luminosity L_X and the Compton integrated Y-parameter (Arnaud et al. 2007, Arnaud et al. 2010, Planck Collaboration et al. 2014).
The first important scaling relation is found between the temperature T and the virial mass of the cluster M_{vir}, by assuming the virial equilibrium, hence from $\frac{3kT}{2\mu m_p} = \frac{GM_{vir}}{R}$, resulting in the following:

$$kT = 3.23\left(\frac{\mu}{0.6}\right)\left(\frac{\delta}{500}\right)\left(\frac{M}{10^{14}\ h^{-1}\ \mathrm{M}_\odot}\right)^{2/3}\ [\mathrm{keV}] \tag{1.12}$$

where δ is the average over-density with respect to the critical density of the Universe $\rho_c = \frac{3H(z)^2}{8\pi G}$ and $h = H_0/(100\ kms^{-1}\ Mpc^{-1})$.

A simpler relation for M_{500} was found by Finoguenov et al. (2001) and then extended for M_{2500} and M_{200} by Babyk & McNamara (2023), where in every case

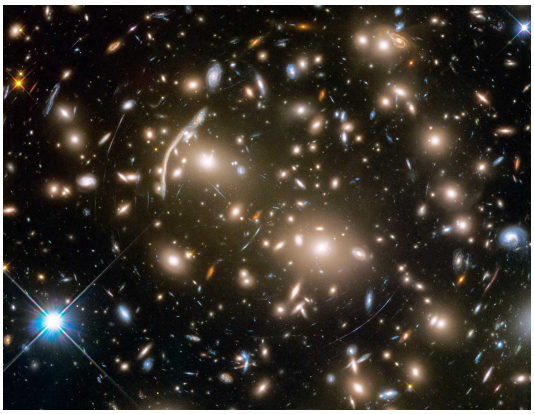

Figure 1.4: Image of the galaxy cluster Abell 370, taken with the Hubble Space Telescope. The image clearly shows the effects of the gravitational lensing on the background galaxies (with distorted arc-like shapes), while the bright elliptical galaxies are part of the cluster. Credits: NASA, ESA, and J. Lotz and the HFF Team (STScI).

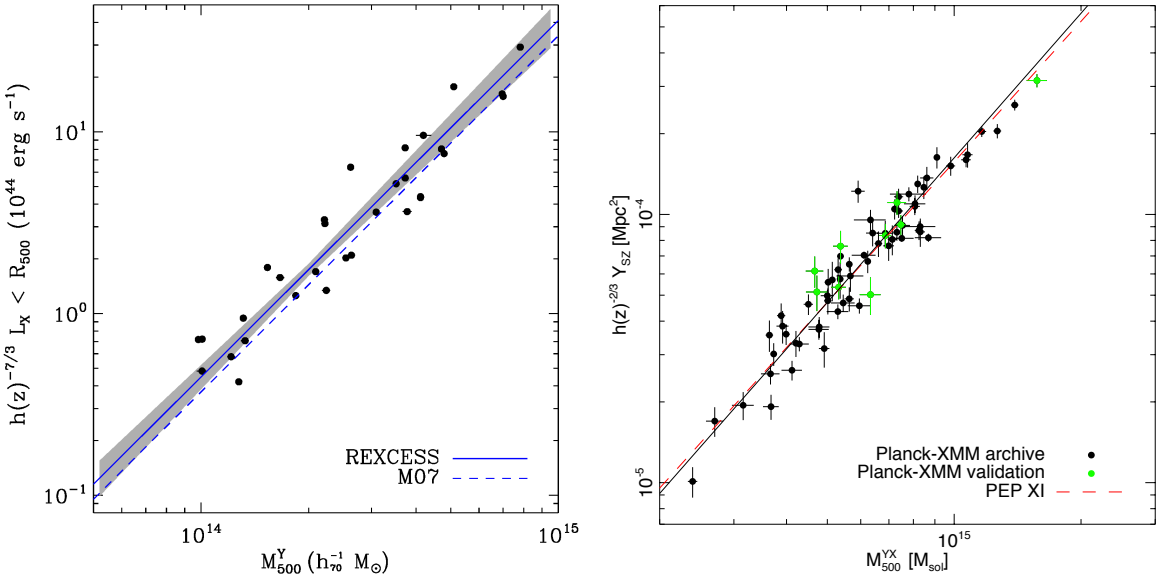

Figure 1.5: *Left*: $L_X - M_{500}$ relation found by Pratt et al. (2009). *Right*: $Y_{500} - M_{500}$ relation described in Planck Collaboration et al. (2014) using XMM-Newton archive data.

$M_\delta \propto T^{1.6}$, while for the virial mass Shimizu et al. (2003) found the relation to be $M_{vir} \propto T^{1.9}$.
X-ray observations from Pratt et al. (2009) (left panel in Fig. 1.5) have confirmed the presence of the scaling relation between L_X and M_{500}:

$$L_X = 1.33 \cdot 10^{43} \left(\frac{f_b}{0.1h^{-3/2}}\right)^2 \left(\frac{\mu}{0.6}\right)^{-1} \left(\frac{n}{10^{-3}\ h^2\ \mathrm{cm}^{-3}}\right) \times \\ \times \left(\frac{T}{keV}\right)^{0.4} \left(\frac{M}{10^{14}\ h^{-1}\ \mathrm{M}_\odot}\right) h^{-2}\ [\mathrm{erg/s}] \quad (1.13)$$

A relation is also present between the integrated Compton-y parameter Y_{500} (within

r_{500}[1]) and M_{500}[2], described by Planck Collaboration et al. (2014) (and shown in the right panel in Fig. 1.5):

$$E(z)^{-2/3}\left(\frac{D_A^2 Y_{500}}{10^{-4} Mpc^2}\right) = 10^{-0.175}\left(\frac{M_{500}}{6\cdot 10^{14}\ \mathrm{M}_\odot}\right)^{1.77} \tag{1.14}$$

where $E(z)^2 = \Omega_{m0}(1+z)^3 + (1-\Omega_{m0}-\Omega_{\Lambda 0})(1+Z)^2 + \Omega_{\Lambda 0}$ and D_A is the angular size of the source. This relation has also a smaller scatter with respect to the relation (1.13), therefore it is a better proxy of the mass.

The existence of these scaling relations proves the existence of the so called self-similar scenario (Peebles 1980), where it is assumed that clusters with different sizes are simply scaled version of each other, following the assumption that is the gravitational potential that is determining the properties of the ICM.

1.3 Dynamical properties

Although galaxy clusters can be approximated as relaxed systems, there are cases in which this assumption does not hold, like during major merger events. Major mergers are able to alter various characteristic properties of clusters such as the density profile, the average temperature of the ICM and the dynamical equilibrium.
Clusters can be divided into Cool-Core-Clusters (CCCs) and Non Cool-Core-Clusters (NCCCs) based on their central cooling times, which is related to the dynamical state; specifically Hudson et al. 2010 identified as threshold value $t_{cool} < 7.7$ Gyr. Cool-core clusters show a peaked density profile with a decrease of the temperature in the central region, also the entropy, defined as $K = kT/n_e^{2/3}$, shows a decrease in the same region. On the other hand, NCCCs have a smooth density profile with constant temperature and entropy in the central region (Arnaud et al. 2010, Ghirardini et al. 2017). The difference in the density and temperature profiles can be seen in Fig. 1.6.

1.3.1 Dynamical parameters and characterization

Alongside with temperature and density profiles, there are different ways to classify clusters based on their dynamical state.

Disturbed galaxy clusters show an asymmetric or irregular distribution of galaxies and gas, with substructures revealed by lensing (galaxies) and X-ray studies (gas). Gravitational lensing studies allow to properly identify these clumps in order to determine the merger history (Wen et al. 2024), while X-ray observations allow the determination of the dynamical state of clusters through the brightness distribution. Merging and post-merger clusters show an asymmetric and disturbed morphology, while cool-core clusters show a peaked X-ray distribution (Molendi & Pizzolato 2001, Wilber et al. 2019).

The classification can be also done through three parameters that are very sensitive to the presence of substructures: the surface brightness concentration c (Santos et al. 2008), the emission centroid shift w (Mohr et al. 1993) and the power ratio P_3/P_0 (Buote & Tsai 1996, Cassano et al. 2010, Cuciti et al. 2015, Yuan et al. 2022).

[1] r_{500} is the radius is the radius in which the average density is 500 times larger than the critical density of the Universe at the source redshift.

[2] M_{500} is the mass contained inside a sphere of radius r_{500}.

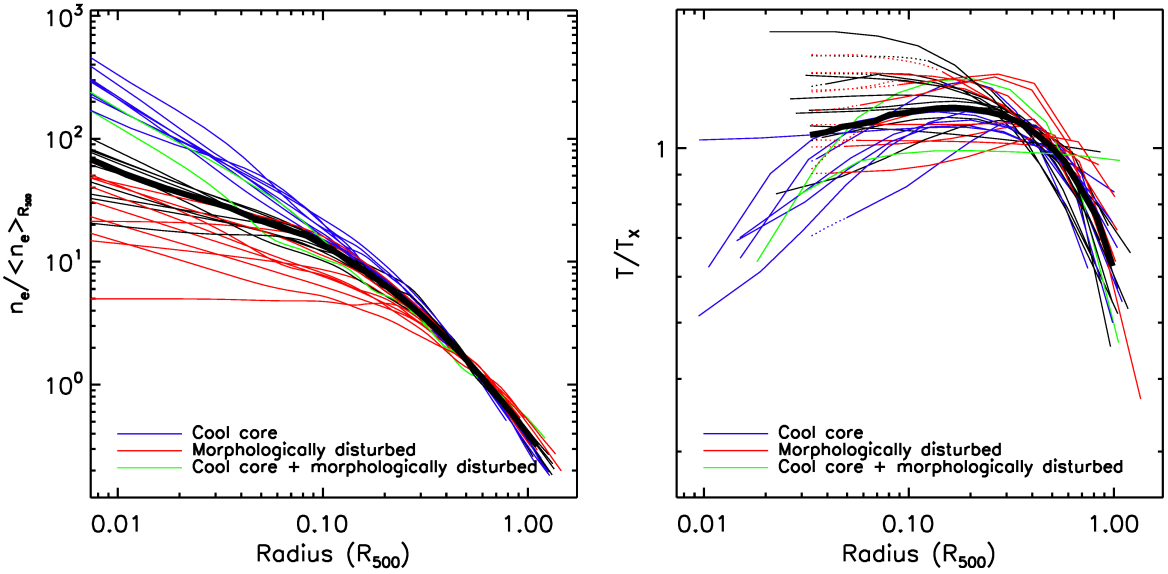

Figure 1.6: Scaled density (left) and temperature (right) profiles in function of the radii (in units of r_{500}) measured by Arnaud et al. (2010). The thick black lines are the average profiles, the blue lines show cool-core clusters while the red ones represent non cool-core clusters.

These parameters were firstly used by Santos et al. (2008) to classify high redshift clusters for which accurate spectroscopic analyses were not possible. The emission centroid shift was found to be very sensitive to the disturbed morphology of clusters, especially to the presence of sub-structures, by Poole et al. (2006) through numerical simulations.
The w-parameter is defined as the standard deviation of the projected separation between the X-ray peak and the centroid of the X-ray surface brightness measured in different apertures, with the expression being:

$$w = \frac{1}{R_{max}} \left(\frac{1}{N-1} \sum_i (\Delta_i - \langle \Delta \rangle)^2 \right)^{1/2} \tag{1.15}$$

where R_{max} is the radius of the maximum aperture, Δ_i is the distance between the peak of the emission and the center of the aperture.
The concentration parameter (also called light concentration parameter), c, is defined as the ratio of the surface brightness inside two concentric apertures:

$$c = \frac{S(r < r_1)}{S(r < r_2)} \tag{1.16}$$

where $r_2 > r_1$. As an example, in Cuciti et al. (2015), this has been defined as the ratio between the peak and the ambient surface brightness.
The power ratio is the multipole decomposition of the 2D mass distribution inside of a circular aperture of radius R_{ap}, centered on the brightness centroid. P_0 is defined as:

$$P_0 = a_0 \ln (R_{ap}) \tag{1.17}$$

where a_0 is the total intensity inside the aperture. The m-th term of the expansion is defined as:

$$P_m = \frac{1}{2m^2 R_{ap}^{2m}} (a_m^2 + b_m^2) \tag{1.18}$$

where:

$$a_m = \int_{R' \leq R_{ap}} S(x')(R') \cos(m\phi') \mathrm{d}^2 x' \tag{1.19}$$

$$b_m = \int_{R' \leq R_{ap}} S(x')(R') \sin(m\phi') \mathrm{d}^2 x' \tag{1.20}$$

Specifically, the ratio P_3/P_0 is sensitive to the presence of multiple X-ray peaks and substructures (Böhringer et al. 2010).

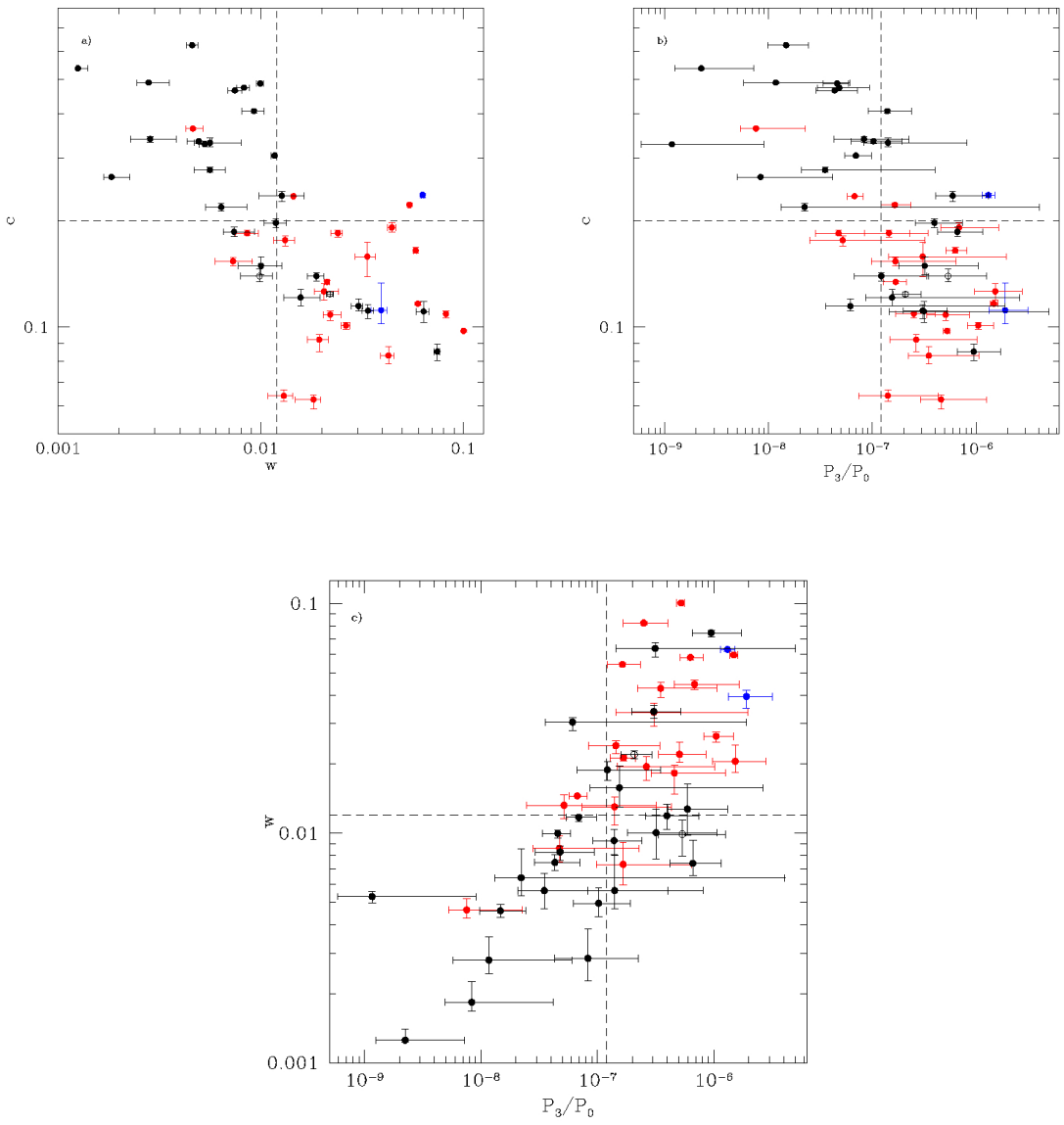

Figure 1.8: c-w, c-P_3/P_0 and w-P_3/P_0 plots for the sample of clusters studied by Cuciti et al. (2015). Red, black and blue dots represent clusters with radio halos, clusters without radio halos and clusters hosting relics (without radio halos), respectively.

By using these three parameters, Cassano et al. (2010) found an anti-correlation between c and w and between c and P_3/P_0, while there is a clear correlation between w and P_3/P_0 (see images in Fig. 1.8). The threshold values between CCCs and NCCCs are set at $c = 0.2$, $w = 0.012$ and $P_3/P_0 = 1.2 \cdot 10^{-7}$ in Cassano et al. (2010) and Cuciti et al. (2015), clusters close to these thresholds are often called warm-core clusters.

It is possible to combine the concentration and centroid shift parameters into a single parameter, the X-ray morphological disturbance (Cuciti et al. 2023). The disturbance is computed as the distance along the fitting line between the c and w parameters from the least disturbed cluster of a sample (which has a disturbance set = 0). The fitting line is defined as:

$$c_{norm} = m w_{norm} + q \tag{1.21}$$

where c_{norm} and w_{norm} are the normalized parameters, computed through the relation:

$$\mathcal{P}_{norm} = \frac{\log(\mathcal{P}_i) - \min(\log(\mathcal{P}))}{\max(\log(\mathcal{P})) - \min(\log(\mathcal{P}))} \tag{1.22}$$

The normalization allows us to take into account the different ranges of the two parameters.
Campitiello et al. (2022) defined a new dynamical parameter, called the M parameter, that combines the information included in the three dynamical parameters. This allows to build a sample from the least to the most disturbed clusters in a sample (hence it is a relative and not an absolute parameter), where relaxed clusters have low M values and disturbed clusters have high M values.

1.3.2 Cool-core clusters

As already discussed, the ICM radiates away its energy through bremsstrahlung processes, with a cooling time described by (Sarazin 1988):

$$t_{cool} \simeq 8.5 \cdot 10^{10} \left(\frac{n}{10^{-3}\ \mathrm{cm}^{-3}} \right)^{-1} \left(\frac{T}{10^{8}\ \mathrm{K}} \right)^{1/2} \ [\mathrm{yr}] \tag{1.23}$$

This time is usually longer than the Hubble time, although in relaxed clusters this can be much shorter in the central regions where the density peaks. Due to the higher emissivity and shorter cooling time, in the central region there is also a lower temperature, as seen in the profile in the right panel in Fig. 1.6.
From this shorter cooling time, Fabian (1994) suggested the presence of cold subsonic gas inflows in the central region, called cooling flows, that should deposit cold matter in the BCG, boosting the star formation and the mass growth, and since it is not hot gas anymore we can not observe it in the X-ray band, but it should be detectable through the Hα line. The first estimates and predictions from X-ray observations suggested a mass inflow rate of $\dot{M} \gtrapprox 500\ \mathrm{M}_\odot/\mathrm{yr}$. Bauer et al. (2005) found that the measured star formation rate and Hα fluxes can be explained by a gas cooling rate of only a few tens of $\mathrm{M}_\odot\ \mathrm{yr}^{-1}$, instead of the amount predicted at first by Fabian (1994) (see also Peterson et al. 2003). The low flux could be explained either by very slow and low cooling of gas or by the presence of conditions that allow long-lived Hα emission (Bauer et al. 2005). Hence the idea that there must be some mechanism or process that is continuously heating the ICM in the central regions slowing down or completely halting the gas cooling. The most accredited process is the so called AGN feedback from the cD galaxy (McNamara & Nulsen 2007), supported by the fact that many BCGs show signs of past or present AGN activity like jets, lobes (Best et al. 2007) and X-ray cavities filled with relativistic plasma (Churazov et al. 2002, Birzan et al. 2004, McNamara & Nulsen 2007), we can see an example in Fig. 1.9.

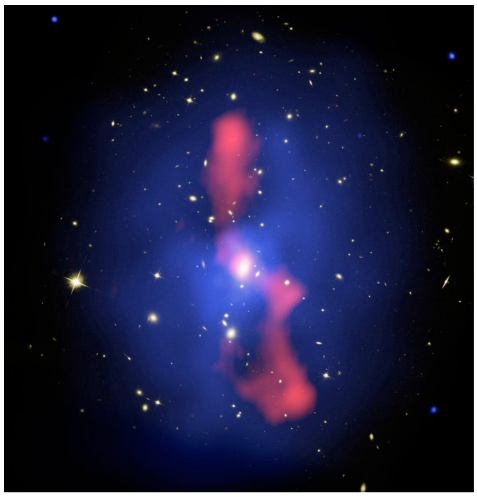

Figure 1.9: HST image of the cluster MS0735.6+7421, in red is the radio emission observed with the VLA at 330 MHz, in blue is the X-ray emission observed with Chandra. From McNamara & Nulsen (2007).

1.3.3 Non cool-core clusters

Non cool-core clusters have different X-ray properties from cool-core clusters and are strictly related to past and current mergers.

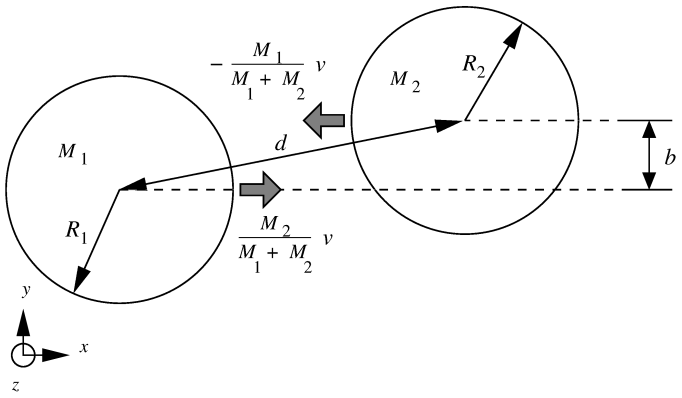

Figure 1.10: Simple schematic of a cluster merger between two clusters with masses M_1 and M_2. From Sarazin (2002).

As we explained before (see Section 1), mergers between clusters are very energetic events that can completely alter the dynamical state of clusters and their properties (Markevitch et al. 1999), like the ICM temperature and density distributions. As we have already seen, the gas temperature in non relaxed clusters is higher than in cool-core clusters, and the density profile is not peaked towards the centre.

In Fig. 1.10 shows a scheme of the kinematics of an idealized merger between two clusters, where M_1 and M_2 are the masses, R_1 and R_2 are the radii of the clusters, b is the impact parameter, d is the distance between the two clusters and v is the initial relative velocity. The collision velocity is the free fall velocity, given by:

$$v_{ff} \sim \sqrt{\frac{2GM}{R}} \sim 1000 \text{ km/s} \tag{1.24}$$

which is close to the sound speed of the ICM, c_s, hence the merger induces transonic gas motions, producing weak shocks, characterized by Mach numbers $\mathcal{M} \approx v_{ff}/c_s \approx \sqrt{2}$, this has also been confirmed by simulations (e.g. Ricker & Sarazin 2001). Simulations by Vazza et al. (2009) showed that shocks' Mach numbers can be higher in the outer regions, due to the lower gas density and temperature. Although shocks compress and heat the gas, leading to an increase in the X-ray emission, it is difficult to observe them in the outskirts of clusters due to the low X-ray brightness in these regions. This is combined with the fact that cluster shocks have low Mach numbers which cause only small jumps in density and temperature. This means that shocks can be detected only with very high sensitivity and angular resolution (e.g. by Chandra, Dasadia et al. 2016, Botteon et al. 2018). Moreover, such shocks can be observed if they have small angles with respect to the sky plane, otherwise projection effects can smooth out the emission, making it very difficult, if not impossible, to detect the jumps.

Mergers induce also turbulence in the ICM (Cassano & Brunetti 2005) that can be studied using cosmological simulations (e.g. Vazza et al. 2012) and traced through the broadening of emission lines from metals in the ICM. This can be done only with a very high spectral resolution (e.g. Hitomi and the future ATHENA space mission) and has been done only for the Perseus cluster by Hitomi Collaboration et al. (2016), in which it has been found a turbulent velocity broadening of $\Delta v = 160 \pm 16$ km/s. An indirect way to follow and characterize the turbulent motions of the gas has been found through the study of the density fluctuations obtained from the X-ray images (Zhuravleva et al. 2014). The results are similar to the ones from Hitomi Collaboration et al. (2016) and this relation has been further investigated through simulations (Simonte et al. 2022), confirming the presence of a connection between the two parameters.

Chapter 2

Non-thermal emission in clusters

Alongside with thermal emission, in galaxy clusters it is possible to observe non-thermal radio emission from radio galaxies. Some clusters also host diffuse radio sources not associated with individual galaxies. As we will see later in this Chapter, there are different classes of diffuse sources, covering a range of scales between a few hundreds of kpc up to a few Mpc. The main classes are:

- *radio halos*, thought to form from the turbulence injected by merger events;
- *mini halos*, their origin is still debated between turbulent acceleration of particles and proton-proton interactions producing high energy electrons;
- *radio relics*, trace merger shocks originated after major mergers, this hypothesis is favoured by their high polarization fraction;
- *phoenices* and *gently re-energized tails*, trace revived fossil AGN plasma;
- *radio bridges*, found between pairs of cluster connecting them, although the origin is unknown, the favoured scenario is the turbulent one;
- *megahalos*, these are large scale sources that cover the cluster volume at least up to r_{500}, their origin is still unknown and only four of them are known so far.

We will describe these sources more in detail in Section 2.3 alongside with their main properties. This non-thermal emission comes from synchrotron emitting electrons that are moving at relativistic speeds in the magnetic fields embedded in the ICM.
In this chapter we will focus on the description of the non-thermal components (magnetic field and cosmic rays), acceleration mechanisms and on the types of diffuse radio sources present in clusters.

2.1 Non-thermal components

Radio observations have shown the evidence of the presence of non-thermal components outside of radio galaxies (Willson 1970) such as cosmic rays (CRs), magnetic fields and turbulence (see Section 1.3.3). This radio emission (that we will describe in detail in Section 2.3) comes from synchrotron emitting electrons with Lorentz factors $\gamma > 10^3$ (hence with energies in the GeV range) interacting with the magnetic fields present in clusters. The existence of diffuse radio emission that is not associated with galactic

counterparts implies the existence of large scale magnetic fields embedded in the ICM. However, the origin of magnetic fields is still uncertain.
In the last years many studies have been carried out to constrain the magnetic field strength in clusters, retrieving values in the range $B \simeq 0.1 - 10\ \mu G$ (Bonafede et al. 2010, Brüggen et al. 2012) that can even reach a few tens of μG in the center of CCCs (Vacca et al. 2012). The intensity and the morphology of magnetic fields has a profound effect on both the energy transport and propagation of CRs, affecting also their lifetime (Ruszkowski & Oh 2010, Pfrommer et al. 2016). Estimating the magnetic field in clusters allows us to infer the lifetime of CRs and the non-thermal component contribution to the total mass and pressure in these objects.

There are different approaches to measure the intensity of magnetic fields and their morphology. The most important methods that are used to make such estimates exploit the Faraday rotation effect and the Rotation Measure (RM), like the RM Synthesis approach developed by Brentjens & de Bruyn (2005).
The Faraday effect takes place when a linearly polarized wave passes through a magnetized medium with free electrons (of density n_e) and causes a shift of the polarization angle ψ, described by the equation:

$$\Delta\psi = \mathrm{RM}\lambda^2 \quad [\mathrm{rad}] \tag{2.1}$$

The rotation measure RM is given by:

$$\mathrm{RM} \approx 812 \int_{los} \left(\frac{n_e}{\mathrm{cm}^{-3}}\right)\left(\frac{B_\parallel}{\mu\mathrm{G}}\right)\left(\frac{\mathrm{d}l}{\mathrm{kpc}}\right) \quad [\mathrm{rad/m}^2] \tag{2.2}$$

where λ is the wavelength of the radiation (in meters) and $B_\parallel$ is the magnetic field component parallel to the line of sight (los). There have been a few estimates of magnetic fields in clusters through this method (Bonafede et al. 2010, Govoni et al. 2010, Kuchar & Enßlin 2011, Vacca et al. 2012, Bonafede et al. 2013, Böhringer et al. 2016), with central values reaching up to $B \approx 5-10\ \mu$G in disturbed clusters and a few tens of μG in relaxed ones. The RM method also allows us to estimate the magnetic field radial profile (after assuming a density profile). Only a small number of these studies have been carried out because they need wide-band radio observations that are combined with X-ray observations from which the density profile can be estimated. The common result between these deep studies shows a decrease of the magnetic field intensity with the radial distance from the cluster center. In Fig. 2.1 it is shown the magnetic field profile of the Coma cluster and we can notice that, despite the fluctuations, the intensity is much lower in the outskirts compared to the central region.

Another method is to use the equipartition assumption between the CRs energy, U_e, and the magnetic field energy, U_B. From the synchrotron theory we have that the total energy budget of a source is given by:

$$U_{tot} = (1 + k)U_e + U_B \tag{2.3}$$

where $U_e \propto L_{syn}/B^{3/2}$ and $U_B = \int B^2/(8\pi)\mathrm{d}V$. The equipartition comes from the assumption that the energy is at its minimum state, corresponding to:

$$U_B = \frac{3}{4}(1 + k)U_e \tag{2.4}$$

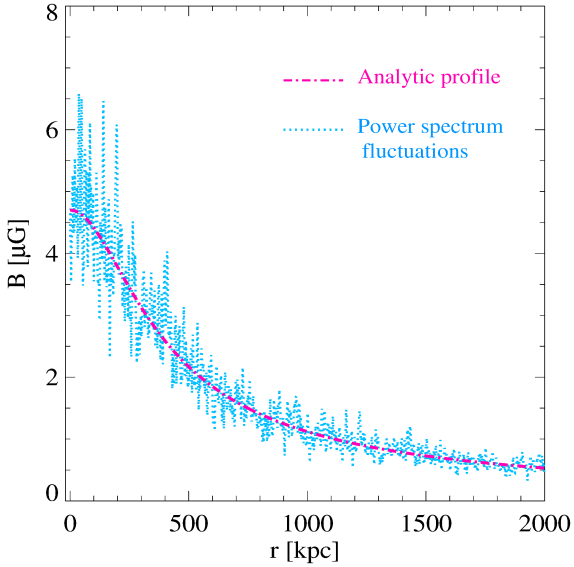

Figure 2.1: Best-fit of the magnetic field profile of the Coma cluster (Bonafede et al. 2010). Fluctuations of the power spectrum of the field are shown in blue.

If we make an assumption on k and estimate both the average surface brightness and the spectral index of a source, we can estimate the equipartition field by applying the formula from Govoni & Feretti (2004), which is:

$$B_{eq} = \left(\frac{24\pi}{7} u_{min}\right)^{1/2} \quad [\mathrm{G}] \tag{2.5}$$

where:

$$u_{min} = \xi(\alpha, \nu_1, \nu_2)(1+k)^{4/7}(\nu_0)^{4\alpha/7}(1+z)^{(12+4\alpha)/7}(I_0)^{4/7}(d)^{-4/7} \quad [\mathrm{erg/cm^3}] \tag{2.6}$$

where in this formula ξ is tabulated in Govoni & Feretti (2004), ν_0 in MHz is the observing frequency, z is the redshift of the source, I_0 in mJy/arcsec^2 is the brightness of the source and d in kpc is the source depth. The issues with this approach are related to the various assumptions needed (minimum energy state of the source, synchrotron bolometric luminosity, volume occupied by the emission and the constant k, related to the energy of cosmic ray protons) alongside with the fact that this cannot be used if the radiative lifetime of the electrons is much shorter than the radio source lifetime.

The diffuse radio emission in clusters comes from cosmic ray electrons, mixed within the ICM. By knowing the cluster properties (average magnetic field and redshift) we can estimate the lifetime for synchrotron emitting particles:

$$t_{age} \approx 3.2 \cdot 10^{10} \frac{B^{1/2}}{B^2 + B^2_{CMB}} [(1+z)\nu]^{-1/2} \ [\mathrm{yr}] \tag{2.7}$$

where B is the magnetic field strength, z is the source redshift, ν is the observing frequency (in MHz) and B_{CMB} is the equivalent magnetic field strength of the CMB ($B_{CMB} \approx 3.25(1+z)^2$ [μG]). The typical value in clusters is around $t_{age} \lesssim 10^8$ yr. By assuming the typical lifetime of a CRe[3] with a Lorentz factor $\gamma \sim 10^4$ ($t_{age} \approx 10^8$ yr),

[3]Cosmic Ray electron

Bagchi et al. (2002) found that the typical diffusion length-scale is about $R_d \approx 10$ pc, assuming also that Bohm diffusion takes place in clusters. If plasma motions are also took into consideration in the calculations, the length-scale can reach a few kpc. Brunetti (2003) considered, in the computations of the propagation scale of CRe, also the maximum magnetic field coherence scale for clusters ($l \sim 20$ kpc) and found that the maximum length-scale for cosmic ray electrons is of the order of $R_d \sim 50$ kpc. This is called *diffusion problem* and it means that, for radio sources which have sizes of at least a few hundreds of kpc, the CRe cannot be simply injected by radio-galaxies and diffused through the cluster volume during their lifetime, but they must be either produced or accelerated *in-situ*. Two different models were proposed to solve the *diffusion problem*: the hadronic (or secondary) model and the re-acceleration model. Hadronic models predict that the cosmic ray electrons are originated as secondary particles from nuclear interactions between cosmic ray protons and ICM protons (Dennison 1980). These interactions would produce a neutral pion π^0 that decays in two γ-ray photons, which then produce a high energy electron-positron pair. This means that, if hadronic models are the main acceleration mechanism of CRe, we should be able to detect clusters also in the γ-ray band. This would solve the diffusion problem since CRe would form by interactions *in-situ*, because CRp[4] can accumulate in the ICM, as their emission is much lower compared to the one of electrons. The ultra-relativistic protons might be accelerated by supernovae, shocks and AGN activity, accumulating over time. Considering that clusters hosting radio halos are not detected in the γ-ray band, only upper limits were put on this ultra high energy emission by using data from the Fermi-LAT satellite (Ackermann et al. 2016), which disfavours a completely hadronic origin of radio halos. On the other hand, re-acceleration models suggest that cosmic ray electrons are mildly relativistic ($\gamma \sim 10^2$) re-accelerated particles that were injected by past AGN activity through various processes such as shock, turbulence acceleration and adiabatic compression (Brunetti & Jones 2014).

2.2 Acceleration mechanisms

The presence of cosmic rays in galaxy clusters implies the presence of mechanisms that are accelerating particles to ultra-relativistic speeds. Depending on the type of diffuse radio source, there are different acceleration mechanisms that can explain the existence of ultra-relativistic electrons, which are, for example, diffusive shock acceleration (DSA) in the case of radio relics and turbulent (re-)acceleration for radio halos.
In the following sections we will describe the main acceleration mechanisms present in galaxy clusters.

2.2.1 Diffusive shock acceleration

The diffusive shock acceleration or first order Fermi acceleration mechanism (Fermi I) is the main process accelerating particles in many astrophysical scenarios (Malkov & Drury 2001), like supernovae shocks and radio relics. In this process, particles are continuously crossing the shock front, interacting with shocked and unperturbed clouds. The energy gain from each interaction is directly related to the shock velocity. A shock is characterized by its Mach number $\mathcal{M} = v_{sh}/c_s$, where v_{sh} is the shock

[4]Cosmic Ray protons

velocity and c_s is the sound speed in the medium. While the shocks produced in supernovae typically have Mach numbers $\mathcal{M} \sim 10^3$, shocks in the ICM are weak, with Mach numbers $1 \lesssim \mathcal{M} \lesssim 5$. The shock strength is strictly related to the acceleration efficiency and therefore to the synchrotron spectrum of cosmic rays (Botteon et al. 2020), allowing us to make predictions on the spectral index and on the radiative age of cosmic rays.

The Larmor formula sets a relation between the radiated power and the mass of the emitting particle ($P \propto m^{-2}$), meaning that the strong emitters are the lightest particles, therefore electrons. With the DSA mechanism the particle that is being accelerated needs to have a large Larmor radius which can be achieved either by a massive particle or by a fast moving light-weight particle. This leads to the problem on how the electrons are accelerated at the beginning of the process since they do not satisfy the requirements for the acceleration, this is also referred to as the *injection problem*. If CRe are particles accelerated from the Maxwellian high energy tail, they should have a minimum momentum related to the post-shock thermal momentum:

$$p_{min} = q_{inj} p_{th} \tag{2.8}$$

the problem is that constraining this value is very difficult and a small change of p_{min} can vastly change the resulting particle distribution.
Other viable solutions to the problem require a pre-acceleration of electrons, an example is given by re-acceleration models. In this scenario electrons are already mildly relativistic ($\gamma \gtrsim 10^2$) and have a gyro-radius large enough to be accelerated by DSA. These electrons should be injected by past AGN events in the cluster volume to be able to have already a high Lorentz factor.

2.2.2 Turbulent acceleration

Particles can also be accelerated through the so called second order Fermi acceleration mechanism (Fermi II), it is a stochastic acceleration process in which particles are randomly scattered by magnetic field inhomogeneities (Brunetti et al. 2001, Petrosian 2001). In clusters, these inhomogeneities are related to the turbulent nature of the ICM, that can be further amplified by merger events or cold gas motions (sloshing) induced by the AGN in the central region. Through this process particles can be either up-scattered or down-scattered, but on average there is an energy increase. This depends on the type of collisions between particles and clouds which are able to either accelerate or decelerate particles. From the theory of stochastic acceleration we have that, considering λ the mean free path between two collisions, the rate for an head-on interaction is:

$$\frac{1}{\tau} \sim \frac{|v + V|}{\lambda} \tag{2.9}$$

while for tail collisions we have:

$$\frac{1}{\tau} \sim \frac{|v - V|}{\lambda} \tag{2.10}$$

where v is the speed of the particle and V is the speed of the magnetized cloud. We can clearly see that heads-on interactions happen with a higher rate, leading to an overall acceleration of particles. Due to the stochastic nature of this process, the acceleration efficiency is much lower compared to the one of the Fermi I mechanism, leading to the particles being accelerated to lower energies and in a smaller number, hence we observe a steeper and curved synchrotron spectrum.

2.2.3 Hadronic models

As we briefly explained in Section 2.1, hadronic models can also explain the presence of diffuse radio emission in clusters through nuclear inelastic interaction between CRp and thermal protons of the ICM. Cosmic ray protons could be accelerated by various processes, such as supernovae shocks, AGN jets and merger shocks and accumulate over time in the ICM due to their low emitting power (given by $P \propto m^{-2}$), the average lifetime of CRp related to nuclear interactions is:

$$\tau_{pp} \simeq \frac{1}{c n_{th} \sigma_{pp}} \tag{2.11}$$

where σ_{pp} is the cross-section of the interaction and n_{th} is the density of the ICM. For ultra high energy cosmic ray protons ($E \sim 1$ GeV $- 1$ TeV) this lifetime is of a few Gyr. The chain reaction for the production of CRe described by hadronic models is:

$$p + p \rightarrow \pi^0 + \pi^+ + \pi^- \tag{2.12}$$
$$\pi^0 \rightarrow 2\gamma \tag{2.13}$$
$$\pi^\pm \rightarrow \mu^\pm + \nu_\mu \tag{2.14}$$
$$\mu^\pm \rightarrow e^\pm + \nu_e + \nu_\mu \tag{2.15}$$

In contrast to what we expect from turbulent acceleration, the integrated spectra from hadronic models should not show a strong break in the energy spectrum (Timmerman et al. 2021), due to the continuous production of cosmic ray electrons.
Hadronic models cannot explain the existence of ultra steep spectrum halos, since their spectral energy distribution would be very steep, predicting an unphysical situation in which clusters would be dominated by this particles (Brunetti et al. 2008).

2.3 Diffuse radio emission

Alongside with the emission from radio-galaxies, in clusters it is possible to observe diffuse emission not associated with any optical counterpart or discrete source in general. van Weeren et al. (2019) classified these sources into: radio halos (classical and mini), radio relics (or radio shocks), phoenices and Gently Re-Energized Tails (GReETs).
Recently two other types of large scale diffuse radio emission have been discovered: radio bridges (Govoni et al. 2019, Botteon et al. 2020, Pignataro et al. 2023) and mega radio halos (Cuciti et al. 2022).
All these sources have low surface brightnesses and steep spectra ($\alpha > 1$ when $S_\nu \propto \nu^{-\alpha}$). The exact origins of these sources are still unknown.

2.3.1 Radio halos

Radio halos are diffuse unpolarized sources found mostly in disturbed clusters (Cassano et al. 2010), although there are cases of halos present in relaxed clusters (Bonafede et al. 2014). They show a smooth distribution following roughly the X-ray emission (Rajpurohit et al. 2018), their radii are of the order of $R \sim 500 - 800$ kpc. An example of a classical halo is shown in the left panel of Fig. 2.2. The surface brightness of radio halos is low, ranging between $0.1 - 10$ μJy/arcsec^2 (Cuciti et al. 2021) and the luminosities lie in the range $P_{1.4\ \mathrm{GHz}} \sim 10^{23} - 10^{26}$ W/Hz (Cuciti et al. 2021). These

sources show steep spectra ($1.1 < \alpha < 1.4$; Giovannini et al. 2009), with the average value of the spectral index $\alpha = 1.3$ (Feretti et al. 2012), although there is a sub-class of halos with the spectral index in the range $1.6 < \alpha < 2.0$, which are called ultra steep spectrum radio halos (Brunetti et al. 2008, Cassano et al. 2010, Pasini et al. 2024). The study of the integrated spectra of halos is of uttermost importance because

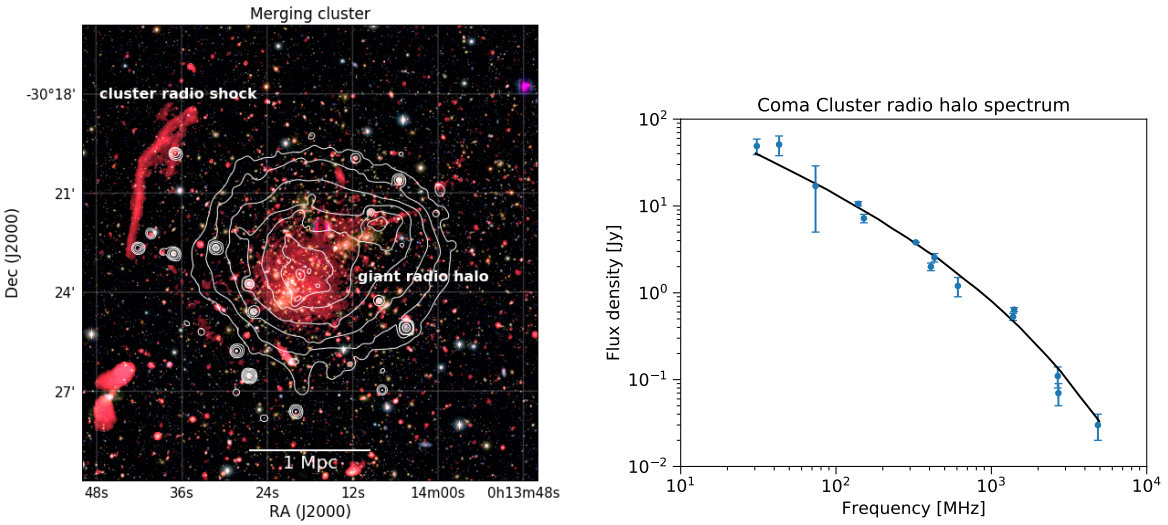

Figure 2.2: *Left*: The cluster Abell 2744 hosting a giant radio halo and a radio relic (both labeled as such), the white contours are X-ray surface brightness contours from Chandra (from van Weeren et al. 2019). *Right*: Integrated radio spectrum fit of the radio halo present in the Coma cluster, from Pizzo (2010).

it allows us to better understand the acceleration mechanisms behind this emission and their efficiency, in other words gives us a better view on the origin of halos. In most cases, the flux and spectral information is based only on two measurements at different frequencies, which, unfortunately, does not allow us to follow the actual aging of particles and to study the deviations from the predicted power-law spectrum. The best studied spectrum is the one of the Coma cluster halo, that we can see in Fig. 2.2, and it clearly shows the curvature originated by the low efficiency and by the subsequent particle aging.
Spectral index maps can also be produced and studied, giving information on the properties of the emission. The first one was carried out by Giovannini et al. (1993), where it was found that there is a radial steepening of the spectral index. However, more recent studies (Pearce et al. 2017, Rajpurohit et al. 2018) show that the spectral index distribution is almost uniform across the entire source.

There are also scaling relations between clusters properties and the radio power of radio halos, like the radio power-X-ray luminosity relation (Yuan et al. 2015) and radio power-mass relation (Basu 2012, Cuciti et al. 2023).

Numerous studies (such as Murgia et al. 2009, Bonafede et al. 2017 and Cuciti et al. 2022) showed that both radio and mini halos radial profiles can be fitted with an exponential function:

$$I(r) = I_0 \exp(-r/r_e) \tag{2.16}$$

where I_0 is the central surface brightness and r_e is the effective radius.

The current favored mechanism to explain the existence of radio halos states that the cosmic rays are re-accelerated from a pool of mildly relativistic electrons ($\gamma \sim 10^2$)

by the turbulence induced by major and minor mergers, this is specifically supported by the steep (and curved) spectra that are observed, which should be related to the low efficiency of turbulent acceleration. The energy budget of radio halos is set by the mass of the accreted cluster. More massive clusters inject more energy and therefore the efficiency of the acceleration process is higher, accelerating more particles to higher energies. Hence, we expect that a merger between massive systems forms a radio halo with a typical spectral index $\alpha \simeq 1.3$, while minor mergers and mergers with less massive systems are expected to originate ultra steep spectrum radio halos ($\alpha > 1.6$; Cassano et al. 2010). The different spectral indexes have observational consequences, halos with ultra steep spectra are detectable at frequencies of at most a few hundreds of MHz, while typical halos can be observed up to ~ 1 GHz.

2.3.2 Mini halos

Radio mini-halos (or simply mini halos) are found in the central region of most of cool-core clusters (Kale et al. 2013, Giacintucci et al. 2017) and surround the cD galaxy (Gitti et al. 2015). Mini halos have sizes in the range of $100 - 500$ kpc, roundish shapes and often they surround the X-ray cavities and radio bubbles that are found around the BCG. The sizes correspond roughly with the size of the cooling region (region in which the cooling time is shorter than the cluster age). The radio power at

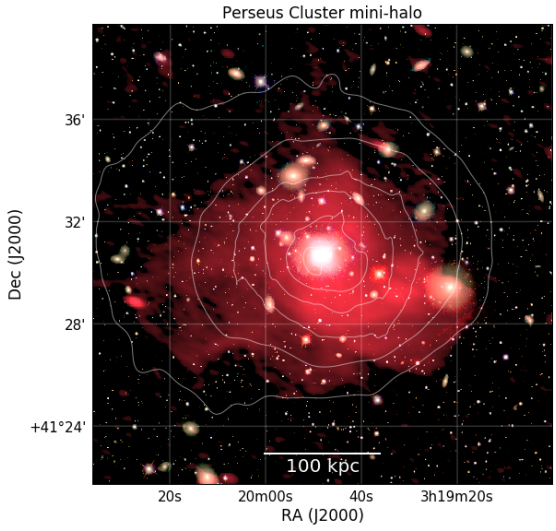

Figure 2.3: Overlays between the optical image and radio image of the Perseus galaxy cluster center showing the mini-halo present (in red). The white contours are surface brightness contours from XMM-Newton in the 0.4–1.3 keV band. From van Weeren et al. (2019).

1.4 GHz $P_{1.4\ \mathrm{GHz}}$ ranges between $P_{1.4\ \mathrm{GHz}} \sim 10^{23} - 10^{25}$ W/Hz and the spectral index is steep, with similar values to classical halos. Although the spectral index and power are similar, mini-halos have an higher emissivity compared to radio halos and smaller effective radii (Murgia et al. 2009). The best mini halo example is shown in Fig. 2.3 and is located in the Perseus cluster.

The *diffusion problem* exists also on mini halos scales and *in-situ* acceleration models are needed to explain their existence, but, differently from radio halos, both turbulent re-acceleration (Gitti et al. 2002) and hadronic (Pfrommer & Enßlin 2004) models can explain the presence of the emission. While for radio halos turbulent motions are

related to merger events, it is not the same for mini halos, where the turbulence is thought to be originated by the gas sloshing from the central AGN activity, meaning that mini halos could trace these motions (ZuHone et al. 2015). In this case the fossil electrons would be injected by the cD galaxy. Mazzotta & Giacintucci (2008) showed that mini halos are confined by cold fronts, supporting the turbulent re-acceleration scenario.
A clear prediction of secondary models is the emission of γ-ray photons emitted by the decay of neutral pions originated from the interactions (the high energy photons will then decay into ultra-relativistic electrons and positrons), hence the detection or non-detection of this emission allows us to put limits on the process. Due to the fact that it is complex to disentangle the γ-ray emission of the central AGN from the one of the possible hadronic collisions, the true discriminant between the two models is given by the integrated spectrum, unfortunately there are not many spectral studies on mini-halos due to the complexity of the radio emission and therefore the origin of mini-halos is still debated.

2.3.3 Radio relics, phoenices and GReETs

Radio relics are elongated or arc-like shaped structures found mostly in the outskirts of merging clusters and which can reach sizes of about ~ 1 Mpc. This emission traces the ICM shocks, therefore is produced by particles that have been (re-)accelerated by diffusive shock acceleration. As we already discussed in Section 2.2.1, the acceleration efficiency is higher compared to the one of turbulent acceleration, this leads to flatter spectra with spectral indexes $1 < \alpha < 1.3$ (Bonafede et al. 2012, de Gasperin et al. 2014) and due to the gas compression the emission is highly polarized, with fractions $p \gtrsim 20\%$ at 1.4 GHz (Stuardi et al. 2022, Hoeft et al. 2022), a radio relic is shown and labeled in Fig. 2.2. Radio relics can be found either alone or in pairs in clusters; in the latter case they are found diametrically with respect to the cluster center and perpendicularly compared to the merger axis. Relics can coexist with radio halos and, in some cases, overlap with them, where it is said that the emission is bridged (van Weeren et al. 2016). The bridged region might be the location where the acceleration mechanism shifts from Fermi I to turbulent acceleration, although in some cases the projection effect may play a role.
Radio relics are less common compared to radio halos, Golovich et al. (2019) found that it could be related to the angle between the merger axis and the line of sight. In fact, in clusters hosting relics, the merger axis is perpendicular to the line of sight (or with great angles), meaning that there are selection biases based on the viewing angle that affect the possibility to find radio relics.
Integrated spectra studies are important since they allow us to understand the efficiency of the acceleration process and also to estimate the Mach number of the shock avoiding the projection biases from X-ray observations. Due to the high efficiency of the DSA mechanism we expect the spectral energy distribution break at high energies, allowing observations at relatively high frequencies (a few GHz), hence the expected spectrum should be very well fitted by a simple power-law at frequencies around 1GHz, as shown in Fig. 2.4. It is also important to notice that in relics there is a spectral steepening in the transverse direction of the shock, possibly caused by synchrotron and IC losses.

Radio phoenices (Kempner et al. 2004) and Gently ReEnergized Tails (GReETs, de Gasperin et al. 2017) are two other classes of radio sources found in clusters that are

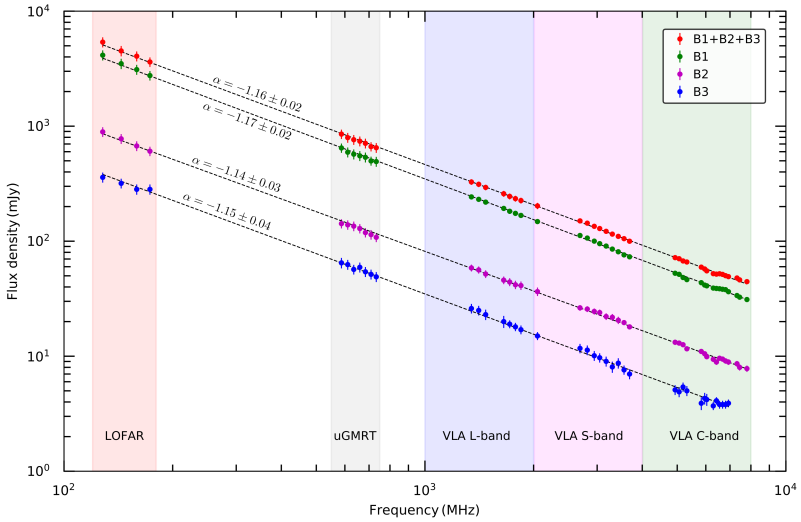

Figure 2.4: Integrated spectra of the Toothbrush relic and of its sub-regions, the spectra can be described with a single power-law ruling out any spectral steepening below 8 GHz (Rajpurohit et al. 2020).

related to the fossil plasma from past AGN activity that has been re-energized. These sources have relatively small sizes of a few hundreds of kpc at most and are best observed at very low frequencies. The difference between phoenices and GReETs resides in the re-energization mechanism. The current favored scenario to explain the existence of phoenices supposes that they trace plasma from past AGN activity in the cluster and the re-energization happens through the adiabatic compression (e.g. induced by the passage of shock waves) that increases the momentum of the mildly relativistic electrons and the intensity of the magnetic field. The adiabatic compression has a low acceleration efficiency, therefore we expect to observe a steep and curved spectrum (Enßlin & Gopal-Krishna 2001, van Weeren et al. 2009), while the morphologies can be irregular and complex (Ensslin & Bruggen 2002). Radio phoenices have also low radio powers, low polarization fractions and are found at small cluster-centric distances.

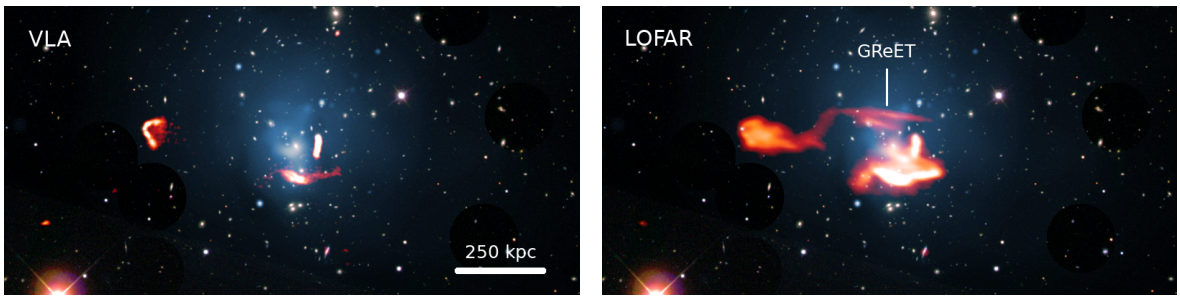

Figure 2.5: Optical image of the cluster Abell 1033, with overimposed the X-ray emission and the radio emission from VLA (left) and LOFAR (right). In the LOFAR image we can see extended emission related to the radio-galaxy on the left, it is the first GReET discovered. From van Weeren et al. (2019).

The re-energization for the GReETs is a much gentler process, which can barely re-accelerate particles, leading to an ultra steep spectrum, e.g. $\alpha = 3.86 \pm 0.03$ (de Gasperin et al. 2017), and keeping it constant along the entire tail. The re-energization is thought to be related to the instabilities originated by the interaction

between the relativistic plasma and the ICM (like the Kelvin-Helmholtz and Rayleigh-Jeans instabilities), allowing a constant acceleration and thus producing the flat spectrum. Because there are only a few known GReETs and candidates that have been detected, their nature and origin is still uncertain. A GReET is shown in Fig. 2.5.

2.3.4 Radio bridges

Radio bridges are a recently discovered type of diffuse radio emission, spanning a few Mpc in size connecting clusters together. The first radio bridge was discovered with LOFAR by Govoni et al. (2019) between the clusters Abell 399 and Abell 401, covering a projected distance of 3 Mpc, showing that non-thermal emission can be found also outside of galaxy clusters (shown in Fig. 2.6).
The origin of this emission is still unknown since it has been observed only in a few systems (Govoni et al. 2019, Botteon et al. 2020, Hoeft et al. 2021). Since the cluster

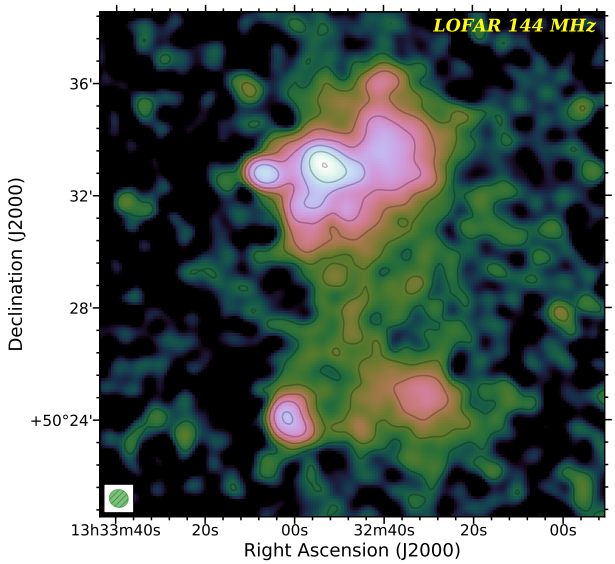

Figure 2.6: Deep LOFAR HBA image of the cluster pair Abell 1758, hosting a northern cluster and a southern one (Botteon et al. 2020). All the discrete sources have been subtracted by the image, leaving only the diffuse emission.

pairs are all in a pre-merger phase, new acceleration processes are needed to explain the presence of the emission. Brunetti & Vazza (2020) presented a mechanism that can explain the origin of bridges through the turbulent acceleration of fossil plasma particles present in the cosmic web, producing curved spectra with steep indexes. The few spectral index studies that have been carried out (Botteon et al. 2020, Hoeft et al. 2021, Pignataro et al. 2024) report values of the spectral index in the range $1.4 < \alpha < 1.7$, consistent with the simulations, although deeper studies must be done to asses the origin and the properties of the emission alongside with multi-frequency studies to determine the integrated spectrum of the emission.

2.3.5 Mega radio halos

Cuciti et al. (2022) discovered a new type of diffuse radio emission in four massive ($M > 6 \cdot 10^{14}$ $M_\odot$) clusters, analyzing the data from the second LOFAR[5] Two Meter Sky Survey Data Release. These sources take the name of megahalos. It is a large scale emission with radii that can reach and even exceed r_{500}, filling a volume that is at least 30 times larger than the one occupied by classical halos. Unlike radio halos, megahalos exhibit almost constant radial surface brightness profiles. Their average surface brightness is around one order of magnitude lower compared to the central brightness of radio halos. The computed radio powers are comparable with the ones from radio halos, being in the range of $P_{150\ \mathrm{MHz}} \sim 10^{24} - 10^{25}$ W/Hz. The only

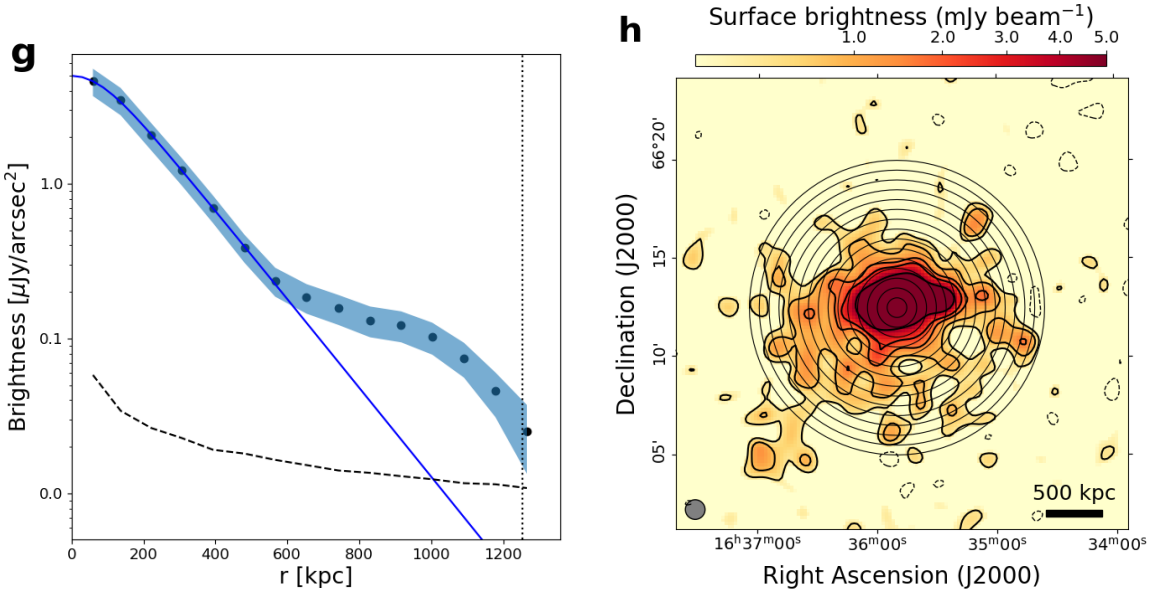

Figure 2.7: *Left*: surface brightness profile for the cluster Abell 2218. The shaded region represents the errors on the measurements, the vertical line is r_{500}, the dashed line is 1σ detection limit of the surface brightness for each annulus and the blue solid line is the exponential fit of the radio halo surface brightness profile. The discontinuity in the profile shows the presence of the megahalo emission. *Right*: $60''$ resolution image of the cluster Abell 2218, the annuli show the regions over which the brightness has been measured to produce the profile (Cuciti et al. 2022).

megahalos known so far were all discovered by Cuciti et al. (2022) in non cool-core clusters and only for two of them it was possible to estimate the spectral index, using both LOFAR high band antenna (HBA) and low band antenna (LBA) data, showing hints of ultra steep spectra, with indexes $\alpha \simeq 1.6$. Botteon et al. (2022) studied the cluster Abell 2255 with ultra-deep LOFAR observations, detecting emission up to r_{200}. Despite the similarities with megahalos, the large scale emission in A2255 has not been classified as a megahalo because the cluster hosts many types of diffuse sources with complex morphologies that prevent a proper characterisation of the surface brightness profile.
One of the four megahalos detected is shown in Fig. 2.7 alongside with its surface brightness profile. The origin of megahalos is still unknown, but their scale shows that magnetic fields and cosmic rays exist on volumes that are much larger than the ones

[5]LOw Frequency ARray

observed up to this day. The ultra steep spectrum hints to an inefficient acceleration mechanism, which lead to a first hypothesis of it being a turbulent acceleration process. Due to the low surface brightness on such large scales and ultra steep spectral index of megahalos, it has been possible to observe them only with LOFAR at low frequencies (< 200 MHz), since it is the only instrument capable of observing at such frequencies with a high sensitivity.
Cosmological simulations can help us understanding the mechanisms that are involved in the formation of this large scale emission. Beduzzi et al. (2023) simulated a single cluster, with mass $M_{100} = 3.8 \cdot 10^{14}$ $M_\odot$ and size $r_{100} = 1520$ kpc, considering only self-gravity and radiative equilibrium cooling. In the simulation they considered an initial uniform magnetic field $B_0 = 0.4$ nG starting from $z = 40$ and letting it evolve following ideal magneto-hydrodynamics. This simulation tests the possibility of the formation of megahalos through turbulent acceleration, which could affect fossil cosmic ray particles that were accreted from the merging with gas clumps and pre-accelerated during their passage through the core. In this scenario, these electrons should have longer lifetimes due to the lower magnetic fields and should be easily (re-)accelerated by future merger events. This study showed that, through turbulence, up to $\sim 50\%$ of particles in the megahalo region are able to emit in the frequency range $50 - 140$ MHz after the last major merger. In Beduzzi et al. (2024) the same cosmological simulation has been analysed, with the addition of the solution of the radiative loss equation for cosmic ray particles. It has been observed that the turbulence in the outskirts has higher Mach numbers when compared to the one in the classical radio halo regions and that the re-energization is led by the turbulence. Another interesting result from Beduzzi et al. (2024) is that in this simulation the megahalo emission is not spherically symmetric and not always present in the evolution of the cluster, but can be observed only within certain angles with respect to the line of sight. Future simulations of more massive clusters will allow us to better constrain the properties of megahalos, but also to understand their formation scenario, alongside with the origin of radio halos.

Chapter 3

This thesis work

After the detection of the megahalos, Cuciti et al. (2022) proposed a possible relation between the megahalo surface brightness and the cluster mass. This relation, shown in Fig. 3.1, is derived assuming a power-law relation between the surface brightness (SB) and the cluster mass ($SB \propto M^{\beta}$) and taking into account the surface brightness cosmological dimming ($SB \propto (1+z)^{-4}$). In addition, the normalization has been derived from the sensitivity of the survey. The three curves in the figure in Fig. 3.1 are related to three different assumptions for the exponential in the relation between the mass and the brightness. Following the assumptions, we expect to detect megahalos above at least one of these curves, set by the brightness-mass relation, since they are related to the sensitivity of current observations. We can see from Fig. 3.1 that there are other massive clusters above the theorized curves, making them the best candidates to search for megahalos using LOFAR observations. Between all the possible candidates, we selected four of them, which are Abell 2219 (A2219), Abell 2390 (A2390), Abell 1763 (A1763) and Abell 2261 (A2261), highlighted and labeled in red in Fig. 3.1. These are among the most massive sources of the LOFAR survey, and are located at an intermediate redshift of $z \simeq 0.2$. The targets of this project are both disturbed and relaxed clusters, allowing us to put constraints on the presence of megahalos also on cool-core clusters.
Since the origin of megahalos is still unknown, it is important to increase the size of the sample to understand if they are present in every cluster or not, and if their presence can be related to the dynamical state of clusters.

Our data come from the public release of the LOFAR Two Meter Sky Survey (LoTSS; Shimwell et al. 2017) Data Release 2 (Shimwell et al. 2022, Botteon et al. 2022; LoTSS-DR2), specifically are sources from the second Planck catalog of SZ sources (PSZ2; Planck Collaboration et al. 2016).
The clusters we have selected were excluded from the analysis by Botteon et al. (2022) due to the low image quality, either related to a high σ_{rms} or very strong image artifacts. In addition, Abell 2261 was excluded because of the presence of residual flux from a powerful radio galaxy, related to the non-perfect subtraction of the source.
In Table 3.1 the main properties of these clusters are listed, such as their mass, radius, redshift, the number of pointings available for each source and the rms of the calibrated image.

We will follow a subtraction process calibrated "ad-hoc" for each cluster in order to remove all the discrete sources and then we will produce the surface brightness profile of the radio and megahalo emissions (if present) and estimate its main properties, such

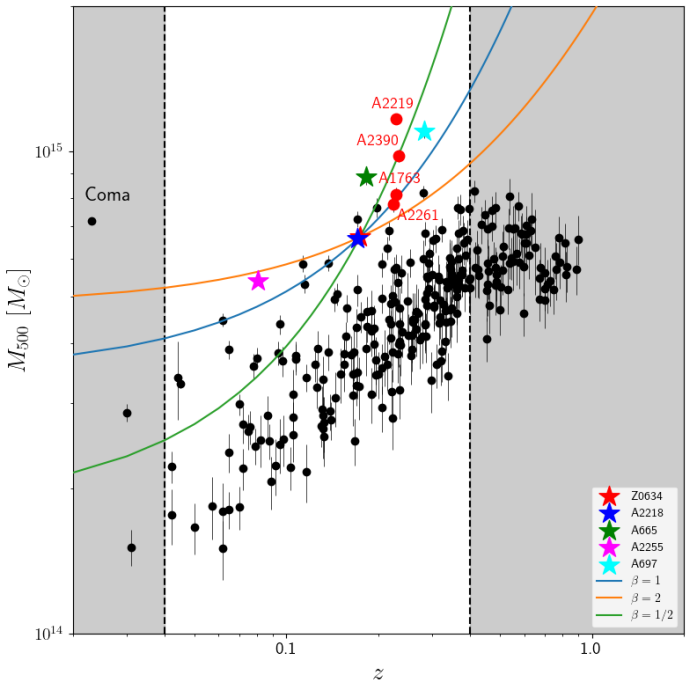

Figure 3.1: Mass-redshift plot showing the PSZ2 clusters observed in the LoTSS-DR2. The star markers highlight the clusters in which Cuciti et al. (2022) found the megahalos, except for Abell 2255 that has been studied by Botteon et al. (2022) but there is no confirmation of the megahalo. The four red dots are the clusters analyzed in this work. The shaded areas are regions in which it would not be possible to detect megahalo emission either due to the scale being greater than the larget recoverable scale or due the resolution being too low. The three colored curves relate the surface brightness of megahalos with the cluster mass and the redshift assuming a power-law relation and the cosmological dimming, respectively. From Cuciti et al. (2022).

as flux, radio power and extension. We will also search for hints of a possible radio power-mass relation for megahalos, assuming that their behavior is similar to the one of radio halos, giving us the first insight on the properties of the emission.
We assume the Concordance Λ−CDM cosmological model with $H_0 = 70$ km/s/Mpc, $\Omega_M = 0.3$ and $\Omega_\Lambda = 0.7$.

Object	M_{500} [$\times 10^{14}$ $M_\odot$]	r_{500} [kpc]	z	No. of pointings	σ_{rms} [mJy/beam]
Abell 2219	11.69 ± 0.26	1490 ± 11	0.228	4	0.111
Abell 2390	9.80 ± 0.28	1402 ± 13	0.233	1	0.216
Abell 1763	8.13 ± 0.27	1320 ± 14	0.228	3	0.075
Abell 2261	7.78 ± 0.31	1302 ± 17	0.224	3	0.106

Table 3.1: Main properties of the four targets of this work.

3.1 Abell 2219

Abell 2219 is the most massive PSZ2 cluster of the LoTSS-DR2 with $M_{500} = (11.69 \pm 0.26) \cdot 10^{14}$ $M_\odot$ and $r_{500} = 1490 \pm 11$ kpc at a redshift $z = 0.228$, corresponding to a luminosity distance $D_L = 1135.3$ Mpc.

It hosts a powerful giant radio halo that was firstly detected through the NVSS (Giovannini et al. 1999) and confirmed with deeper VLA observations at 1.4 GHz by Bacchi et al. (2003) and at 325 MHz by Orrù et al. (2007). Due to the image artifacts caused by the strong AGN at the center of the cluster, the image quality was classified as low by Botteon et al. (2022) and it was not analyzed by the LOFAR team.
In Fig. 3.2, we can see both the LOFAR and XMM-Newton images of A2219.

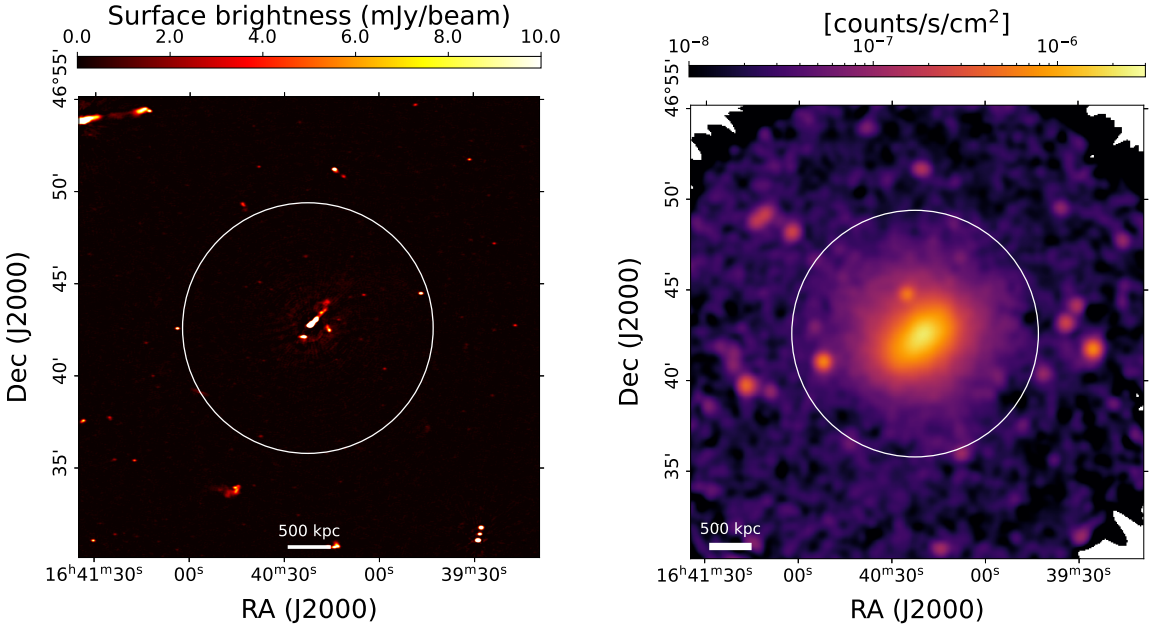

Figure 3.2: LOFAR 144 MHz (left) and XMM-Newton (right) images of A2219. The resolution of the radio image is of $\sim 6''$ and the area is of roughly 1 deg^2. Thw white circles show the extension of r_{500}.

From the X-ray image, we can see that the emission and so ICM distribution is elongated on the SouthEast-NorthWest direction, hint of a disturbed cluster morphology. Bacchi et al. (2003) studied this cluster with VLA observations at 1.4 GHz and found that the strong radio source at the center of the cluster is actually a blend of three sources (see the left panel in Fig. 3.2). From the same study ,it has been found that the radio halo has a regular and symmetric structure with a linear size of more than 2 Mpc, making it one of the largest sources known in the literature. By analyzing ROSAT images, Rizza et al. (1998) discovered the presence of two main X-ray peaks displaced by around 220 kpc, confirming that the cluster is in a merger state.
To sustain the hypothesis of this being a disturbed cluster, many other studies were carried out. Boschin et al. (2004) showed that A2219 is not a relaxed cluster, using both Chandra archival data and optical spectroscopical observations. The X-ray and mass distributions show a SouthEast-NorthWest elongation (see also the right panel in Fig. 3.2). From its observations, Boschin et al. (2004) suggested a complex merger history, with the system undergoing an in-fall of many clumps aligned with a filament in the foreground, oriented with an oblique angle with respect to the line of sight.

More hints on the merger scenario are given by the average temperature of the gas $T_X = 9.5$ keV obtained by Allen & Fabian (1998) and by the X-ray luminosity in the $0.1 - 2.4$ keV range $L_X = (19.8 \pm 2.2) \cdot 10^{44}$ erg/s (Ebeling et al. 1998, Smith et al. 2005), in fact this is among the hottest and most luminous clusters known. Although Boschin et al. (2004) determined the mass distribution from the spectroscopical analysis, Bezecourt et al. (2000) carried out a gravitational lensing analysis studying the 2D mass distribution and found the presence of two main mass clumps, centered on the two brightest galaxies of the cluster. Through Chandra observations, also Million & Allen (2009) found hints of a past merger event, by detecting a shock near the center of the cluster (at around $\sim$ 430 kpc), with a Mach number $\mathcal{M} > 1.3$, in the North-West direction. Cassano et al. (2010) determined the disturbed dynamical state of this cluster by measuring the three main dynamical parameters (w, c and the power ratio). Canning et al. (2017) studied the cluster through deep Chandra observations and detected multiple shocks surrounding the two BCGs alongside with another shock along the merger axis, similar to the one detected first by Million & Allen (2009) and with a comparable Mach number, but in the opposite direction. They also confirmed the presence of the two X-ray peaks noticing also that their position corresponds to the position of the two brightest galaxies, suggesting that one of the two was once part of the accreted sub-cluster, supporting the finding from Bezecourt et al. (2000).

3.2 Abell 2390

The cluster Abell 2390 has a mass of $M_{500} = (9.80 \pm 0.28) \cdot 10^{14}$ $M_\odot$, a size of $r_{500} = 1402 \pm 13$ kpc and its located at $z = 0.233$, which corresponds to $D_L = 1163.5$ Mpc. This cluster hosts a very powerful radio galaxy that has been identified as the cD galaxy (Pierre et al. 1996), ROSAT observations indicate that this source coincides also with the peak of the X-ray luminosity (Pierre et al. 1996, Boehringer et al. 1998). Allen et al. (2001) highlighted the presence of an X-ray sub-structure on the large scale that is likely related to a past merger of the cluster. Despite this, the cluster has been classified as a cool-core cluster (Allen 2000, 2001, 2008), as the temperature is not constant in the central region, but increase with the radius in the first $\sim$ 200 kpc, before becoming almost isothermal, as shown by Allen et al. (2001). Alongside with the non-isothermal profile, Allen (2000) computed the cooling time, finding a value of $t_{cool} \approx 4$ Gyr, which is shorter than the threshold value for the definition of cool-core clusters (see Section 1.3).
Weißmann et al. (2013) did a morphological study of the cluster based on the dynamical estimators and characterized this cluster as an intermediate core, having the power ratio P_3/P_0 very close to the threshold value determined by Cassano et al. (2010), which separates cool-core clusters from non cool-core clusters (see Section 1.3.1).
This cluster was also studied by Bacchi et al. (2003) through VLA 1.4 GHz observations, where they detected the presence of diffuse radio emission and classified it as a mini halo with an extension of around $\sim$ 550 kpc. Follow up JVLA observations were analyzed by Sommer et al. (2017), where they were able to classify the emission of the diffuse radio component as a radio halo instead of a mini halo, in fact the extension of the emission in their observations reaches a linear size of $\sim$ 800 kpc. Sommer et al. (2017) estimated also the spectral index of the radio halo, obtaining a value of $\alpha = 1.60 \pm 0.17$, computed it in the JVLA wide band in the range $\nu = 1 - 2$ GHz and classifying it as an ultra step spectrum radio halo.

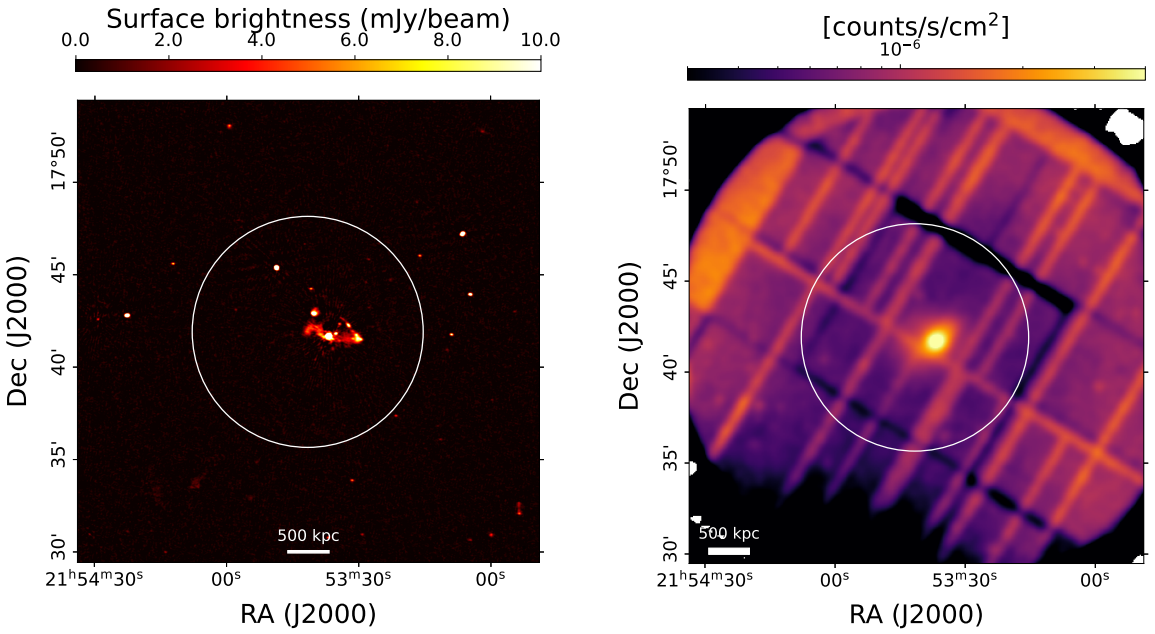

Figure 3.3: *Left*: the cluster Abell 2390 at 144 MHz at a resolution of 6″. *Right*: the same cluster seen from XMM-Newton. The white circles are representing r_{500}, the area is of ~ 1 deg^2.

Recently, Savini et al. (2019) analyzed this cluster through high resolution LOFAR observations. They found that the cD galaxy is a double radio galaxy with the lobes extending for about ~ 600 kpc and filling the X-ray cavities in the ICM. The authors note that radio galaxies with such a great extension are not common in the central region of clusters. Due to the presence of artifacts near the core of the central radio galaxy, Savini et al. (2019) could not perform an accurate subtraction of the source to search for the radio halo emission detected by Sommer et al. (2017), hence they could only conclude that the radio emission is mostly dominated by the BCG. In Fig. 3.3 we can see both the high resolution image from the LoTSS-DR2 and the XMM-Newton image. Unfortunately the X-ray image has a bad quality due to the low counts and strong flaring, hence it cannot be used to asses the ICM distribution; despite this, we can clearly see the peak of the emission that coincides with the position of the central radio galaxy.

3.3 Abell 1763

The third target of this study is Abell 1763, it has a mass of $M_{590} = (8.13 \pm 0.27) \cdot 10^{14}$ M$_\odot$ and a radius of $r_{500} = 1320 \pm 14$ kpc, at a redshift $z = 0.228$, which corresponds to $D_L = 1135.3$ Mpc.
Spitzer data analyzed by Fadda et al. (2008) and Edwards et al. (2010) show the presence of a stream of galaxies along a cluster filament, connecting Abell 1763 with a neighboring and smaller cluster, Abell 1770, covering a distance of around ~ 12 Mpc. In the left panel of Fig. 3.4 we can see the LoTSS-DR2 image of the cluster and the XMM-Newton image, the latter one is interesting as we can see a peaked and elongated X-ray distribution with two other peaks in the South-Western region, suggesting that there could be an ongoing off-axis merger.

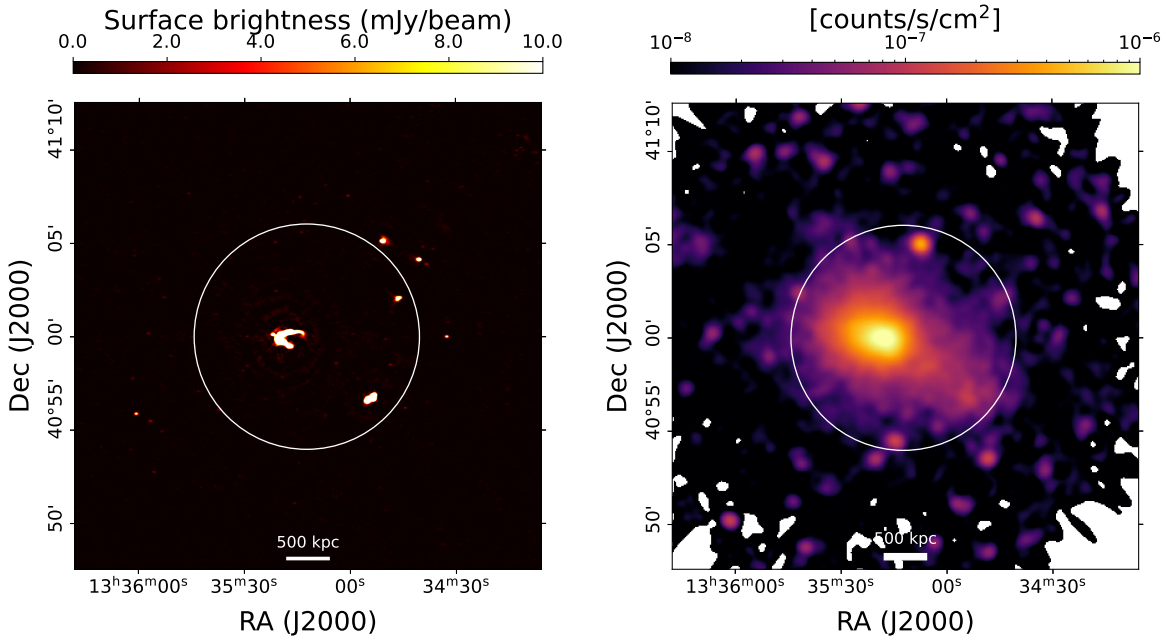

Figure 3.4: *Left*: the cluster Abell 1763 at 144 MHz at a resolution of 6″. *Right*: the same cluster seen from XMM-Newton. The white circles are representing r_{500}, the area is of ~ 1 deg^2.

Through Chandra observations, Douglass et al. (2018) found hints of strong sloshing in the cluster, alongside with the presence of two sub-clusters (centered on the second and third brightest galaxies in the system) along the elongation axis of the ICM distribution. Douglass et al. (2018) suggest that these systems might be the reason of the disruptive core sloshing. Based on these observations, they suggest that Abell 1763 is a case of cool-core disruption by an off-axis merger, a quite unusual scenario.
The case proposed by Douglass et al. (2018) is further supported by the Spitzer studies from Fadda et al. (2008) and Edwards et al. (2010). Venturi et al. (2008) analyzed archival VLA data at 1.4 GHz and found no hints of large scale radio emission, no upper limits were derived for this emission at this frequency.

3.4 Abell 2261

Abell 2261 is the least massive cluster that we studied in this work, with a mass of $M_{500} = (7.78 \pm 0.31) \cdot 10^{14}$ M$_\odot$ and radius $r_{500} = 1302 \pm 17$ kpc located at $z = 0.224$, corresponding to a luminosity distance $D_L = 1112.9$ Mpc.
Venturi et al. (2008) studied the VLA 1.4 GHz archival data of this cluster and found possible hints of extended ($850 - 1000$ kpc) radio emission around the central radio galaxy. Kale et al. (2013) analyzed this cluster using the data of the extended GMRT radio halo survey and did not find any extended radio emission at 610 MHz, setting an upper limit of $\simeq 8$ mJy, which is below the $P_{1.4\ \mathrm{GHz}} - M$ relation. The first confirmation of the presence of the radio halo comes from Sommer et al. (2017), where they modeled the compact component of the VLA archival images and subtracted it, finding a very low value of $\simeq 4$ mJy. Savini et al. (2019) studied this cluster using LOFAR observations at 144 MHz and Chandra X-ray data. The X-ray distribution shows a patch of X-ray emission in the western part of the cluster, possibly associated

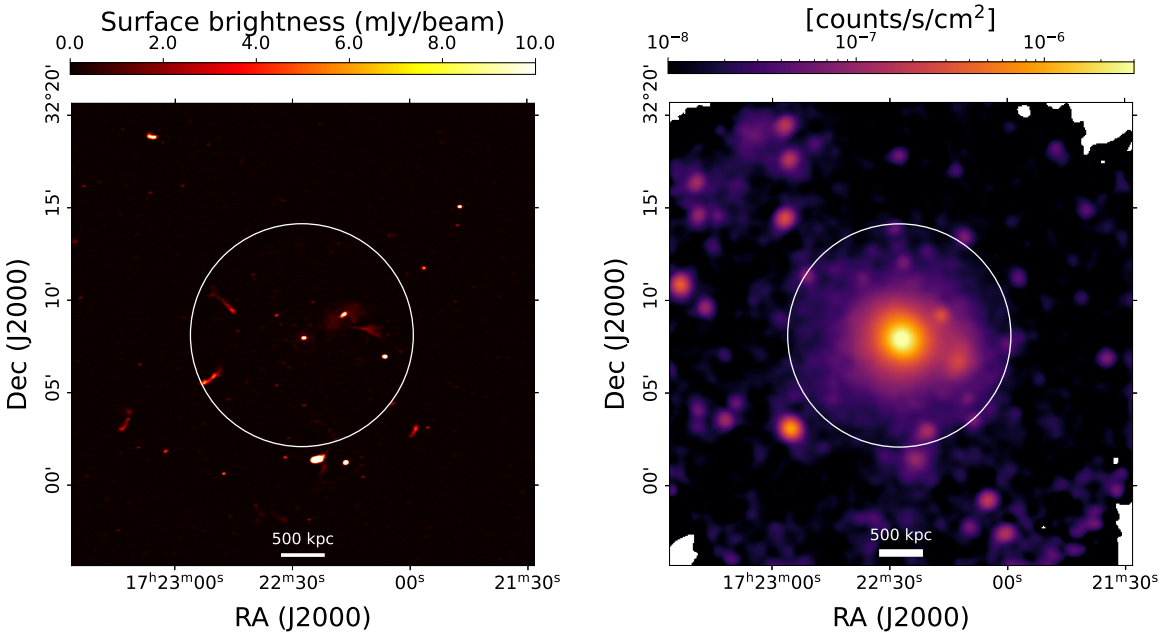

Figure 3.5: *Left*: the cluster Abell 2261 at 144 MHz at a resolution of 6″. *Right*: the same cluster seen from XMM-Newton. The white circles are representing r_{500}.

to a group and hence to a minor merger (Savini et al. 2019). The results from Savini et al. (2019) show a spectral index of $\alpha = 1.7 \pm 0.3$, making this a candidate ultra steep spectrum halo. These results are not consistent with the ones from the LoTSS-DR2, because of a strong source that could not be properly subtracted.
Allen (2000) classified this as a cool-core cluster (see also Sommer et al. 2017) while Bildfell et al. (2008) found a small level of substructures and a low value of the centroid shift w. The high resolution (6″) radio image and the XMM X-ray band image are shown in Fig. 3.5.

Chapter 4

LOFAR Two Meter Sky Survey

The LOw Frequency ARray (LOFAR; van Haarlem et al. 2013) is a low-frequency radio interferometer able to observe in the frequency range $10 - 240$ MHz. The array is divided into 52 stations, of which 38 are located in the Netherlands and 14 *international* stations that are scattered across Europe. Of the 38 dutch stations, 24 are concentrated in an area called the *core* and 14 are spread over the Dutch territory, constituting the *remote* stations which guarantee baselines of at most 100 km, while the international stations have maximum baselines of around ~ 1000 km.
In Fig. 4.1 we can see on the left an aerial photograph of a region of the *core*, called the *Superterp*, where there is the highest concentration of antennas, and on the right all the sites of already built and planned stations across Europe.
The antennas are divided in two types: low band antennas (LBA), that observe in the range $\nu = 10 - 90$ MHz, and high band antennas (HBA), observing in the range $\nu = 110 - 240$ MHz.

Figure 4.1: *Left*: aerial photograph of the "Superterp", in the central part of the LOFAR core, showing the distribution of both HBA and LBA antennas. From van Haarlem et al. (2013). *Right*: international distribution of the LOFAR stations across Europe, considering also the station under construction (and planned). Credits: ASTRON, https://www.astron.nl/telescopes/lofar/.

LOFAR has a very large field of view, making it optimal for full sky surveys, and thanks to the *remote* stations it is the very first low frequency interferometer with a high resolution, reaching up to $\sim 6''$. Combining *remote* and *international* stations it is possible to reach sub-arcsecond resolution, as low as $\sim 0.3''$, the resolution in function

of the frequency and baseline is shown in Table 2 in the ASTRON Science website[6]. The *core*, instead, allows the observation of the largest scales on the sky, thanks to the very short baselines, especially in the low frequency range. In fact, an interferometer is characterized by the resolution, defined through following formula:

$$\theta_{min} \approx \frac{\lambda}{b_{max}} \tag{4.1}$$

where λ is the observing wavelength and b_{max} is the maximum baseline available; and by the largest recoverable scale, defined by:

$$\theta_{max} \approx \frac{\lambda}{b_{min}} \tag{4.2}$$

where λ is the observing wavelength and b_{min} is the minimum baseline of the array. Since many astrophysical radio sources are optically thin and emit radiation from synchrotron process (hence the spectral energy distribution is defined by a decreasing power-law in function of the frequency), LOFAR can easily observe such sources, where the flux density is higher than at higher frequencies. It is also the best instrument to observe ultra steep spectrum sources, since their cut-off frequencies happen at frequencies higher than the LOFAR observing ones, making it the best instrument to observe both low efficiency acceleration sources and aged cosmic rays in extra-galactic sources, in fact, with LOFAR it has been possible to discover radio bridges, GReETs and megahalos (see Section 2.3).

The data used in this project are from the Second LOFAR Two Meter Sky Survey data release (LoTSS-DR2; Shimwell et al. 2017, 2022). The observations are carried out in the frequency range $120 - 168$ MHz, with a central frequency of 144 MHz. For this project, we focused on the second Planck catalog of SZ sources (PSZ2; Planck Collaboration et al. 2016), the total number of these sources observed in the LoTSS-DR2 is 309 (Botteon et al. 2022). These clusters span a redshift and mass ranges of $0.016 < z < 0.9$ and $1.1 \cdot 10^{14}\ M_{\odot} < M_{500} < 11.7 \cdot 10^{14}\ M_{\odot}$ respectively. We can see the entire sample in Fig. 3.1.

Each observation of the LoTSS is generally 8 hours long, reaching a root-mean-square (rms) value of $\sigma_{rms} \sim 0.1$ mJy/beam. Each pointing has a full width half at half maximum of 3.96° with a separation of $\sim 2.6°$, meaning that targets may be covered by up to three pointings, which are then combined together for the analysis.

The data were calibrated by the LOFAR Survey team with the pipelines built for the LOFAR Key Science Project, the process is described in Tasse et al. (2021) and Shimwell et al. (2019, 2022). The calibration is not done using only the observations from LOFAR, this is due to the inaccuracies in the beam model and to the ionospheric directional effects that cause offsets in the flux scale (Hardcastle et al. 2016). To solve this problem, the measured fluxes are scaled to the ones reported in the Roger et al. (1973) scale. In order to apply this correction, a cross-match with the NRAO VLA Sky Survey (NVSS; Condon et al. 1998) catalog is needed, where there is the assumption of a global scaling relation between the NVSS and the 6C catalog (Hales et al. 1988, 1990), which is thought to be consistent to 5% to the results of Roger et al. (1973). After these corrections, it is possible to analyze the data and get the correct flux measurements.

[6] https://science.astron.nl/telescopes/lofar/lofar-system-overview/observing-modes/lofar-imaging-capabilities-and-sensitivity/

To better improve the calibration for specific targets with an area much smaller with respect to the LOFAR field of view, the post-processing scheme of "extraction + self-calibration" from van Weeren et al. (2021) has been applied. As explained briefly in Botteon et al. (2022), this consists in the subtraction from the *uv*-data of the sources outside a square region with an area less than ~ 1 deg^2 containing the target. After the subtraction, the solutions of the direction-dependent calibration are applied alongside with the sky model that are obtained in the first steps of the calibration. The resulting data are phase-shifted to the center of the region, averaged and then corrected for the beam. After this a series of phase and amplitude loops is performed and the process is completed with a final self-calibration. The resulting images have a resolution of $6''$ and an rms of the order of 0.1 mJy/beam (see Table 3.1 for the rms of the targets of this work).
Botteon et al. (2022) classified the extended radio sources in radio halos, radio relics and candidates for both classes. They also searched in the archives of Chandra and XMM-Newton telescopes for past X-ray observations of these targets. These X-ray observations are used to compute the dynamical parameters, c and w, in order to get an estimate of the dynamical states of the targets.

4.1 A brief introduction to radio interferometry

In radio-astronomy the observational band ranges from 10 MHz to ~ 1 THz, where the low frequency limit is set due to the reflection of low frequency waves by the ionosphere and the higher limit is set by the atmospheric absorption (Condon & Ransom 2016). In the beginning radio observations were done with large single dish antennas, characterized by a resolution of $\theta_{res} \propto \lambda/D$, where λ is the observing wavelength and D is the diameter of the antenna, which means that to get a higher resolution at a specific frequency, we need very large collecting areas.

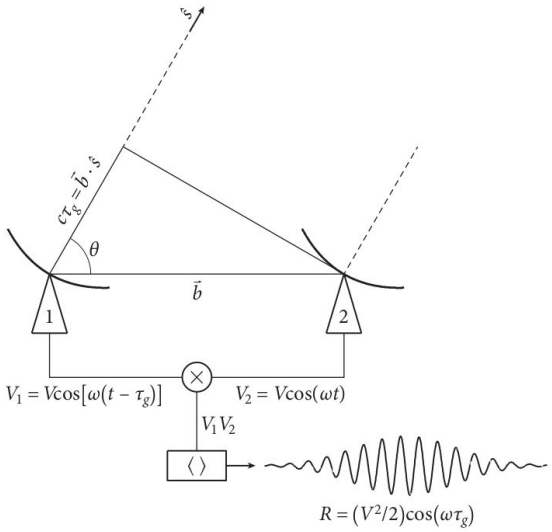

Figure 4.2: Scheme of a two antennas interferometer. From Condon & Ransom (2016).

A solution to this problem comes from interferometry, in which a number of N small dish antennas are used with correlated voltage outputs, with this we get a greater collecting area and a higher resolution, which is related to the maximum baseline between two antennas (see Eq. 4.1). If we consider a simple interferometer with only two

antennas (like the one shown in Fig. 4.2), separated by the baseline vector $\mathbf{b}$ linking Antenna 1 with Antenna 2. They observe the same source, whose direction is identified by the versor $\hat{s}$ and θ is the angle between $\mathbf{b}$ and $\hat{s}$, planar waves reach first Antenna 2 and after a time delay τ_g due to the geometry of the system:

$$\tau_g = \frac{\mathbf{b} \cdot \hat{s}}{c} \tag{4.3}$$

called also geometric delay. The outputs of the antennas are:

$$V_1 = V \cos(\omega(t - \tau_g)) \qquad V_2 = V \cos(\omega t) \tag{4.4}$$

A correlator then multiplies and averages over time the two output, resulting in the response $R_C = (V^2/2)\cos(\omega\tau_g)$. To recover the full power of the source, the sine correlator output is also computed, being $R_S = (V^2/2)\sin(\omega\tau_g)$. The correlator computes both components simultaneously, resulting in the complex correlator:

$$\mathcal{V} = R_C - iR_S = Ae^{-i\phi} \tag{4.5}$$

where $A = (R_C^2 + R_S^2)^{1/2}$ is the amplitude and $\phi = \tan^{-1}(R_S/R_C)$ is the phase. The response to a source with brightness distribution $I_\nu(\hat{s})$ of the complex correlator is called complex visibility, and it is described by the following expression:

$$\mathcal{V} = \int I_\nu(\hat{s}) \exp\{(-i2\pi\mathbf{b} \cdot \hat{s}/\lambda)\} \, \mathrm{d}\Omega \tag{4.6}$$

The three dimensional generalization for this expression is:

$$\mathcal{V}(u, v, w) = \int\int \frac{I_\nu(l, m)}{(1 - l^2 - m^2)^{1/2}} e^{-i2\pi[ul+vm+w(\sqrt{1-l^2-m^2}-1)]} \, \mathrm{d}l \, \mathrm{d}m \tag{4.7}$$

where (l, m) are cosine sky coordinates and (u, v, w) are the components of the baseline vector in wavelength units. The w component is in the $\hat{s_0}$ direction, which is the one that contains the source. In case of small field of views (FoVs) and high frequencies we can set $w = 0$ and simplify Eq. (4.7), making it an ordinary invertible Fourier Transform.
In the case of wide-field or low frequency interferometry, which are both cases of LOFAR, this term cannot be neglected and we need to take into account the sky curvature and the non-coplanar baselines, meaning that we cannot simply invert the transform. To produce the images we applied the *w-stacking* technique through the `WSClean` software (Offringa et al. 2014). In order to be able to reconstruct the brightness distribution we firstly factorize Eq. (4.7):

$$\mathcal{V}(u, v, w) = \int\int \frac{I_\nu(l, m) e^{-i2\pi w(\sqrt{1-l^2-m^2}-1)}}{(1 - l^2 - m^2)^{1/2}} e^{-i2\pi(ul+vm)} \, \mathrm{d}l \, \mathrm{d}m \tag{4.8}$$

With the w-stacking technique, the FoV is divided in small tiles enough for which the approximation $w = 0$ holds, and Eq. (4.8) becomes an invertible Fourier Transform for each tile, obtaining:

$$\frac{I_\nu(l, m)}{\sqrt{1 - l^2 - m^2}} = e^{i2\pi w(\sqrt{1-l^2-m^2}-1)} \int\int \mathcal{V}(u, v, w) e^{i2\pi(ul+vm)} \, \mathrm{d}u \, \mathrm{d}v \tag{4.9}$$

then, to reconstruct the sky signal we integrate over every value of w, resulting in:

$$\frac{I_\nu(l,m)(w_{max}-w_{min})}{\sqrt{1-l^2-m^2}} = \\ = \int_{w_{min}}^{w_{max}} e^{i2\pi w(\sqrt{1-l^2-m^2}-1)}\mathrm{d}w \int\int \mathcal{V}(u,v,w)e^{i2\pi(ul+vm)}\ \mathrm{d}u\ \mathrm{d}v \quad (4.10)$$

With this approach we can recover $I_\nu(l,m)$ in the case of large field of views and low frequencies, overcoming the assumption of the planar sky.

Chapter 5

Data analysis and results

In this Chapter we will discuss the approach followed to produce the images used in this work alongside with the methods used to study megahalos and to derive the upper limits for this emission. We will also present our results obtained from the analysis, such as the main properties of the radio halos, megahalos and the derived upper limits for the emission.

5.1 Procedure

The analysis starts from the LoTSS-DR2 data that are already calibrated, extracted, self-calibrated and corrected for the flux by the LOFAR Survey team.
We produce the images using the `WSClean` code v3.5, taking advantage of the `multiscale` and `multifrequency` algorithms (presented by Offringa & Smirnov 2017).
The `multiscale` algorithm uses Gaussian components with different sizes to model the emission, this is based on the approach presented by Cornwell (2008), in which it is assumed that the sky brightness is a sum of scaled and centered extended Gaussian components. The `multifrequency` algorithm accounts for the spectral variation of the beam and sources responses; `WSClean` divides the frequency range in sub-bands of equal width and measures the beam variation starting from the integrated image and computing the flux density in the sub-bands. In this work, we follow the approach described in Shimwell et al. (2022) and Botteon et al. (2022) and divide the *uv*-data in 6 channels, each with a width of 8 MHz. We produce two sets of images, where in the first case we produce the image by cleaning the data with no cleaning masks and setting the stopping criteria to 15000 iterations only. This shallow initial clean has the purpose of creating a cleaning mask, to be used in the second iteration. The second set of images is done through a deeper clean loop, with the application of a cleaning mask created over the previous images, cleaning only where the brightness is greater than $4\sigma_{rms}$. For these images, we increased the number of threshold iterations to 100000 and added a stopping criterion on the maximum brightness, stopping the process when the maximum brightness is less than $2\sigma_{rms}$. All of our images are cleaned until they reach the second criterion, reaching the threshold set on the noise. This procedure is followed for every image produced.
To search for megahalos, we have to remove from the *uv-data* all the discrete sources embedded and projected onto the cluster. The procedure that we followed is summarized in Fig. 5.1 and in the following sections we will describe each step of the process in detail.

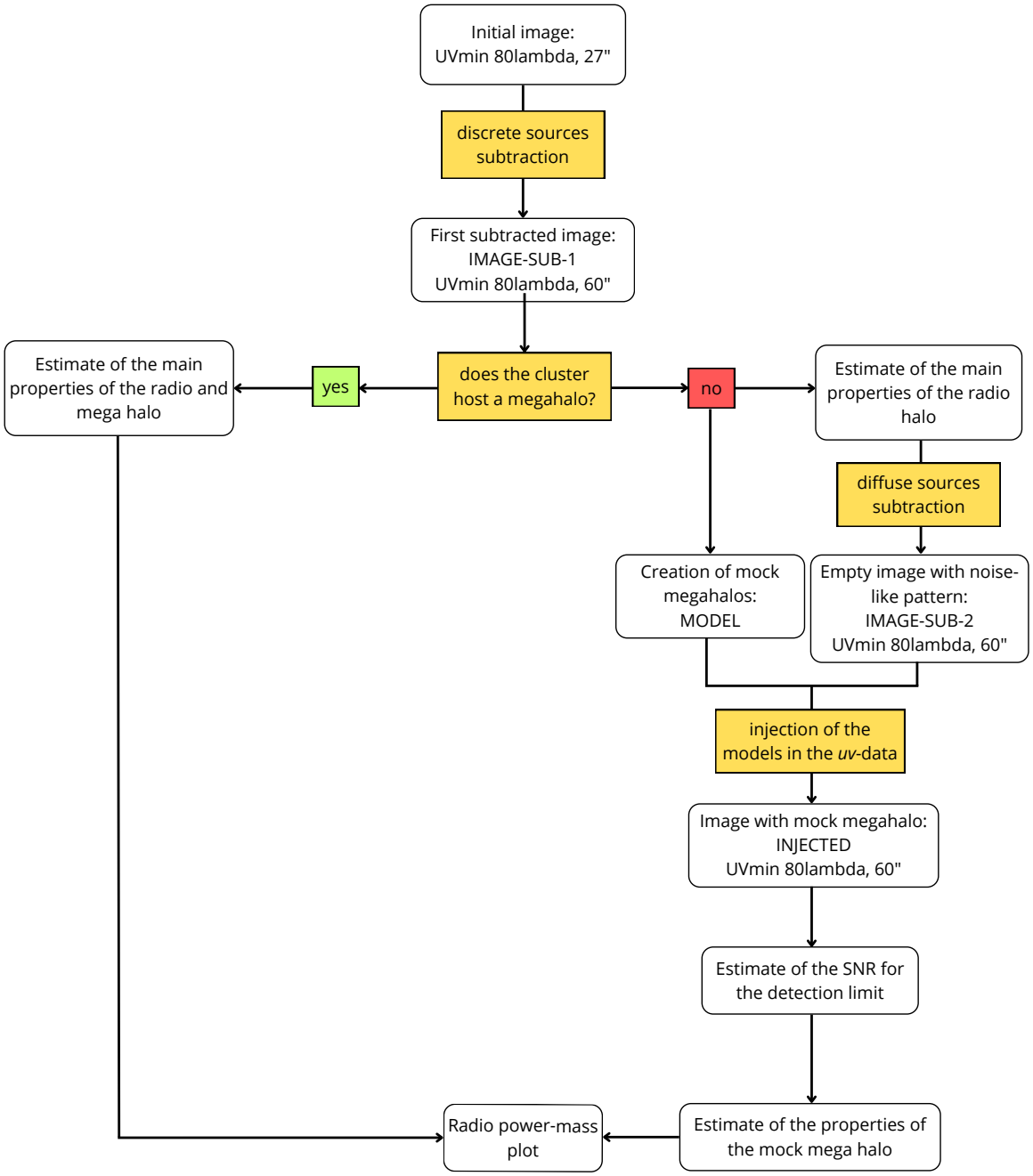

Figure 5.1: Simple scheme summarizing the procedure followed to analyze the four clusters and derive their main properties.

Step 1: initial image

In this first step, we produce a low resolution image with a Gaussian taper of 100 kpc ($\simeq 27''$) and a Briggs weighting scheme (Briggs 1995) with `robust = -0.5` (which is the standard used in the LoTSS). In this step we set a *uv*-cut in λ units, where in this case it corresponds to r_{500}. In this way, we can image only the sources smaller than this scale by cutting out the shorter baselines that are used to detect the emission on larger scales. During this step, the `CLEAN` algorithm outputs both the cleaned image and the model components of the sources. Since we used a high *uv*-cut, our model contains only the discrete sources that we need to subtract to be able to observe the

underlying low brightness diffuse sources (e.g. the radio halos). With the production of this first image ends the first step of our procedure to search for megahalos in galaxy clusters. An example image is shown in Fig. 5.2.

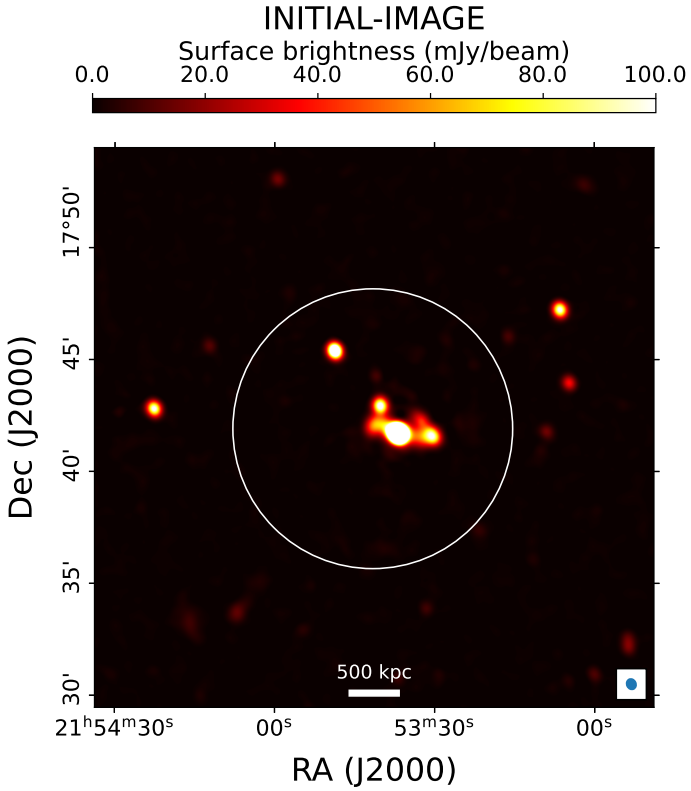

Figure 5.2: Image of the cluster A2390 at 27″ (∼ 100 kpc) of resolution before the subtraction of the discrete sources, the white circle represents r_{500}.

Step 2: first subtraction and properties of diffuse emission

The second step leads to the production of an image without discrete sources and to the estimate of the main properties of the diffuse emission, if present. To subtract all the discrete sources from the image, we Fourier transform the resulting model from the first step into the visibilities and then subtract it from the *uv*-data, saving the results in a new data column. This procedure leaves the diffuse emission almost completely unaffected because, as we said in the previous step, the model is based only on the discrete sources of the initial image. After the subtraction process, we first produce an image with the same parameters as the image in **Step 1** to visually inspect it and verify that every discrete source has been correctly removed, we see an example in the left panel of Fig. 5.3. We then produce a new image (IMAGE-SUB-1 in the scheme in Fig. 5.1), with a low resolution of 60″ (corresponding to ≈ 222 kpc), to increase the sensitivity to faint diffuse emission. An example of this is shown in the right panel of Fig. 5.3. To produce this image, we used the same Briggs weighting of the first image but a much lower *uv*-cut, set to 80λ, to take advantage of most of the shorter baselines which are sensitive to the extended emission thanks to the higher maximum recoverable scale (see Eq. 4.2). The *uv*-cut is set to 80λ, because we noticed that with lower cuts (or even with no *uv*-cut) strong patterns, related to either noise or Galactic

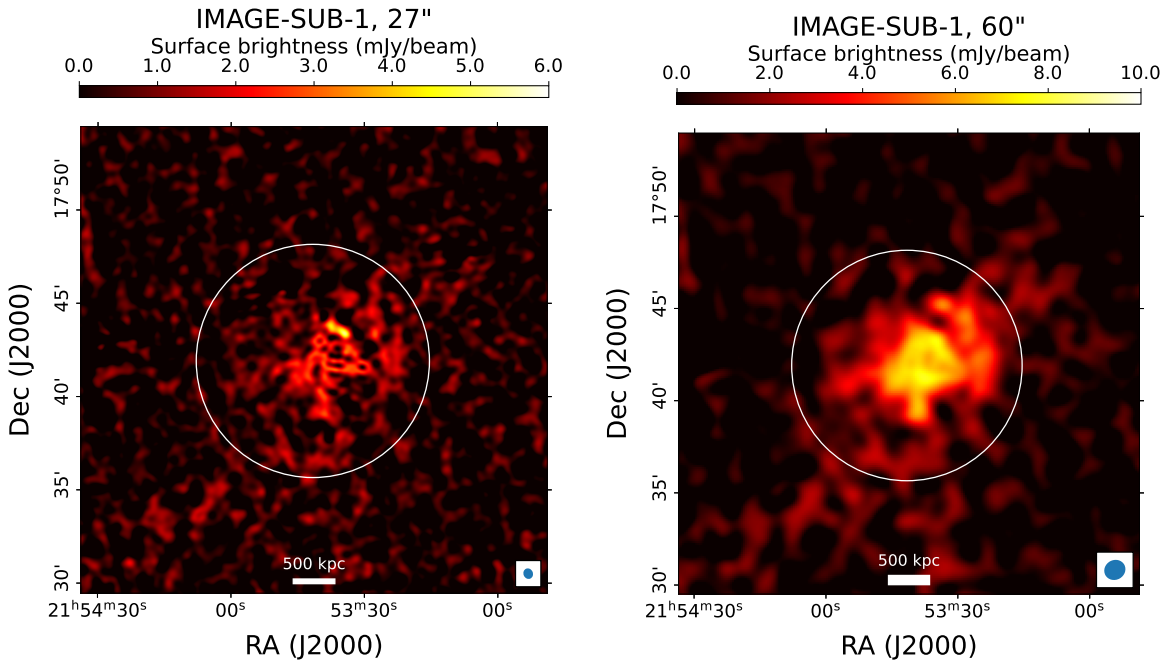

Figure 5.3: Example images after the subtraction of the discrete sources in the cluster A2390, on the left we have the image at a resolution of 27″ (≈ 100 kpc), on the right the low resolution (60″ ≈ 200 kpc)). The white circle represents r_{500}.

emission, appear in the images, being most noticeable at low (60″) and ultra-low (120″) resolutions. This has also been reported by Bruno et al. (2023), where it is explained that shorter spacings are more difficult to calibrate and can sample emission of the Galaxy on large angular scales.
If diffuse emission is observed in this step, we analyze it and retrieve its main properties, such as surface brightness, size, flux density, radio power and emissivity. We describe the process followed to derive the main properties of the radio halos in Section 5.1.1.
After the end of the cleaning algorithm, we are, once again, left with the cleaned image and the model of the diffuse emission.

Step 3: second subtraction

In this very short step we follow the same subtraction procedure of the first subtraction, but we subtract the model of IMAGE-SUB-1 from the *uv*-data after it has been Fourier transformed in the visibilities. This step is done only if we have to derive an upper limit to the megahalo emission, hence it is not done for A2219 as we will explain the following sections. In this case we remove all the diffuse sources from the *uv*-data, leaving us with an image with no sources and a noise-like pattern, this is referred to as IMAGE-SUB-2 in the scheme in Fig. 5.1. An example of this noise-like image can be observed in the left panel of Fig. 5.4.

Step 4: creation and injection of mock megahalos

After the second subtraction, we need to derive the upper limits for the megahalo emission through the injection of modeled megahalos in the *uv*-data. For the mock megahalos we consider a flat surface brightness distribution, approximating the profiles found by Cuciti et al. (2022), since we noticed that it is not possible to fit the

megahalos found in the study with an exponential function. The constant surface brightness should still be a good first approximation of the distribution considering its very slow decrease in function of the distance (see left panel in Fig. 2.7). We set a radius of $\sim$ 2.5 Mpc for the mock megahalos, which is based on the megahalo found in Abell 2219 (as we will see in Section 5). These models depict a circular megahalo centered in the SZ center of the cluster (reported in Botteon et al. 2022), an example of a modeled megahalo is shown in the central panel in Fig. 5.4.

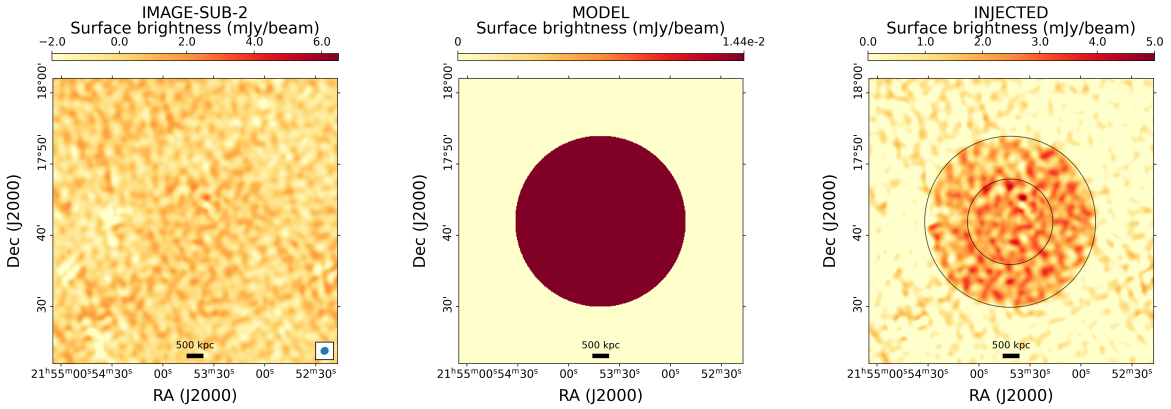

Figure 5.4: Images showing the last three steps of the injection procedure in case of missing megahalo emission. *Left*: image after the second subtraction, all sources have been subtracted and the image shows a noise-like pattern. *Center*: example of the model that is Fourier transformed and injected in the visibilities. *Right*: example of a clean image after the injection of the model shown in the central panel. We injected a model with a high surface brightness to highlight the results of this process. The black annulus shows the region that we used to derive the SNR from the various images.

We produce twenty images to model mock megahalos, with the injected surface brightness ranging from $I = 0.01$ μJy/arcsec^2 to $I = 0.20$ μJy/arcsec^2 with jumps of $\Delta I = 0.01$ μJy/rcsec^2. The brightness range is extrapolated from the profiles shown in Cuciti et al. (2022), to start from values of a real case scenario. In turn, all the models are Fourier transformed and added to the visibilities before producing the clean image. An example image is shown in the right panel of Fig. 5.4, where a model with $I = 0.4$ μJy/arcsec^2 has been injected, just for the purpose of clearly showing the injection procedure.
This part of the procedure is highlighted by the box INJECTED in the scheme in Fig. 5.1, and the final images are produced with a resolution of 60″ and a *uv*-cut of 80λ. The mock megahalos are used to determine the detection limit through the signal-to-noise ratio (SNR) computed in a region between r_{500} and $r = 2.5$ Mpc, which we can see in black in the right panel in Fig. 5.4. We consider this annular region to add a size constraint to the detection of the emission, as all these clusters host a giant radio halo extending up to $\sim r_{500}$ (as we will see in Section 5). The SNR is computed through the following expression:

$$SNR = \frac{S}{\sqrt{(\sigma_{rms} \cdot \sqrt{N_{beam}})^2 + (S \cdot \delta_{cal})^2}} \tag{5.1}$$

where S is the total flux in the region of interest, $\delta_{cal} = 0.1$ is the calibration error (Botteon et al. 2022), σ_{rms} is the rms noise of the image and N_{beam} is the number of beams in the region. The detection limit in this work is set at $SNR = 5$.

5.1.1 Estimate of the main properties of the diffuse emission

If a radio halo is found after the first subtraction, we produce the surface brightness profile to asses the properties of the emission. Then, we fit an exponential function to the brightness profile (see Eq. 2.16) and derive the central surface brightness I_0 and the effective radius r_e of the radio halo. We estimate the flux densities and radio powers at 144 MHz and also the k-corrected values at 150 MHz[7] through the relation:

$$S_{150\ \mathrm{MHz}} = S_{144\ \mathrm{MHz}} \left(\frac{144\ \mathrm{MHz}}{150\ \mathrm{MHz}} \right)^{\alpha} \tag{5.2}$$

where α is assumed positive from the convention $S_\nu \propto \nu^{-\alpha}$.
Once the effective radius and the central surface brightness are estimated, we can compute the total flux density by applying the formula described by Murgia et al. (2009):

$$S_\nu = 2\pi f r_e^2 I_0 \quad [\mathrm{Jy}] \tag{5.3}$$

where r_e is in arcsec, I_0 in Jy/arcsec^2 and $f = 0.8$, meaning that the computation is up to $3r_e$. The errors associated with the flux density are computed through the following formula:

$$\Delta S = \sqrt{(\sigma_{rms} \cdot \sqrt{N_{beam}})^2 + (S \cdot \delta_{cal})^2} \tag{5.4}$$

where N_{beam} is the number of beams in the area, S is the total flux density inside the same area and $\delta_{cal} = 10\%$ is the calibration error (Shimwell et al. 2022, Botteon et al. 2022). We did not consider the uncertainty related to the source subtraction that is described in Botteon et al. (2022) because the error would still be dominated by the calibration uncertainty, and the computation of each source contribution to the different radial annuli would be of high complexity.
The radio power is computed using the following formula:

$$P_\nu = 4\pi S_\nu D_L^2 (1+z)^{\alpha-1} \quad [\mathrm{W/Hz}] \tag{5.5}$$

where D_L is the luminosity distance of the source and α is its spectral index. In case we do not know the spectral index of radio halos, we assume $\alpha = 1.3$ (Feretti et al. 2012, van Weeren et al. 2019), while for the megahalo emission we assume $\alpha = 1.6$ (Cuciti et al. 2022). We compute also the emissivity at 1.4 GHz for both radio halos and megahalos (considering also the mock megahalos) to compare them with the typical values found for radio halos. In the case of the radio halos, we compute the emissivity following Murgia et al. (2009):

$$\langle J_\nu \rangle \simeq 7.7 \times 10^{-41} (1+z)^{3+\alpha} \cdot \frac{I_0}{r_e} \quad [erg/s/cm^3/Hz] \tag{5.6}$$

where I_0 is in μJy/arcsec^2 and r_e is in kpc. The term $(1+z)^{3+\alpha}$ takes into account both the surface brightness cosmological dimming and the k-correction. This follows the assumption that all the flux density comes from a sphere with radius $3r_e$. For megahalos, instead, we follow the approach described in Cuciti et al. (2022), where the volume averaged emissivity is given by:

$$J_\nu = \frac{P_\nu}{\frac{4}{3}\pi R^3} \tag{5.7}$$

[7] which are the values reported through this thesis to keep continuity with the LoTSS papers.

where P_ν is the radio power and R is the radius of the source. The assumption here is that the whole emission comes from a sphere of radius R.

Since megahalos are not spherical, in the general case the radii are computed using the formula $R = \sqrt{r_{min} \cdot r_{max}}$, where r_{min} and r_{max} are the largest and smallest radii delimited by the 3σ contours in an image with a resolution of $2'$, while for mock halos the radius is known a priori. In Cuciti et al. (2022) it is assumed that megahalos might be co-spatial with radio halos in the central region, therefore to estimate the total flux density of a megahalo, we measure the average surface brightness in a region of the megahalo that does not include the radio halo and we multiply it by the total area inside the 3σ contours.
After estimating the properties of the radio halos we compare them with the results computed through the Halo-Flux Density CAlculator (`Halo-FDCA`; Boxelaar et al. 2021).

If we detect megahalo emission in a cluster, we produce also its surface brightness profile and estimate the flux density by subtracting the radio halo flux density from the total measured flux density in a region containing both the radio halo and the megahalo and use this result to compute the radio power. If a megahalo is not detected after **Step 2**, we continue with the already described **Step 3** and **Step 4** of the analysis to derive the upper limits for the emission through the injeciton of mock megahalos in the visibilities. After measuring the SNR for the different injections, we select the image for which the detection results in $SNR = 5$ and produce the recovered surface brightness profile of the modeled megahalo to study its observed behaviour in a "true case scenario", comparing it with the known megahalo profiles. We also compare the recovered flux density and radio power with the injected ones, to understand how much flux density is recovered in the image with respect to the injected one.

In the following sections, we explain in detail the procedure used for each cluster.

We report the main results of our analysis, showing the results of the best-fitted models alongside with the main properties of the emission, such as flux density, radio luminosity and emissivity of both radio halos and megahalos. For the injected megahalos we report their surface brightness, the recovered flux density and the recovered power alongside with the injected values. All the flux densities and radio luminosities that are reported are computed at 150 MHz.

Abell 2219

After carefully removing all the sources with a size smaller than r_{500} from the visibilities, we produced a low resolution image ($60''$) of the cluster. In the left panel of Fig. 5.5 we show the low resolution image, where we clearly detect a new megahalo, extending beyond r_{500}, while in the right panel we show the surface brightness profile.

Through the best-fit of the halo surface brightness, we determined the parameters of the halo exponential profile being $I_0 = 8.76 \pm 1.6$ μJy/arcsec^2 and $r_e = 369 \pm 29$ kpc. Using the formula from Murgia et al. (2009) and integrating up to $3r_e$, the measured flux density is $S_{150\ \mathrm{MHz}} = 427 \pm 103$ mJy, which corresponds to a radio power of $P_{150\ \mathrm{MHz}} = (7.0 \pm 1.7) \cdot 10^{25}$ W/Hz. The emissivity of the radio halo at 1.4 GHz is $J_{1.4\ \mathrm{GHz}} = (4.4 \pm 0.9) \cdot 10^{-42}$ erg/s/cm^3/Hz.

Since we were not able to fit the megahalo profile with an analytic function, to determine the flux of the megahalo we measured the entire flux in a region covering both the radio and the megahalos, hence up to ~ 2.5 Mpc, and then subtract the flux of the radio halo. This process carries great uncertainty since we do not know precisely

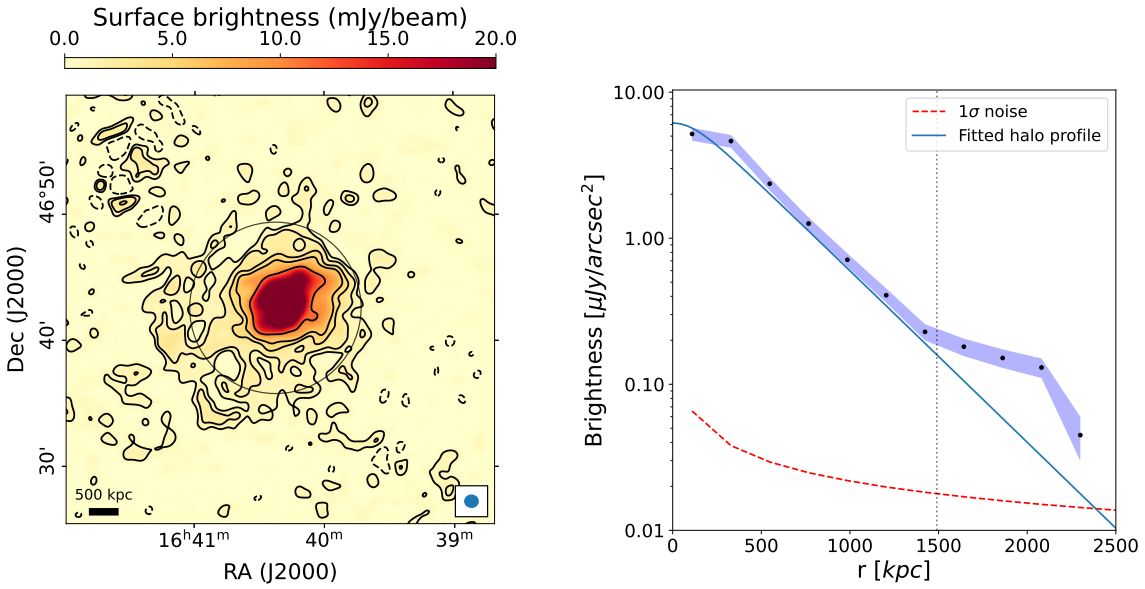

Figure 5.5: *Left*: low resolution image of Abell 2219 showing the radio halo and the megahalo. The black circle delimits r_{500}. The contours are set at levels $[-3, 2, 4, 8, 12, 24] \cdot \sigma_{rms}$, where $\sigma_{rms} = 0.45$ mJy/beam. *Right*: surface brightness profile of the radio halo and megahalo. The solid line is the best fit of the halo emission, the vertical line is r_{500} and the red dashed line is 1σ detection limit of the surface brightness for each annulus. The surface brightness is computed in annuli of width $60''$ centered on the cluster.

where is the transition from the radio halo to the megahalo emission. Despite this, it is the same approach that has been applied to the other known megahalos, since it is the best way to remove the contribution from the radio halo emission.

By analyzing the surface brightness profile[8] in Fig. 5.5 we can see how the radio halo is more extended than $3r_e$ and that the transition from radio halo to megahalo happens at around $4r_e$ (~ 1.48 Mpc). Hence, we estimate the megahalo flux density in a region starting from $4r_e$ up to ~ 2.5 Mpc. Due to the uncertainties on the true size of the megahalo and of the radio halo, we estimated the flux density in two extreme cases obtaining a flux range for the emission, in this way we manage to remain conservative in our estimates. In the first case, to get the lower limit of the flux density, we subtracted the radio halo from the *uv*-data after first carefully masking out of the model what we thought is the megahalo, then we measured the remaining flux density in the region between $4r_e$ and 2.5 Mpc. To derive the upper limit to the megahalo flux density, we computed analytically the flux of the radio halo by integrating the exponential profile up to $4r_e$ and subtracting it from the measured flux density in a circular region centered on the cluster and extending up to the radius of the megahalo. We also computed the flux density of the radio halo by measuring it directly from the image, in a region centered on the cluster and extending up to $4r_e$. This flux density is then subtracted from the one measured in the region covering the entire megahalo, as in the previous case. The upper limit is set by the highest of these two resulting flux densities, while the other one is considered as nominal value of the megahalo. From this analysis, we derive a megahalo flux density at 150 MHz of $S_{MH} = 95$ mJy while the lower and upper limits of the range are $S_{low} = 57$ mJy and $S_{up} = 146$ mJy respectively.

[8] which has been produced by excluding the residuals of a badly subtracted source in the North-East region of the cluster, since it would alter the resulting profile.

The corresponding radio powers are $P_{MH} = 1.7 \cdot 10^{25}$ W/Hz for the nominal value, while the limits are $P_{low} = 9.9 \cdot 10^{24}$ W/Hz and $P_{up} = 2.5 \cdot 10^{25}$ W/Hz. Following what was done in Cuciti et al. (2022), we assumed that the megahalo occupies also the same region of the radio halo. As a best estimate, we took the average surface brightness of the halo and multiplied it by the area inside $4r_e$ to obtain the flux density and then added it to the already computed one. In this case the total flux density of the megahalo is $S_{150\ \mathrm{MHz}} = 130 \pm 82$ mJy, while the correspondent radio power is $P_{150\ \mathrm{MHz}} = (2.3 \pm 1.4) \cdot 10^{25}$ W/Hz.
To compute the volume averaged emissivity we use Eq. (5.7), in which the radius is defined as $R_{MH} = \sqrt{r_{min} \cdot r_{max}}$, where r_{min} and r_{max} are the minimum and maximum radii of the megahalo respectively, measured within the 3σ contours from the image with a resolution of $2'$. This resulted in a radius $R_{MH} = 2089 \pm 130$ kpc. Through these results we obtain the emissivity at 1.4 GHz at $J_{1.4\ \mathrm{GHz}} = (5.6 \pm 3.7) \cdot 10^{-45}$ erg/s/cm^3/Hz, which is two orders of magnitude lower than the average emissivity of radio halos.

Abell 2390

After the subtraction of the sources we found evidence of the radio halo reported by Sommer et al. (2017), as we can see from Fig. 5.6. The radio halo radial profile fit shows a central brightness of $I_0 = 1.95 \pm 0.22$ μJy/arcsec^2 and an effective radius $r_e = 478 \pm 38$ kpc. This results in a flux density of $S_{150\ \mathrm{MHz}} = 152 \pm 30$ mJy and a radio power of $P_{150\ \mathrm{MHz}} = (2.8 \pm 0.6) \cdot 10^{25}$ W/Hz. The emissivity computed at 1.4 GHz for the radio halo is $J_{1.4\ \mathrm{GHz}} = (8.2 \pm 1.1) \cdot 10^{-43}$ erg/s/cm^3/Hz.

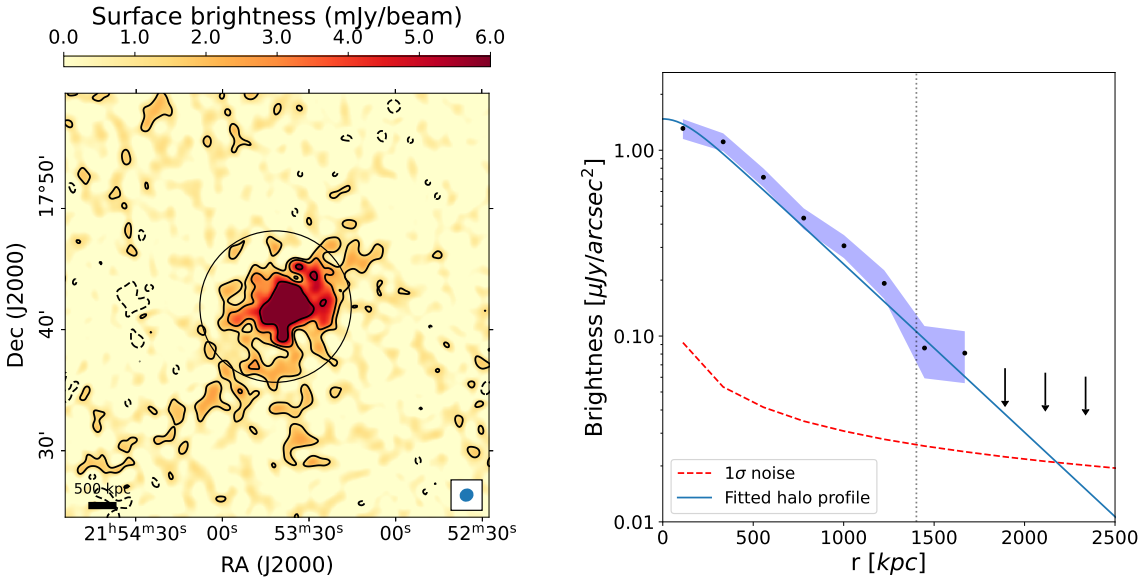

Figure 5.6: *Left*: low resolution image of Abell 2390 showing the radio halo. The black circle is r_{500}. The contours are set at levels $[-3, 2, 4, 8, 12, 24] \cdot \sigma_{rms}$, where $\sigma_{rms} = 0.65$ mJy/beam. *Right*: surface brightness profile of the radio halo. The solid line is the best fit of the emission, the vertical line is r_{500} and the red dashed line is 1σ detection limit of the surface brightness for each annulus.

Then, we used `Halo-FDCA` to fit the data with a simple circular model estimated through the Monte Carlo-Markov Chain, which is also able to get a robust estimate of the uncertainties of the various parameters. It resulted in a central surface brightness of

$I_0 = 2.37 \pm 0.16$ μJy/arcsec^2 and an effective radius of $r_e = 452 \pm 25$ kpc, which are both consistent with our results within the errors. The results of this second fitting procedure can be seen in Fig. 5.7. The residual image shows that the fitted circular model is a good approximation and that the arc-like shaped emission in the North-West of the cluster might not be part of the radio halo, but possibly related to residual emission from a subtracted source.
Although we can see some extended emission outside of r_{500}, we cannot claim this as a megahalo as it is not detected at least at the $3\sigma_{rms}$ level, we think that this might be a hint of extended emission, although the quality of the data and the sensitivity are not enough to confirm this. We also noticed that with a uv-cut of 150λ this emission becomes fainter, making it possibly related to interference at shorter baselines. Deeper observations or an increased sensitivity will allow us to understand if this is actually emission or if it is related to a non optimal calibration of the short baselines.
We then subtracted the remaining emission to obtain an empty image over which we inject our models (see left and central panels of Fig. 5.4). As we already said, we produced different models with the surface brightness ranging from 0.01 μJy/arcsec^2 to 0.2 μJy/arcsec^2 with steps of 0.01 μJy/arcsec^2. After the injection, we measured the SNR in every image in which we injected the mock megahalos, selecting the one at the threshold value of $SNR = 5$, the relation between the measured SNR and the surface brightness of the correspondent model is shown in Fig. 5.8. In the figure we can see a jump in the surface brightness between 0.07 muJy/arcsec^2 and 0.08 μJy/arcsec^2, this might be related to what happens in the cleaning process, where the model with higher brightness is better cleaned and more flux density is recovered. We observe the same behavior in the case of A2261, shown in Fig. 5.18. For this cluster we find the surface brightness upper limit to be of $I = 0.07$ μJy/arcsec^2. After finding the model that satisfies the requirements, we measure the injected and recovered flux densities and the correspondent luminosities. The injected flux density is $S_{inj} = 79$ mJy, which corresponds to a radio power of $P_{inj} = 1.5 \cdot 10^{25}$ W/Hz, while the recovered flux density and power are $S_{rec} = 48 \pm 10$ mJy and $P_{rec} = (8.7 \pm 1.9) \cdot 10^{24}$ W/Hz. The recovered flux density is $\sim 2/3$ of the total injected flux density in the region.
If we consider the flux density in the entire injection region, the injected flux density is $S_{inj} = 106$ mJy with a radio power $P_{inj} = 2 \cdot 10^{25}$ W/Hz. The recovered values are $S_{rec} = 87 \pm 15$ mJy and $P_{rec} = (1.6 \pm 0.3) \cdot 10^{25}$ W/Hz. This means that in this case the recovered flux is $\sim 80\%$, while in the annular region the recovered fraction is $\sim 60\%$.
We then produced the surface brightness profile of the recovered emission and overlayed it with the halo profile and, as we can see from Fig. 5.9, we get a 3σ detection in the surface brightness considering also the errors.
Following what we did for the megahalo in A2219, we measured the emissivity of the injected megahalo, this time without having to measure the size or the surface brightness since they are known a priori. The emissivity of the mock halo at 1.4 GHz is $J_{1.4\ \mathrm{GHz}} = 2.3 \cdot 10^{-45}$ erg/s/cm^3/Hz, which is similar to the one of known megahalos.

Abell 1763

After the subtraction of the sources we found a new radio halo in this cluster, which was not detected with the GMRT at 610 MHz (Venturi et al. 2008). As we can see from Fig. 5.10, the emission is not circular but it has an almost ellipsoidal shape. Because of this, we could not perform the fit through concentric annuli as done for the other clusters. For this reason, we only use the `Halo-FDCA` algorithm, assuming a rotated

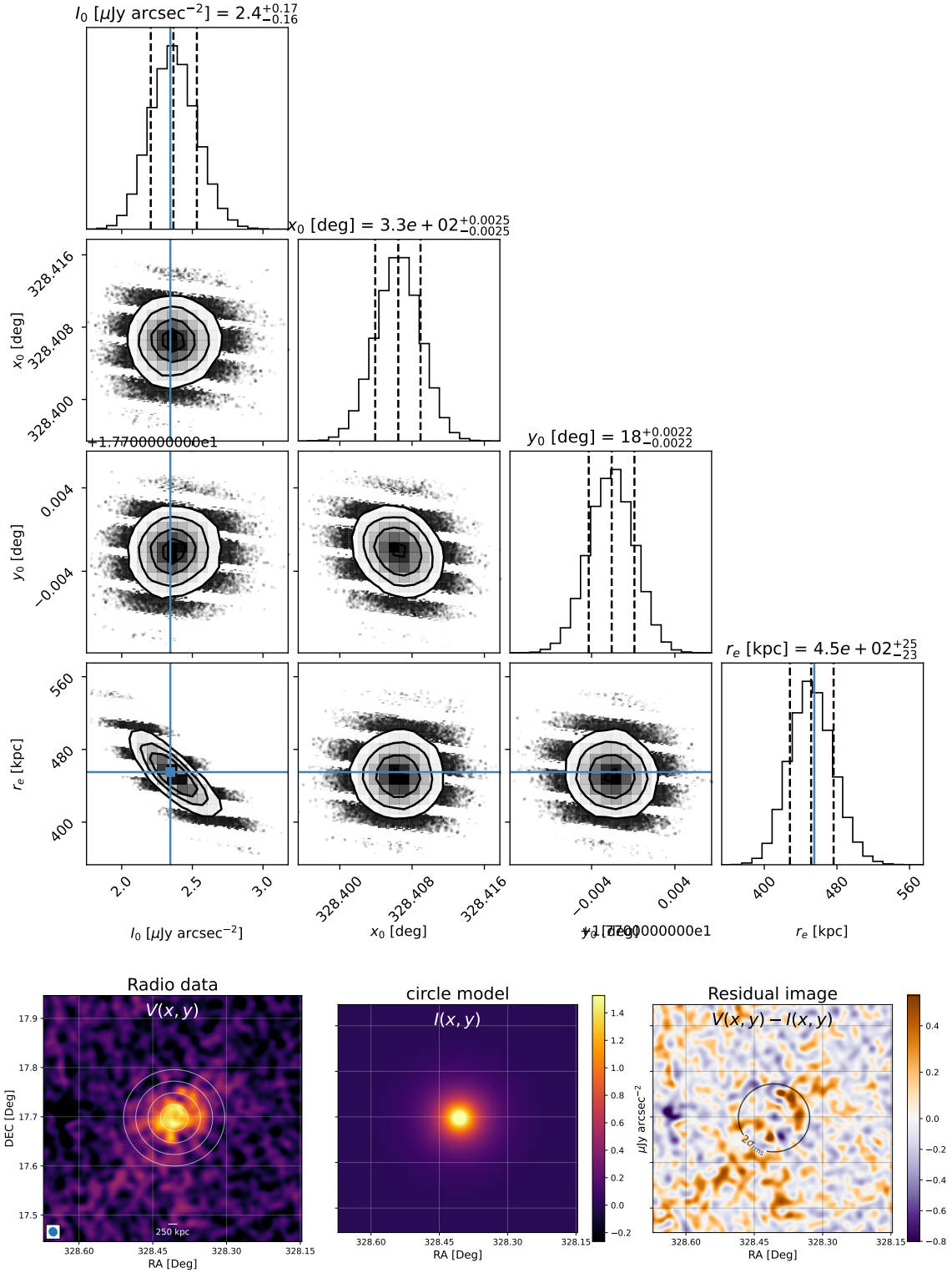

Figure 5.7: Results from Halo-FDCA for Abell 2390. *Top*: corner plot resulting from Halo-FDCA showing the distribution of the variables. *Bottom*: data used for the fit (left) with the contours of the best-fitted model (center), on the right the residuals of the fit are shown. The scale of the residuals is the same of the data and model, which is μJy/arcsec^2.

ellipse model. In the case of a rotated ellipsoidal, `Halo-FDCA` returns in output the central surface brightness I_0, the values of the two semi-axes (r_x and r_y), the coordinates

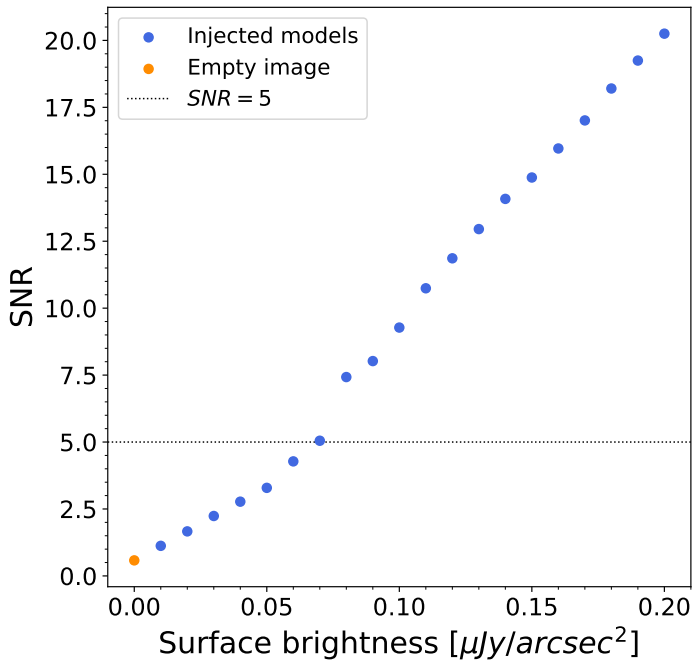

Figure 5.8: Plot showing the relation between the SNR and the surface brightness of the injected models for A2390. The orange dot is the SNR obtained from the empty image, the horizontal line is the threshold set at $SNR = 5$.

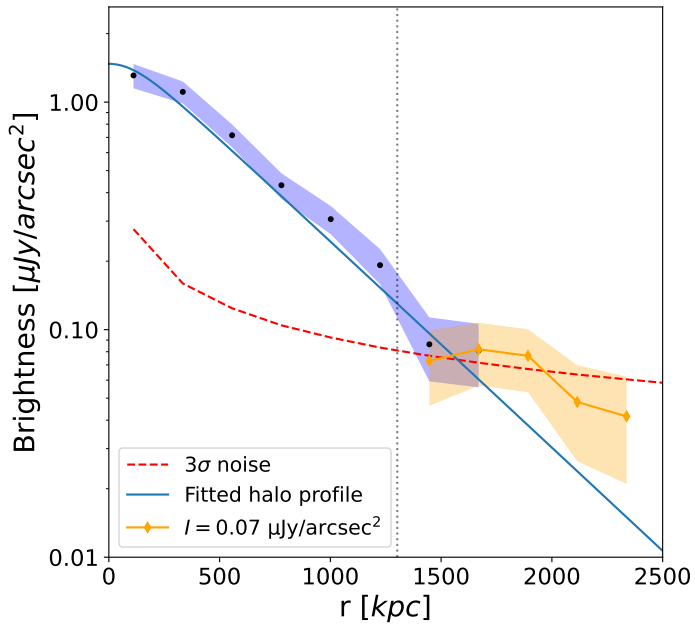

Figure 5.9: Profile of the halo in Abell 2390 alongside with the recovered profile of the mock megahalo. The halo points are shown in black with the errors showed as the shaded blue region. The orange points show the profile of the injected megahalo and the shaded orange region represents its errors.

of the center of the halo and the tilt angle of the model ϕ_e. The radius of the halo is computed from the semi-axes size, from the formula $r_e = \sqrt{r_x \cdot r_y}$ (Cuciti et al. 2021). From `Halo-FDCA` we obtained a central brightness of $I_0 = 1.37 \pm 0.06$ μJy/arcsec^2 while the semi-axes are $r_x = 640 \pm 29$ kpc and $r_y = 402 \pm 21$ kpc. The halo radius is therefore

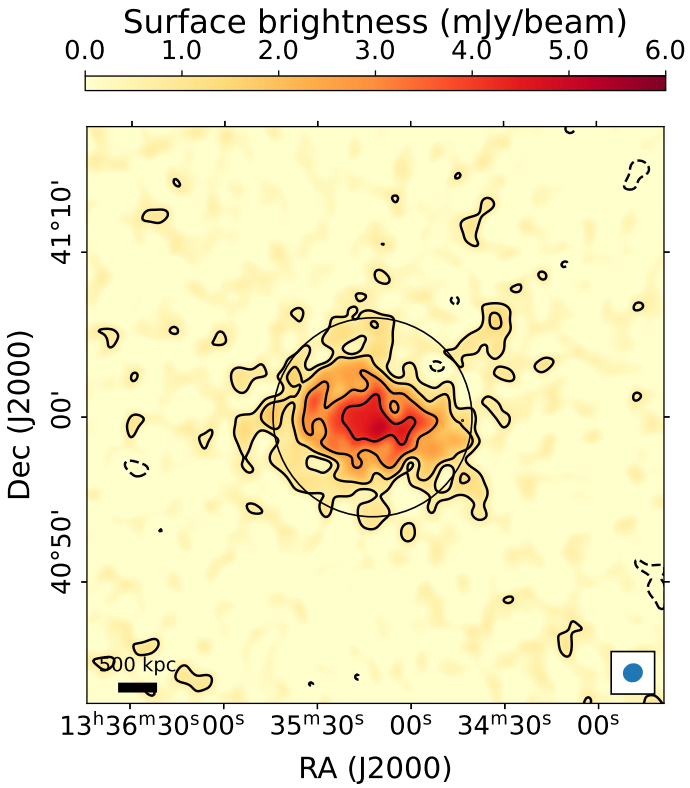

Figure 5.10: $60''$ resolution image showing the radio halo in Abell 1763. The contours are set at $[-3, 2, 4, 8, 12, 24] \cdot \sigma_{rms}$, where $\sigma_{rms} = 0.34$ mJy/beam and the black circle is r_{500}.

$r_e = 507 \pm 18$ kpc. The output plots of `Halo-FDCA` can be seen in Fig. 5.11, we can see in the right panel that withing the $2\sigma_{rms}$ contour there are positive residuals (up to ± 0.2 μJy/arcsec^2), which might be related to the image artifacts. From `Halo-FDCA`, we get a flux density of $S_{150\ \mathrm{MHz}} = 126 \pm 10$ mJy and a luminosity $P_{150\ \mathrm{MHz}} = (2.1 \pm 0.2) \cdot 10^{25}$ W/Hz, assuming $\alpha = 1.3$. Assuming the same spectral index, the emissivity at 1.4 GHz for this radio halo would be $J_{1.4\ \mathrm{GHz}} = (5.0 \pm 0.3) \cdot 10^{-43}$ erg/s/cm^3/Hz.

To investigate the presence of a megahalo, we produced two surface brightness profiles, one in the direction of the minor axis and one in the direction of the major axis, which can be seen in Fig. 5.12.
To produce these profiles we selected four elliptical sectors in four different directions and then averaged together the ones along the same axis. By analyzing the two profiles, we do not find any flattening of the surface brightness and therefore we exclude the detection of a megahalo at the current sensitivity. These regions are shown in Fig. 5.13.

We attempted to compute an upper limit to the megahalo emission, as done for the other clusters, but in this case we noticed that the large-scale pattern of the noise in the image is strongly dependent on the adopted uv-cut. Indeed, also the flux and radii of the radio halo is strongly affected by the selected uv-cut to produce the image. We produced three images, one without a uv-cut, one with the cut at 50λ and the last one at 80λ, and as we can see from Fig. 5.14 the noise pattern changes strongly, becoming more noticeable at lower uv-cuts. This can be noticed by comparing the image without the cut and the image with the cut at 80λ, shown in Fig. 5.14.

The pattern of noise in the images has the effect of increasing the SNR towards the cluster, but also in other empty regions of the field. Indeed, we notice a relatively

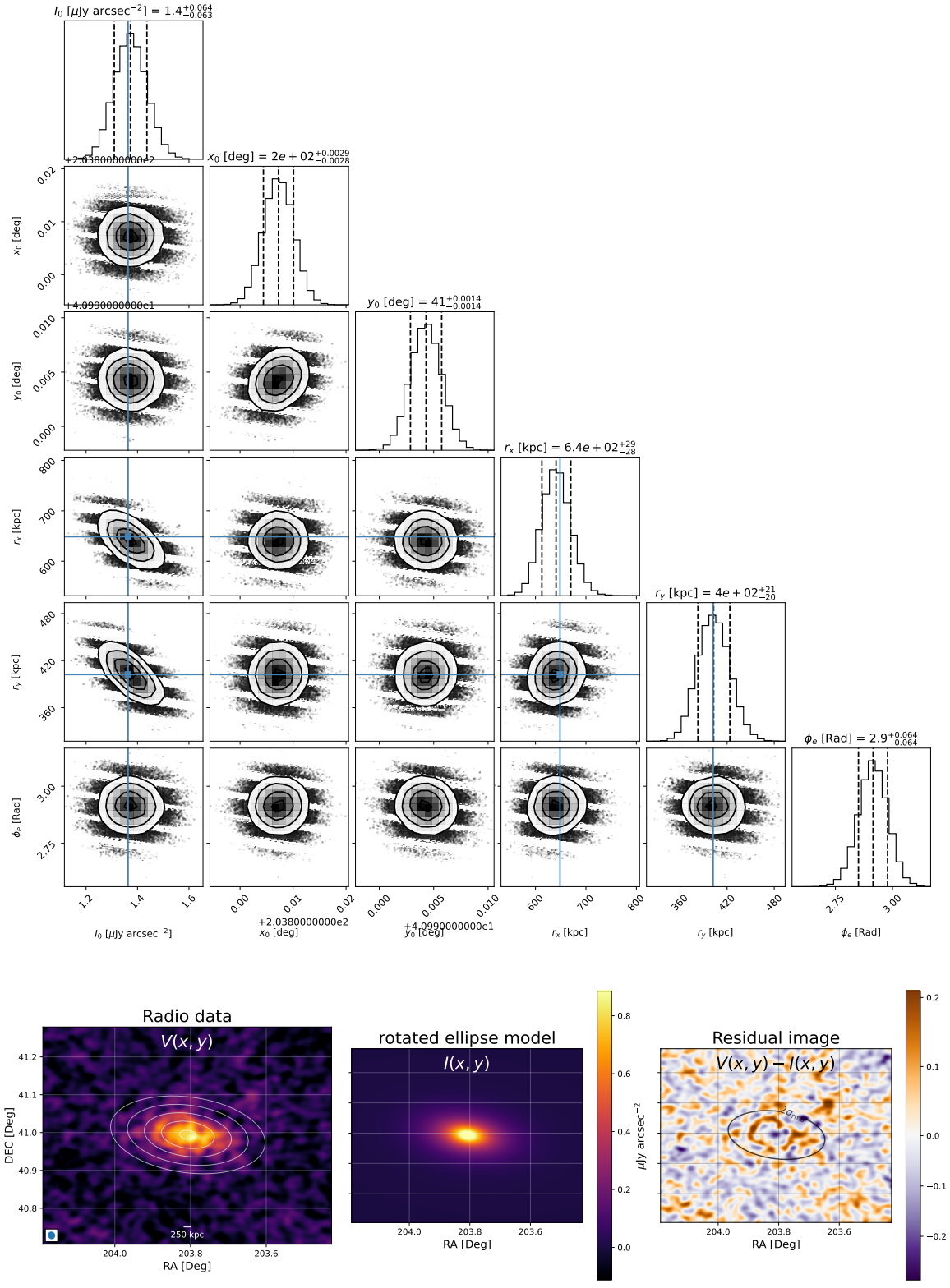

Figure 5.11: Results from Halo-FDCA for Abell 1763. *Top*: corner plot resulting from Halo-FDCA showing the distribution of the variables. *Bottom*: image used for the fit (left) with the contours of the best-fitted model (centre), on the right the residuals of the fit are shown. The scale of the residuals is the same of the data and model, which is μJy/arcsec^2.

high SNR around the cluster (≈ 3). Before claiming the presence of possible emission

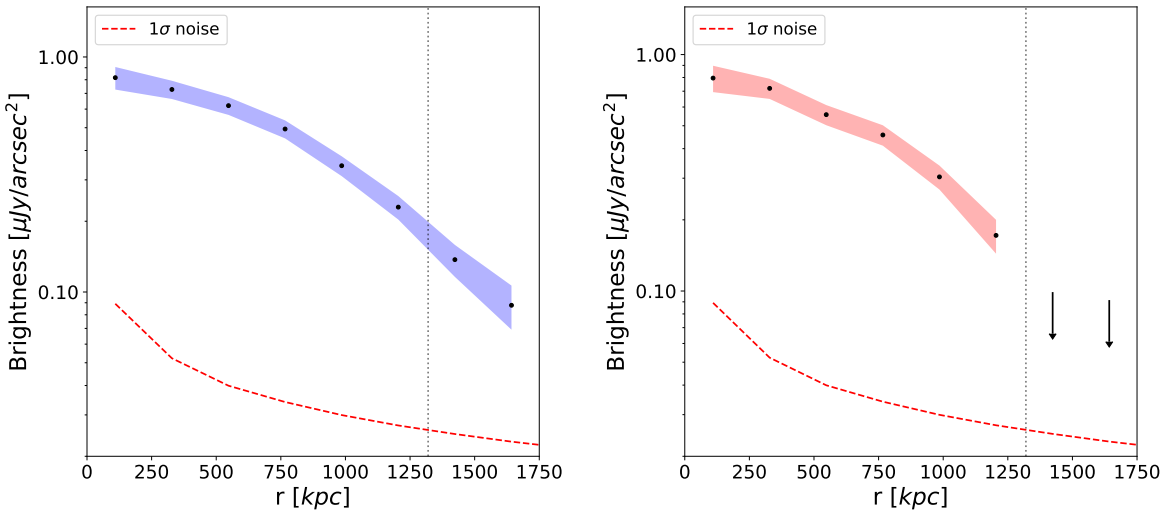

Figure 5.12: Surface brightness profiles of the radio halo in A1763 in the direction of the major axis (left) and minor axis (right)

around the cluster, we examined other regions of the image and found similar values for the SNR (≈ 3), which are listed in Table 5.1.

Region	SNR	Flux [mJy]	Noise [mJy]
1	3.4	16	5
2	3.1	14	5
3	3.3	15	5
4	3.3	15	5
5	3.8	18	5

Table 5.1: SNR computed in different regions of the image center on A1763 after the subtraction of all the sources. Region 1 is the original region drawn around the cluster.

The location of these regions is shown in Fig. 5.15 and, specifically, region 1 is the region drawn around A1763.
As the Galactic latitude of the source is ≈ 73.45, we find unlikely that this emission is Galactic, and conclude that this is probably due to the badly calibrated short baselines. Due to these issues related specifically to these data, we did not proceed with the injection of mock megahalos in the *uv*-data, because of the low reliability of the procedure with a non uniform noise pattern.

Abell 2261

We confirm also the presence of the radio halo in this cluster, that was already found by Savini et al. (2019). Our analysis from the 1-dimensional fit shows a central brightness of $I_0 = 1.30 \pm 0.13$ μJy/arcsec^2 and a radius $r_e = 428 \pm 28$ kpc. From these parameters, we estimate a flux density of $S_{144\ \mathrm{MHz}} = 92 \pm 15$ mJy[9], which is almost half of what was firstly estimated by Savini et al. (2019) but it is larger in size. This can be explained

[9] corresponding to $S_{150\ \mathrm{MHz}} = 86 \pm 14$ mJy.

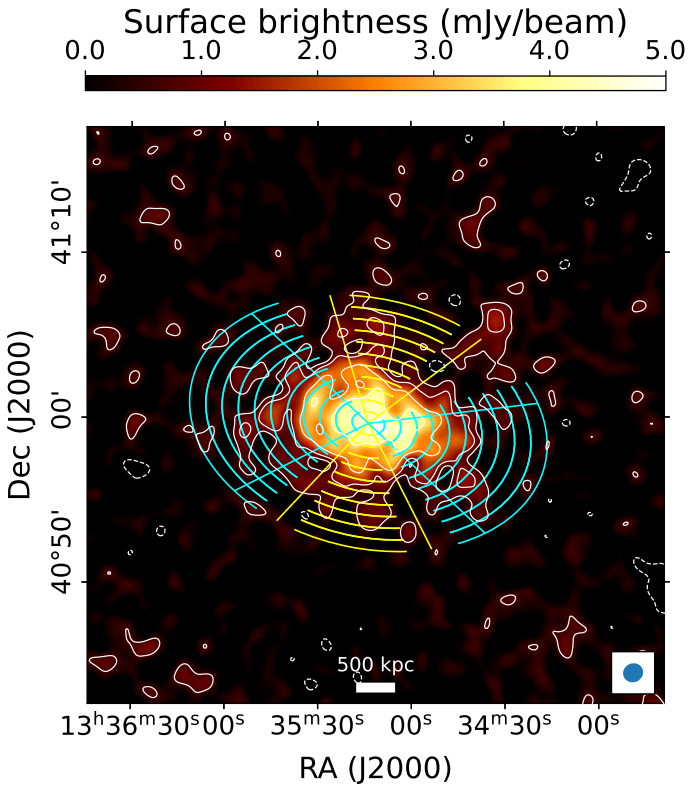

Figure 5.13: Low resolution (60″) image of A1763. The regions with the same colors are averaged together to produce the two surface brightness profiles.

by the fact that there is a strong radio galaxy which has not been completely removed by Savini et al. (2019) and that contaminated the radio halo emission, increasing its measured flux density. A similar issue happened in Botteon et al. (2022), in this case this radio source, that was not subtracted properly, has been masked in order to do the radio halo fit, but still led to a wrong estimate of the parameters, hence when we followed the subtraction procedure we estimated once again the various parameters, since in our case the radio galaxy was properly subtracted. The estimated power is therefore lower, with a value of $P_{144\ \mathrm{MHz}} = (1.6 \pm 0.3) \cdot 10^{25}$ W/Hz[10] against the $P = 2.6 \cdot 10^{25}$ W/Hz derived by Savini et al. (2019). This leads to an emissivity of $J_{1.4\ \mathrm{GHz}} = (6.0 \pm 0.7) \cdot 10^{-43}$ erg/s/cm^3/Hz.

From `Halo-FDCA` we got the central surface brightness $I_0 = 1.50 \pm 0.11$ μJy/arcsec^2 and the radius $r_e = 416 \pm 22$ kpc that are consistent with the 1D profile, the results of the analysis are shown in Fig. 5.17.

As there is no evidence for a megahalo, we proceeded with the derivation of an upper limit, which is reached for a modeled megahalo with a surface brightness of $I = 0.08$ μJy/arcsec^2, as we can see from Fig. 5.18. The injected flux density in the area between r_{500} and 2.5 Mpc is $S_{inj} = 90$ mJy and the corresponding radio power is $P_{inj} = 1.5 \cdot 10^{25}$ W/Hz. The recovered flux density instead is $S_{rec} = 28 \pm 6$ mJy, with an associated luminosity of $P_{rec} = 4.67 \pm 1.09 \cdot 10^{24}$ W/Hz.
In this case, the recovered flux density is less than 1/3 of the injected one and it is possibly related to the presence of strong negatives is the injection region, reducing the total measured flux density. Better image quality should allow for a better flux recovery,

[10] at 150 MHz we computed a power of $P_{150\ \mathrm{MHz}} = (1.4 \pm 0.2) \cdot 10^{25}$ W/Hz.

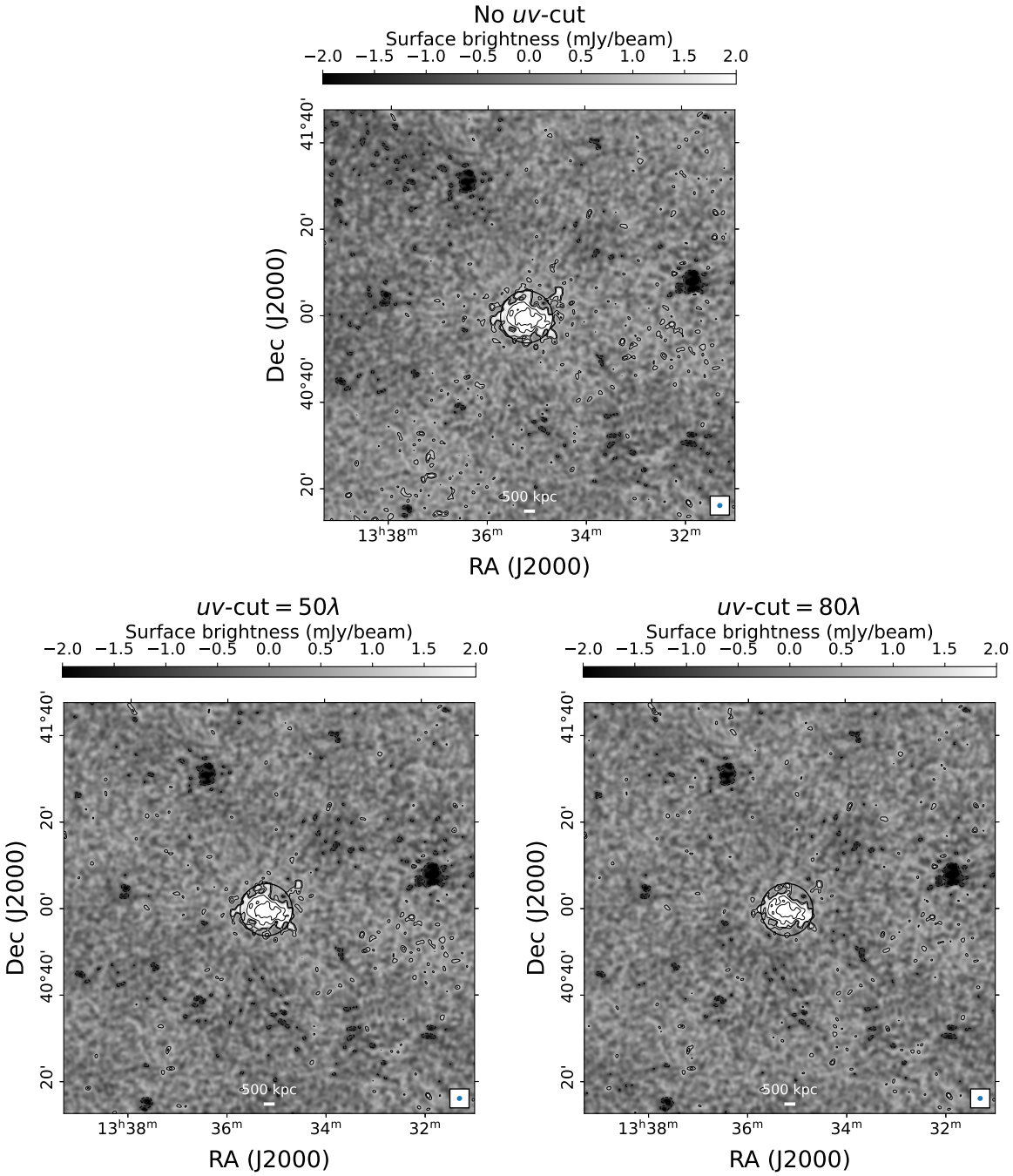

Figure 5.14: Low resolution (60″) images of A1763 at different *uv*-cuts, showing how the background noise pattern changes at different values. The black circle is r_{500} and the contours are set at $[-3, 2, 4, 8, 12, 24] \cdot \sigma_{rms}$, where $\sigma_{rms} = 0.3$ mJy/beam.

while deeper observations could decrease the detection limit in case of non-detection.

Considering the entire injection region, the injected flux density is $S_{inj} = 121$ mJy and the related luminosity is $P_{inj} = 2 \cdot 10^{25}$ W/Hz. The recovered flux density and power are $S_{rec} = 59 \pm 8$ mJy and $P_{rec} = (9.8 \pm 1.4) \cdot 10^{24}$ W/Hz respectively, leading to a fraction of recovered flux density of $\sim 50\%$.
We produced the surface brightness profile of the injected megahalo and plotted it alongside with the halo profile (see Fig. 5.19) and, as we can see also in this case, the surface brightness of the mock megahalo is around the 3σ level considering also the

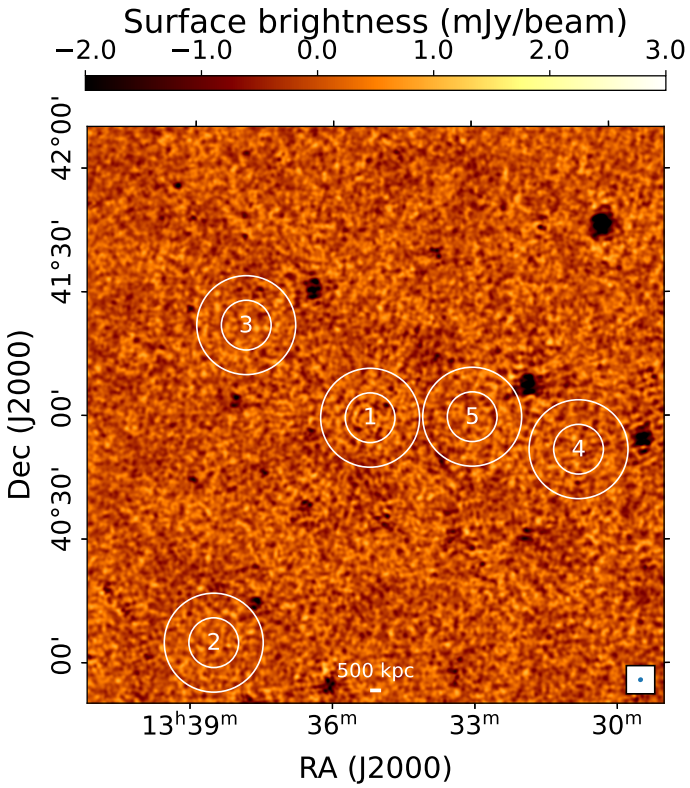

Figure 5.15: Resulting image after the subtraction of all the sources from Abell 1763, with a resolution of 60″. The five annuli are the regions in which we computed the signal-to-noise ratio in the image.

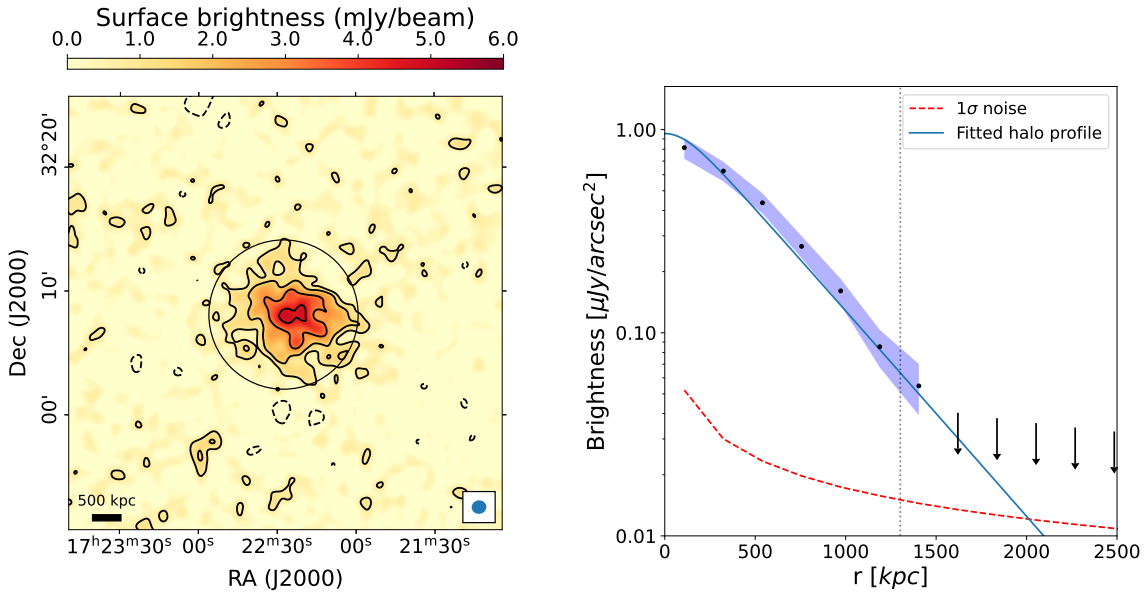

Figure 5.16: *Left*: low resolution image of Abell 2261 showing the radio halo. The black circle is r_{500}. The contours are set at levels $[-3, 2, 4, 8, 12, 24] \cdot \sigma_{rms}$, where $\sigma_{rms} = 0.38$ mJy/beam. *Right*: surface brightness profile of the radio halo. The solid line is the best fit of the emission, the vertical line is r_{500} and the red dashed line is 1σ detection limit of the surface brightness for each annulus.

errors.
The emissivity of the mock megahalo is very similar to the one of A2390, in fact it is $J_{1.4\ \mathrm{GHz}} = 2.7 \cdot 10^{-45}$ erg/s/cm^3/Hz, since the total flux density varies by a very small amount.

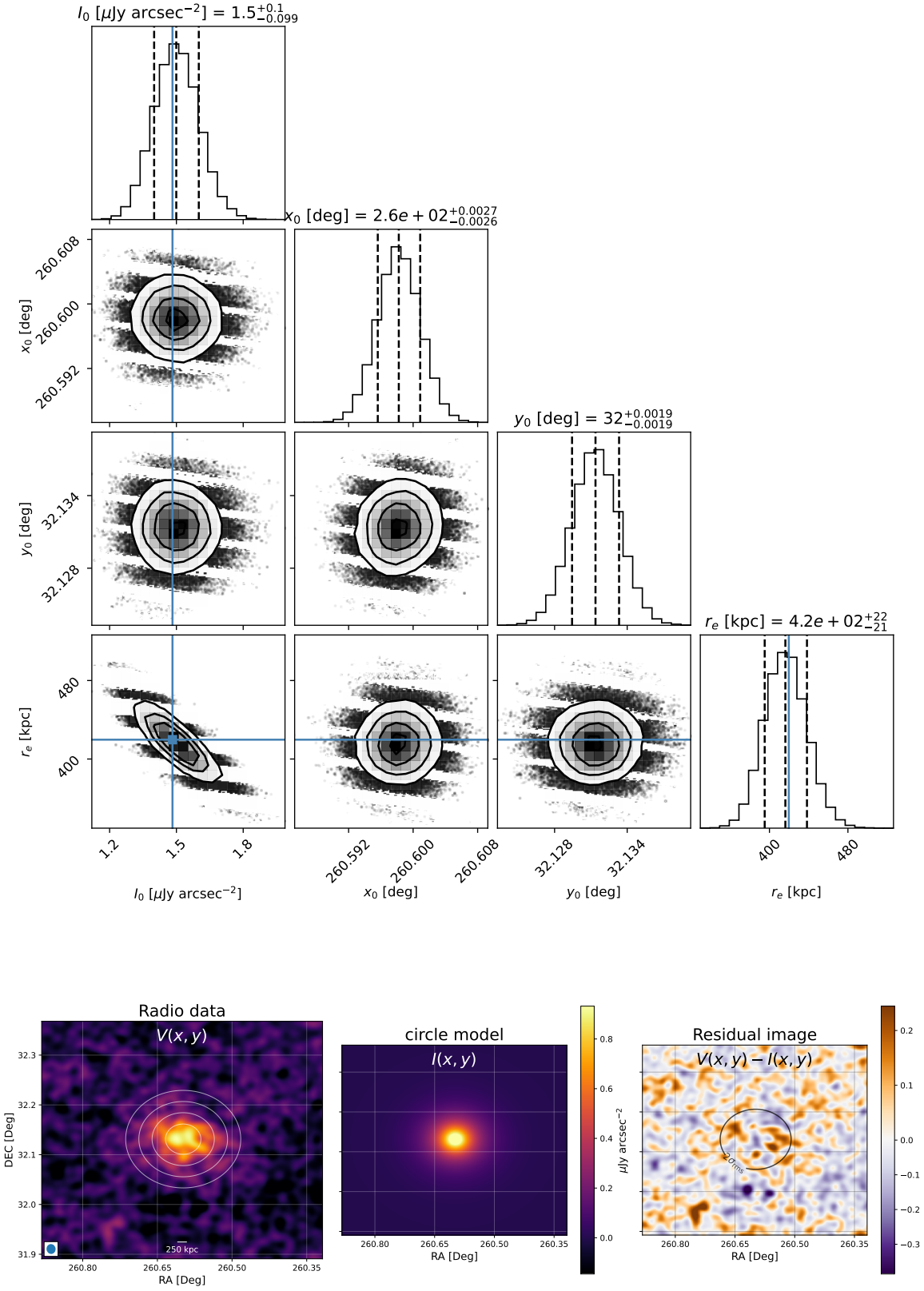

Figure 5.17: Results from Halo-FDCA for Abell 2261. *Top*: corner plot resulting from Halo-FDCA showing the distribution of the variables. *Bottom*: image used for the fit (left) with the contours of the best-fitted model (centre), on the right the residuals of the fit are shown. The scale of the residuals is the same of the data and model, which is μJy/arcsec^2.

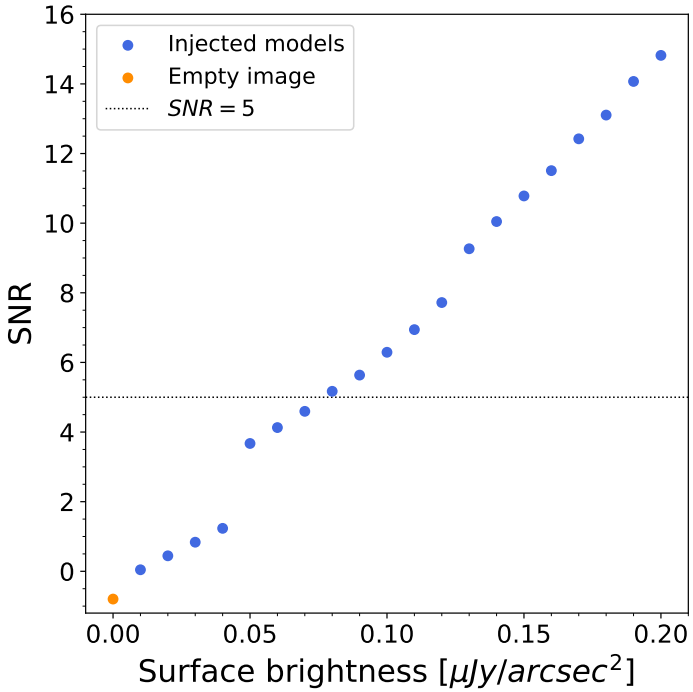

Figure 5.18: SNR vs model surface brightness for the cluster Abell 2261. The orange dot is the SNR computed in the empty image, the blue dots show the relation between the SNR and the injected models.

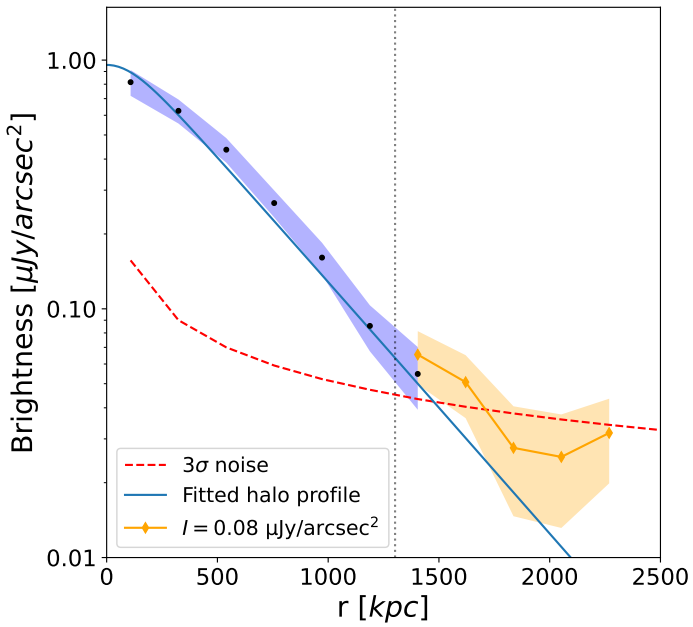

Figure 5.19: Abell 2261 halo profile alongside with the injected megahalo profile computed from the image. The black points are from the radio halo while the blue shaded region shows the associated errors. The orange points and region are the profile and associated errors computed from the image with the injected model.

Chapter 6

Discussion

In this chapter we are going to discuss in depth the results obtained from the analysis of our sources, specifically we are going to discuss the presence of the megahalo in Abell 2219 and comparing it with the simulations from Beduzzi et al. (2023, 2024). We will also discuss the results from the radio halo analysis, comparing them with the results from Cuciti et al. (2023). We will also show the first radio power-mass plot for megahalos and compare the emissivity of the megahalo in A2219 with the ones of the megahalos found by Cuciti et al. (2022).

6.1 The new megahalo in Abell 2219

As we have already seen, in the merging cluster Abell 2219 we discovered a new megahalo. We can see from the surface brightness profile (Fig. 5.5) that this is also the largest megahalo detected so far. In fact, the total scale of the diffuse radio emission, considering both the radio halo and the megahalo, reaches almost 2.5 Mpc, while the ones detected in Cuciti et al. (2022) reach at most ≈ 1.4 Mpc. In our case, the megahalo becomes visible at ≈ 1.4 Mpc, which is where we observe the flattening of the profile, and it extends for ≈ 1 Mpc. As briefly discussed in the previous Chapter, if we follow the assumption that megahalos cover also the central region of clusters, where radio halos are found, the actual extension of the emission is more than 2 Mpc and its emissivity is $J_{1.4\ \mathrm{GHz}} = (5.6 \pm 3.7) \cdot 10^{-45}$ erg/s/cm^3/Hz. To compute the emissivity we assumed a spectral index for the megahalo of $\alpha = 1.6$, which is in line with the only two indexes measured by Cuciti et al. (2022), although the authors assumed $\alpha = 1.3$ to be conservative. To be able to compare these results, we computed the emissivities of the four megahalos discovered assuming $\alpha = 1.6$, obtaining for all of them values $J_{1.4\ \mathrm{GHz}} \sim 10^{-45}$ erg/s/cm^3/Hz, which are consistent with our measurement. With these results, we can say that the average emissivity of megahalos is around two orders of magnitude lower than the one of radio halos.

Since it is difficult to constrain the real size of a megahalo, we assume that it occupies also the radio halo regions, that it has a spherical volume and that satisfies the assumption for the equipartition. With these assumption we computed a first equipartition field estimate through Eq. (2.5), resulting in $B_{eq} = 0.15 \pm 0.01$ μG, which is consistent with the average values of magnetic fields in clusters, despite the strong assumptions.

We can see from Fig. 5.5 that the megahalo is not symmetric around the radio halo and that the radio halo is not coincident with the cluster center. We therefore produced

a surface brightness profile dividing the cluster into two regions, centered on the radio halo which an offset of ≈ 180 kpc with respect to the cluster center. We chose the first region in the direction where the megahalo is more extended (South-East region) and the second one in the opposite direction. To produce these profiles and the one shown in Fig. 5.5 we excluded a region North-East of the cluster due to the residuals left by the subtraction of a strong source that would alter the resulting profiles in the most external parts.

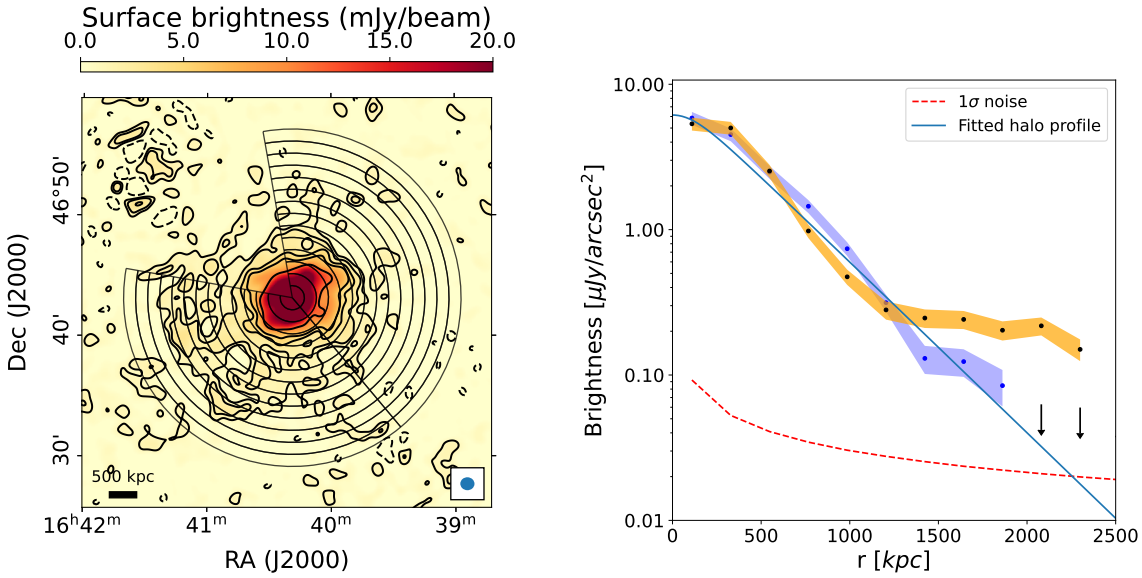

Figure 6.1: *Left*: low resolution image of Abell 2219 showing the diffuse radio emission and the semi-annuli used to measure the surface brightness. The contours are set at levels $[-3, 2, 4, 8, 12, 24] \cdot \sigma_{rms}$, where $\sigma_{rms} = 0.45$ mJy/beam. *Right*: surface brightness profile. The solid line is the best fit of the halo emission and the red dashed line is 1σ detection limit of the surface brightness for each annulus. The black points show the profile of the southern region with the errors shown by the orange shaded region, the blue points are taken from the northern region and the blue shaded region represents the associated errors.

From Fig. 6.1 we can clearly see that the megahalo extends mostly on the South-Eastern side of the cluster, and it shows an even greater extension compared to the one obtained by averaging over whole annuli, reaching ≈ 2.2 Mpc from the cluster centre. The profile of the northern part of the radio halo shows a small deviation from the exponential profile at around r_{500}, but we cannot say for sure that it is related to the megahalo emission.

As we can see, the megahalo covers a greater area in the region South-East to the cluster compared to the one in the North-Western part of the system. The flattening of the radial profile, visible near the cluster center, is likely due to the non-perfect subtraction of the strong AGN present at the center.

It is possible that this megahalo was not detected during the analysis of the LoTSS-DR2 clusters due to the bad subtraction of the central source, which lead to a poor dynamic range and quality of the image, decreasing the sensitivity to this large scale diffuse emission with very low surface brightness.

Considering the fact that this is a disturbed cluster that has a very complex merger history and that the region in which we observe the megahalo is roughly aligned with the merger axis (as seen from the X-ray images and the optical studies of the sub-

clusters), it is possible that this megahalo is originated from the main merger event as suggested by the simulation done and analyzed by Beduzzi et al. (2023, 2024), instead of it being related to the turbulence induced by the smooth accretion from the Cosmic Web (Cuciti et al. 2022). The asymmetric shape of this emission could be consistent with the results from Beduzzi et al. (2024), where it is said that the megahalo shape could be related to the projection due to the viewing angle, since in the simulation the megahalo has an ellipsoidal shape, related to the merger. Also the megahalos observed by Cuciti et al. (2022) show strong asymmetries, although they are present on both sides of the clusters (as shown by their profiles), this could still be related to the merger scenario. In fact, the smooth accretion scenario predicts that the gas accretion from the Cosmic Web induces turbulence (Vazza et al. 2011) that is strong enough to produce megahalos through Fermi II acceleration. In this case, the turbulence in the outskirts of cool-core and non cool-core clusters should be similar and we would observe almost symmetric megahalos in both types of clusters. Despite this, megahalos have been detected only in disturbed massive clusters so far, leaning to the hypothesis that a merger event is needed to form this kind of emission.

6.2 Radio power-mass relation

To better understand the origin of diffuse radio emission in clusters, a powerful tool is the radio power-mass diagram. In the case of radio halos, a clear relation between these two quantities exists, telling us that the most massive clusters should host the most luminous radio halos (Cuciti et al. 2023), as we can see also from Fig. 6.3. As a last step of this work, we built the same plot but for the known megahalos and and also including the upper limits determined in this study, we are aware that we have only a few points and are not enough to get a good statistics, but plotting them in the diagram to see where they are located with respect to each other, to start investigating the possible presence of a relation. In Fig. 6.2, we see two of these plots, one in which we considered the radio power of the megahalos in annular regions excluding the flux of radio halos up to $4r_e$ (on the left), and one in which the power has been estimated assuming that megahalos occupy also the same regions of radio halos (on the right), to keep consistency with the work of Cuciti et al. (2022).
Despite the very low statistics, due to the small number of known megahalos, we find intermediate values of the Pearson correlation coefficient, of 0.6 and 0.7 for the powers in the annulus and for the powers in the total volume respectively, although they do not have a high statistical significance since their p-values are ≈ 0.2 (these values are shown also in Table 6.1). In these plots, we show both the recovered and the injected powers, this is because a fraction of the flux is not recovered in the image after the injection and convolution. We consider both of them because the injected one is the true upper limit, but the recovered flux density is the one that must be used to do the comparison with the other megahalos. A detail we can see from Fig. 6.2 is that when we consider the total flux densities the fraction of recovered flux increases, giving us a smaller range for the upper limit true value. Differently from what happens for radio halos, our upper limits are not much lower than the values of observed megahalos, but have comparable values. This means that we cannot exclude the fact that megahalos might be present in every cluster and deeper observations will be needed to discover new megahalos or to put more stringent upper limits on their emission.
Keeping in mind that the statistics is very low, we tried to do a preliminary fit in both

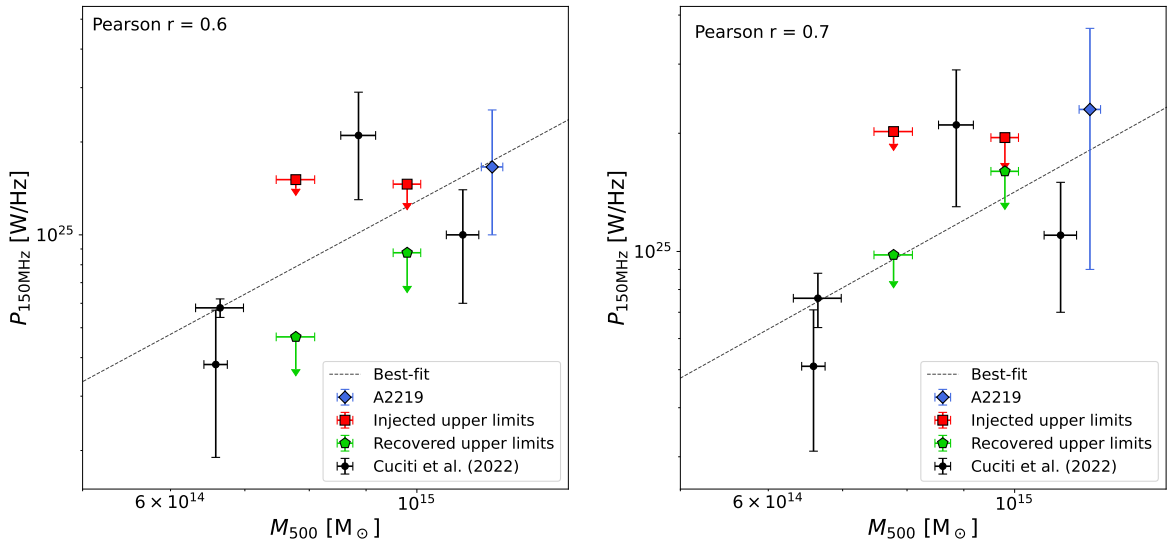

Figure 6.2: Radio power-mass diagram for the megahalos. The black points are the megahalos found in Cuciti et al. (2022). These plots show the powers computed in an annular region going from $4r_e$ of the radio halo up to the radius of the megahalo (left) and the powers computed assuming that the megahalo occupies also the same region of the radio halo (right). We reported also the Pearson r coefficient in both cases.

cases shown in Fig. 6.2.
We assumed a relation similar to the one described in Cuciti et al. (2023), defined as:

$$\log\left(\frac{P_{150\mathrm{MHz}}}{10^{24.5}\ \mathrm{W/Hz}}\right) = B\log\left(\frac{M_{500}}{10^{14.9}\ \mathrm{M}_\odot}\right) + A \tag{6.1}$$

In the case of the luminosities computed in an annular region in the cluster this results in $B = 1.94$ and $A = 0.41$, in the second case, instead, it results in $B = 1.57$ and $A = 0.49$, these parameters are reported also in Table 6.1. For the first case, we find a *Pearson* r coefficient of $r = 0.6$ and a p-value $p = 0.28$, while for the entire regions we got $r = 0.7$ and $p = 0.19$, confirming the fact that our statistics is still too low.

Region	A	B	Pearson r	p-value
Annular	0.41	1.94	0.6	0.28
Total	0.49	1.57	0.7	0.19

Table 6.1: Best-fit parameters assuming a linear relation between the radio power and the cluster mass for megahalos.

6.2.1 Upper limits

Among the three clusters showing no megahalo emission, two of them (Abell 2390 and Abell 1763) show hints of the presence of diffuse radio emission outside of r_{500} which could be related and connected to the cluster itself.
Abell 2390, especially, shows hints of this emission extending much farther out r_{500}, even though there is no detection of a megahalo. This emission decreases with a uv-cut of 150λ (correspondent to scales of ~ 5 Mpc at the source redshift), hinting

Object	$S_{150\ MHz}$ [mJy]	$P_{150\ MHz}$ [$\times 10^{24}$ W/Hz]	R [kpc]	$J_{1.4\ GHz}$ [$\times 10^{-45}$ erg/s/cm^3/Hz]
Megahalos				
A2219	130 ± 82	23 ± 14	2098 ± 130	5.6 ± 3.7
ZwCl 0634.1+4750	82 ± 12	7.6 ± 1.2	1400 ± 130	6.3 ± 1.9
A665	207 ± 74	21 ± 8	1417 ± 70	17 ± 7
A697	39 ± 19	11 ± 4	1432 ± 50	8.8 ± 4.4
A2218	57 ± 23	5.1 ± 1.9	1333 ± 102	4.8 ± 2.3
Upper limits				
A2390	106	19.5	2500	2.3
A2261	121	20.2	2500	2.7

Table 6.2: Main parameters of the current known megahalos and upper limits, assuming that they occupy the same regions as radio halos. For the upper limits we report only the injected values, which are the most conservative limits.

to the possible presence of large scale diffuse emission. Nevertheless, we notice that this could be also related to the worse image quality compared to the other images ($\sigma_{rms} \approx 0.7$ mJy/beam against $\sigma_{rms} \approx 0.3$ mJy/beam) or to the Galactic emission, since this cluster is closer to the Galactic plane (with a latitude of -27.82) with respect to the other three clusters we studied.

The case of Abell 1763 is also peculiar, because we can see some "plumes" of extended emission slightly crossing r_{500}. To investigate this emission, we produced two different surface brightness profiles, one along the major axis of the ellipse and the other one along the minor axis. The profiles do not show any presence of a flattening at great distance from the center, excluding the detection of a megahalo at the current sensitivity.

Deeper radio observations are needed to either uncover the possible presence of megahalos that are hidden due to the current sensitivity. In addition, with the aid of optical and X-ray observations, we can investigate the presence of a possible relation between the presence of megahalos and the dynamical states of galaxy clusters.

The main results on megahalos from this study are reported in Table 6.2 alongside with the results from Cuciti et al. (2022). The differences between the emissivity and the radio power in the four megahalos studied by Cuciti et al. (2022) are related to the different assumption when we re-analyzed the data. Despite this, they are consistent within the error and have very similar values, except for the emissivity, which has been computed again assuming a spectral index of $\alpha = 1.6$.

6.3 Giant radio halos in our sample

As we already and briefly saw in the previous Chapter, we observed giant halos in every cluster we analyzed; where the radio halos in Abell 2261 (Sommer et al. 2017, Savini et al. 2019) and Abell 2219 were already reported in literature, the presence of the radio halo in Abell 2390 (Sommer et al. 2017, Savini et al. 2019) was debated and we discovered a new radio halo in Abell 1763. We note that two of these clusters,

namely Abell 2390 and Abell 2261, are cool-core clusters, as we can see from our c-w plot in the left panel of Fig. 6.4. The presence of radio halos in cool-core clusters is an interesting finding, since most giant halos and classical halos are found in disturbed clusters. In Table 6.3 we have listed the properties of the radio halos, such as central brightness, effective radius, emissivity at 1.4 GHz, flux density and power at 150 MHz. As expected, the properties of these radio halos are consistent with the ones found in literature.
To check if these are actually giant halos and the extension is not actually modified by the low resolution, we also produced images with a Gaussian taper set to `taper=100kpc` ($\sim 27''$) and then we visually inspected the images and produced the surface brightness profiles which we compared with the best-fit profiles that we found previously. We noticed that, during this visual inspection, it was slightly harder to identify the entire halo emission, likely because of the lower sensitivity to the diffuse emission of the higher resolution images. In fact, when we produced the brightness profiles, the extension of the emission was comparable with the one measured from the low resolution images, with variations in the range of $100 - 200$ kpc that could be related to the lower sensitivity. Even with the difference of a couple hundreds of kiloparsecs in size, the halos would still be classified as giant radio halos, since they would span around 2 Mpc.

Object	I_0 [μJy/arcsec^2]	r_e [kpc]	$S_{150\ MHz}$ [mJy]	$P_{150\ MHz}$ [$\times 10^{25}$ W/Hz]	$J_{1.4\ GHz}$ [$\times 10^{-43}$ erg/s/cm^3/Hz]
Abell 2219	8.76 ± 1.60	369 ± 29	427 ± 103	7.0 ± 1.7	44 ± 0.09
Abell 2390	1.95 ± 0.22	478 ± 38	152 ± 30	2.8 ± 0.6	8.2 ± 1.1
Abell 1763	1.37 ± 0.06	507 ± 18	126 ± 10	2.1 ± 0.2	5.0 ± 0.3
Abell 2261	1.30 ± 0.13	428 ± 28	86 ± 14	1.4 ± 0.2	5.6 ± 0.7

Table 6.3: Main properties of the four giant radio halos analyzed in this work.

6.3.1 Power-mass relation of the radio halos

The spectral indexes are available in literature only for Abell 2219, Abell 2390, and Abell 2261. For A2219, the only spectral index analysis has been done by Orrù et al. 2007 and it resulted in the spectral index ranging between $\alpha = 1.0$ and $\alpha = 1.5$ (between 325 MHz and 1.4 GHz), hence we adopted an average spectral index of $\alpha = 1.3$ (see Feretti et al. 2012). The spectral index of A2390 has been estimated by Sommer et al. (2017) through wide band observations of the JVLA, finding a value of $\alpha = 1.6$, making it an ultra steep spectrum radio halo. For A2261, we assumed two different spectral indexes in order to compare our results with the ones from Savini et al. (2019), where they estimated the spectral index between 144 MHz and 240 MHz (Sommer et al. 2017). This resulted in a spectral index of $\alpha = 1.7 \pm 0.3$. By comparing our radio halo morphology with the one observed by Savini et al. (2019), we found that they have great differences and that ours is similar to the one observed with the GMRT by Sommer et al. (2017), as we already explained in Chapter 5. Due to this, we computed the spectral index comparing our flux density at 144 MHz and the ones computed by Sommer et al. (2017) at 240 MHz and 610 MHz, finding a range for the spectral index between $\alpha = 0.3$ and $\alpha = 1.8$. Due to this large uncertainty, that could be either to

our subtraction or to the analysis of GMRT data by Sommer et al. (2017), we decided to assume $\alpha = 1.3$ for our powers and emissivities.
The last cluster we analysed is A1763. We report the first detection of a radio halo in this cluster, therefore there are no spectral studies and we had to assume the spectral index as $\alpha = 1.3$ from Feretti et al. (2012).

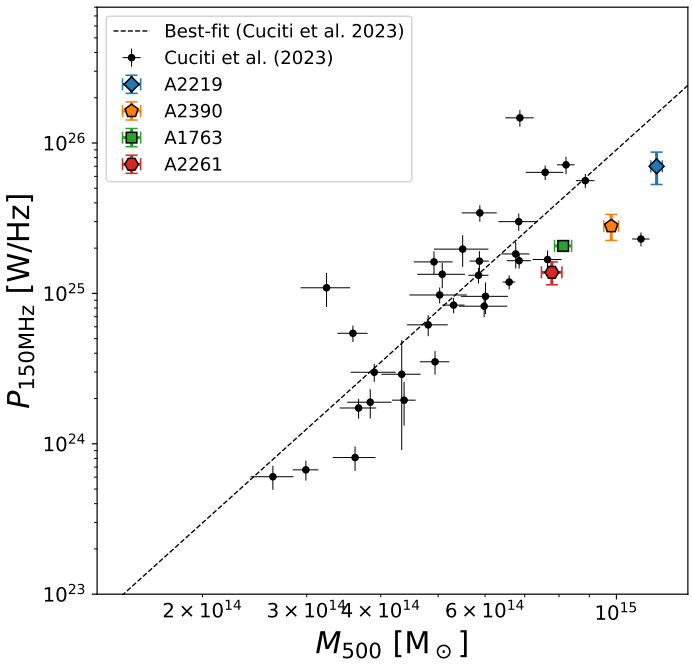

Figure 6.3: Radio power-cluster mass plot comparing the luminosity of the radio halos studied in this work compared to the results from Cuciti et al. (2023).

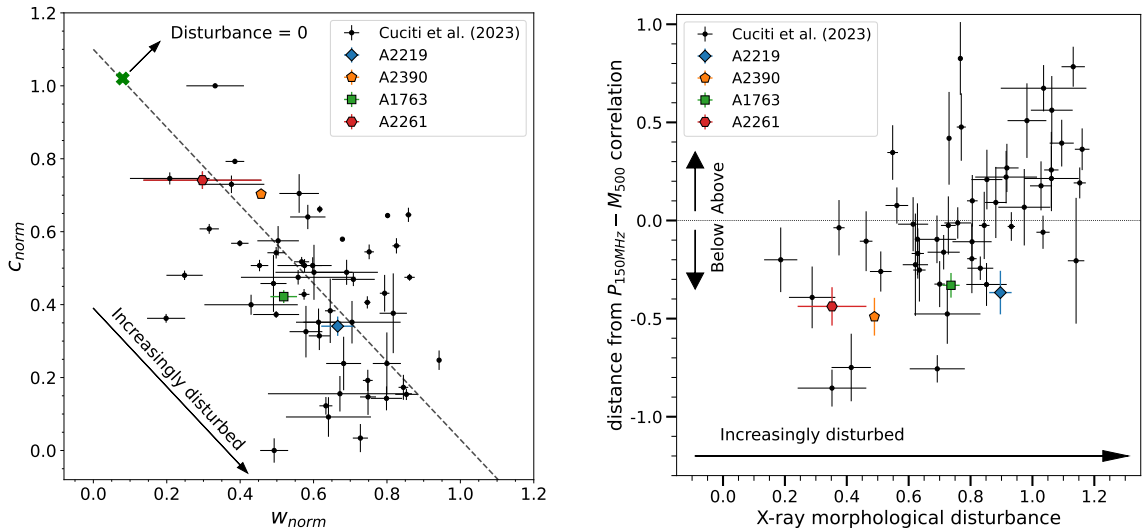

Figure 6.4: *Left*: *c*-*w* plot highlighting the targets of this study. The black points are the clusters hosting radio halos reported in Cuciti et al. (2023). The dotted line is the best-fit computed in the same study. *Right*: distance of radio halos from the radio power-mass relation in function of the X-ray morphological disturbance.

In Fig. 6.3, we show our four clusters alongside the radio halo sample of the LoTSS-DR2 analysed in Cuciti et al. (2023), while the dotted line is the best-fit found in the

same study. Alongside with the c-w plot on the left in Fig. 6.4, we show the scatter of the radio power-mass correlation against the X-ray morphological disturbance (described in Section 1.3.1), using also the data analysed by Cuciti et al. (2023). The disturbance is a parameter derived from the combination of the concentration and centroid shift. The disturbance of a cluster can be imagined as the projection of the points in the left panel of Fig. 6.4 onto the best-fit line and the disturbance increase for greater w and lower c. This plot shows a clear correlation between the power of radio halos and the morphological disturbance of the clusters, showing that clusters that have over-luminous halos are also the most disturbed ones. Our results are consistent with what was found by Cuciti et al. (2023), except for A2219, which is below the expected relation, although this could be related to the complex subtraction that we did to uncover the diffuse emission, which could affect its flux reducing it.

Chapter 7

Conclusions and future prospects

Megahalos are a type of large scale diffuse radio emission present in galaxy clusters, recently discovered by Cuciti et al. (2022) through LOFAR observations. Their extension can reach and surpass r_{500}, making them the best way to probe magnetic fields on large scales within clusters. In this work, we analyzed LOFAR 144 MHz data of four clusters (Abell 2219, Abell 2390, Abell 1763 and Abell 2261) to search for the possible presence of megahalos or put limits to their radio power. These are among the most massive PSZ2 clusters in the entire LoTSS-DR2 (Shimwell et al. 2022, Botteon et al. 2022). Considering the assumptions from Cuciti et al. (2022) on the surface brightness, which are the power-law relation with the cluster mass and the cosmological dimming, we can identify a region in which we expect to detect megahalos, as we can see from Fig. 3.1. The four clusters that we studied in this work are satisfying these conditions, making them the best candidates for the study. Although the images have an rms in line with the rest of the LoTSS-DR2 ($\sigma_{rms} \simeq 0.1$ mJy/beam), the quality of the images did not allow the authors to investigate the presence of a megahalo because of calibration and/or subtraction artifacts. Therefore, they were not analyzed in the survey.

To search for possible diffuse emission, we first had to make "ad-hoc" subtractions of the discrete sources present in the clusters and then produce low resolution 60″ images to study the properties of the diffuse emission. Following this approach, we detected radio halos in every cluster. Two of them were already known in the literature (A2219 and A2261), one was debated (A2390), and one is a new discovery of our work (A1763). We estimated the main properties of the radio halos, such as the central surface brightness, the effective radius, flux density, radio power, and emissivity (at 1.4 GHz) and compared them with the results from Cuciti et al. (2023). All the radio halos that have been detected can be classified as giant radio halos since their radii are all $\gtrsim 1$ Mpc.

The radio halos were fitted with a simple exponential profile and a comparison has been made with the results from `Halo-FDCA`, the flux density and emissivity have also been computed using the exponential profile assumption and using the relations defined in Murgia et al. (2009), finding consistent values in every case. In order to compare our radio powers with the ones measured in the LoTSS (Botteon et al. 2022), we applied the k-correction and computed them at 150 MHz. We computed the flux density and power of found and injected megahalos at 150 MHz and the emissivity at 1.4 GHz to compare them with the average values of radio halos.

To determine the upper limits on the megahalo emission, we set the threshold of

the flux density to $SNR = 5$ in an annular region around the radio halo, by injecting megahalos with flat surface brightness distributions in the *uv*-data.

Abell 2219: In A2219 we fitted the radio halo using an exponential profile with a central surface brightness $I_0 = 7.6 \pm 1.6$ μJy/arcsec^2 and an effective radius of $r_e = 369 \pm 29$ kpc. Through these parameters, we computed a flux density of $S_{150\ \mathrm{MHz}} = 427 \pm 103$ mJy, with the assumption of the average spectral index of radio halos being $\alpha = 1.3$ (Feretti et al. 2012) the radio power is $P_{150\ \mathrm{MHz}} = (7.0 \pm 1.7) \cdot 10^{25}$ W/Hz. We also estimated the average volume emissivity at 1.4 GHz, which resulted in $J_{1.4\ \mathrm{GHz}} = (4.4 \pm 0.9) \cdot 10^{-42}$ erg/s/cm^3/Hz.
In this cluster, we discovered a new megahalo, which is also the largest one detected so far, with a radius $R_{MH} = 2089 \pm 130$ kpc. The measured flux density is $S_{150\ \mathrm{MHz}} = 130 \pm 82$ mJy, which corresponds to a radio power $P_{150\ \mathrm{MHz}} = (2.3 \pm 1.4) \cdot 10^{25}$ W/Hz, under the assumption that megahalos cover also the regions in which radio halos are found. With this assumption, we can estimate the emissivity at 1.4 GHz as if the emission comes from a sphere with radius R_{MH}, assuming also a spectral index $\alpha = 1.6$, as found by Cuciti et al. (2022). For this megahalo, this results in $J_{1.4\ \mathrm{GHz}} = (5.6 \pm 3.7) \cdot 10^{-45}$ erg/s/cm^3/Hz.

Abell 2390: In A2390 we confirm the presence of the radio halo detected by Sommer et al. (2017) and fitted it with an exponential profile which has a peak brightness of $I_0 = 1.95 \pm 0.22$ and an effective radius $r_e = 478 \pm 38$ kpc. The flux density is $S_{150\ \mathrm{MHz}} = 152 \pm 30$ mJy, the radio power is $P_{150\ \mathrm{MHz}} = (2.8 \pm 0.6) \cdot 10^{25}$ W/Hz and the emissivity $J_{1.4\ \mathrm{GHz}} = (8.2 \pm 1.1) \cdot 10^{-43}$ erg/s/cm^3/Hz, all computed assuming a spectral index $\alpha = 1.6$ (Sommer et al. 2017). All these values are consistent with what we expect from radio halos from the power-mass correlation. There is no detection of a megahalo in this cluster, therefore to determine the upper limit to the radio emission we injected a mock megahalo with radius ~ 2.5 Mpc centered on the cluster. With our procedure, we determined the upper limit corresponding to a megahalo with a flat surface brightness of of $I = 0.07$ μJy/arcsec^2, which corresponds to an injected flux density of $S_{inj} = 106$ mJy and a recovered flux density $S_{rec} = 87 \pm 15$ mJy, in the injection region. The injected radio power is $P_{inj} = 2 \cdot 10^{25}$ W/Hz and the recovered one is $P_{rec} = (1.6 \pm 0.3) \cdot 10^{25}$ W/Hz, leading to a recovered flux fraction of ≈ 0.8. The emissivity has been computed through the injected flux density, resulting in $J_{1.4\ \mathrm{GHz}} = 2.3 \cdot 10^{-45}$ erg/s/cm^3/Hz.

Abell 1763: The newly discovered radio halo in A1763 has been fitted with a rotated ellipsoidal model through `Halo-FDCA` software, which returned a central brightness of $I_0 = 1.37 \pm 0.06$ μJy/arcsec^2 and the equivalent radius $r = 507 \pm 18$ kpc. The flux density of the radio halo is $S_{150\ \mathrm{MHz}} = 126 \pm 10$ mJy. Assuming $\alpha = 1.3$ (due to the lack of detections at other frequencies) the radio luminosity results in $P_{150\ \mathrm{MHz}} = (2.1 \pm 0.2) \cdot 10^{25}$ W/Hz, while the emissivity is $J_{1.4\ \mathrm{GHz}} = (5.0 \pm 0.3) \cdot 10^{-43}$ erg/s/cm^3/Hz. Due to the RFI[11]/residual calibration errors on the short baselines, we could not derive an upper limit on the radio power of megahalo emission for this cluster, hence we stopped our analysis early. A better calibration of the short baselines would allow us to put upper limits on the emission also for this cluster.

[11] Radio Frequency Interference

Abell 2261: The radio halo in A2261 was already studied by Savini et al. (2019), retrieving a flux density of $S_{144\ \mathrm{MHz}} \sim 165$ mJy and a radio power $P_{144\ \mathrm{MHz}} \sim 2.6 \cdot 10^{25}$ W/Hz. They also compared their results with the ones from Sommer et al. (2017), deriving a spectral index $\alpha = 1.7 \pm 0.3$. We re-analyzed the cluster and the radio halo. The central brightness is $I_0 = 1.30 \pm 0.13$ μJy/arcsec^2 and the effective radius is $r_e = 428 \pm 28$ kpc, which leads to a general larger extension with respect to the one found by Savini et al. (2019) ($r \sim 600$ kpc). Considering also the differences in the morphology of the halo and between our results (and the one in Sommer et al. 2017) and the ones by Savini et al. (2019), we set $\alpha = 1.3$. We computed a flux density of $S_{150\ \mathrm{MHz}} = 86 \pm 14$ mJy, a luminosity $P_{150\ \mathrm{MHz}} = (1.4 \pm 0.2) \cdot 10^{25}$ W/Hz and an emissivity of $J_{1.4\ \mathrm{GHz}} = (5.6 \pm 0.7) \cdot 10^{-43}$ erg/s/cm^3/Hz. This shows that our flux density is lower than the one measured by Savini et al. (2019). From the injection of mock megahalos in the *uv*-data, we set the detection limit when the surface brightness is $I = 0.08$ μJy/arcsec^2. This corresponds to an injected flux density of $S_{inj} = 121$ mJy and a power $P_{inj} = 2.0 \cdot 10^{25}$ W/Hz. The recovered flux density and power are $S_{rec} = 59 \pm 8$ mJy and $P_{rec} = (9.8 \pm 1.4) \cdot 10^{25}$ respectively, with a recovered flux density fraction is ≈ 0.5.

Radio power-mass plot: At the end of our work, we plotted the radio powers of our megahalo and upper limits on the radio power-mass diagram alongside with the results from Cuciti et al. (2022), finding possible hints of a relation, although the statistics is still too low to confirm it and more detections are needed to improve it. An important thing to notice is that the upper limits have luminosities similar to the ones of detected megahalos, therefore we cannot say that the emission is present only in a specific population of clusters (e.g. disturbed clusters), differently than radio halos, where the upper limits have much lower powers compared to the observed ones. It is still early to say if megahalos can be found in every cluster or not and to understand their origin. Searching for megahalos in low mass clusters will give us a wider mass and power range over which we can derive better constraints on the expected power-mass relation (in case of detection of more megahalos). Deeper observations and higher sensitivities will play a key role in future studies and searches for megahalos.

By comparing our results with the predictions from the plot in Fig. 3.1, we find that, at this time, we cannot put a constraint on the possible $SB-M$ relation, since our only detection is above all the three proposed curves, especially considering that the two upper limits we derived have recovered powers comparable to the ones of observed megahalos. Observations of low mass clusters with the same sensitivity in the proposed redshift range (see Cuciti et al. 2022 and Fig. 3.1) will give us a better estimate of the proposed brightness-mass relation.

Our results and current knowledge on megahalos does not allow us to tell if they can be found in every cluster and consequently we do not yet understand if their origin is connected to mergers. Nevertheless, we have been able to observe megahalos only in clusters which are already hosting radio halos (and are disturbed clusters), moreover, all these megahalos show asymmetric shapes. This is consistent with what has been shown by Beduzzi et al. (2023, 2024), where the authors simulated the time evolution of a low mass cluster through various mergers, resulting in the formation of a radio halo and a megahalo. The properties of the simulated emission are consistent with what we have observed up to now despite the mass difference between observed and simulated clusters.

Future prospects: As we said in the previous paragraph, the same analysis done in our work can be carried out also for lower mass clusters in the redshift range indicated in Cuciti et al. (2022). In case of detection of megahalos in low mass clusters it will be possible to improve the constraints on the proposed power-mass and brightness-mass relations suggested so far.

With deeper observations and higher sensitivities, we expect to be able to detect more and fainter megahalos, allowing us to get better constraints on their properties, such as the magnetic field intensity in the megahalo regions, the relation between the presence of the emission and the dynamical state of clusters (with the help of optical and X-ray observations) and on their extension, since in every case we can see an almost sharp cut-off in the surface brightness profiles. In case of non-detection at higher sensitivities we will be able to put more stringent upper limits to megahalos luminosities.

To characterize the emission and understand its origin, observations at ultra-low frequencies (i.e. 50 MHz) will be needed, for example with LOFAR LBA, allowing us to probe the most luminous part of the spectrum and their maximum extension, also opening the possibilities to spectral studies. Up to now, in fact, only two megahalos have been also observed in the ultra-low band ($\approx$ 50 MHz) and it has been observed that their extension increases at lower frequencies.

Deep radio observations at higher frequencies are also important to probe the spectrum at intermediate frequencies and to search for possible substructures, currently the best interferometer for this is MeerKAT (see Jonas & MeerKAT Team 2016 for information about this telescope). This telescope has sensitivity and resolution high enough to detect megahalos in the range of $544 - 1987$ MHz and at GHz frequencies and to observe the possible presence substructures in the emission, alongside with the possibility to start investigating their polarization.
With the advent of the Square Kilometer Array (SKA) Low ($\nu = 50 - 350$ MHz), it will be possible to detect megahalos at frequencies of the order of a few MHz, with a sensitivity at least comparable to the one of LOFAR HBA, although with a lower resolution due to the lack of long baselines. Combining the observations of SKA-Low with the ones of SKA-Mid ($\nu = 350$ MHz $- 15$ GHz), will allow for wide band spectral studies of megahalos, aiming for observations between 50 MHz and 1 GHz.
The next LOFAR upgrade, LOFAR 2.0, will also allow for better observations, in terms of resolution and sensitivity in the LBA band, allowing simultaneous observations between LBA and HBA (and thus a better directional dependent calibration) and allowing observations and frequencies < 50 MHz. This update maximises the number of low band antennas that can be used at the same time, increasing the sensitivity of the instrument. This means that both SKA and LOFAR 2.0 will allow us to detect or put limits on megahalos in less massive clusters and with lower powers with respect to the ones that we already studied, and will also allow us to understand better the dynamics behind the origin of megahalos, such as if they can be found only in merging clusters or also in relaxed clusters, and if a merger event is always necessary for their formation.

Bibliography

[1] Abell, G. O. 1958, The Astrophysical Journal, Supplement, 3, 211, doi: 10.1086/190036

[2] Abell, G. O., Corwin, Harold G., J., & Olowin, R. P. 1989, The Astrophysical Journal, Supplement, 70, 1, doi: 10.1086/191333

[3] Ackermann, M., Ajello, M., Albert, A., et al. 2016, The Astrophysical Journal, 819, 149, doi: 10.3847/0004-637x/819/2/149

[4] Allen, S. W. 2000, Monthly Notices of the Royal Astronomical Society, 315, 269–295, doi: 10.1046/j.1365-8711.2000.03395.x

[5] Allen, S. W., Ettori, S., & Fabian, A. C. 2001, Monthly Notices of the Royal Astronomical Society, 324, 877, doi: 10.1046/j.1365-8711.2001.04318.x

[6] Allen, S. W., & Fabian, A. C. 1998, Monthly Notices of the Royal Astronomical Society, 297, L57–L62, doi: 10.1046/j.1365-8711.1998.01737.x

[7] Allen, S. W., Rapetti, D. A., Schmidt, R. W., et al. 2008, Monthly Notices of the Royal Astronomical Society, 383, 879, doi: 10.1111/j.1365-2966.2007.12610.x

[8] Arnaud, M., Pointecouteau, E., & Pratt, G. W. 2007, Astronomy & Astrophysics, 474, L37–L40, doi: 10.1051/0004-6361:20078541

[9] Arnaud, M., Pratt, G. W., Piffaretti, R., et al. 2010, Astronomy and Astrophysics, 517, A92, doi: 10.1051/0004-6361/200913416

[10] Babyk, I. V., & McNamara, B. R. 2023, The Astrophysical Journal, 946, 54, doi: 10.3847/1538-4357/acbf4b

[11] Bacchi, M., Feretti, L., Giovannini, G., & Govoni, F. 2003, Astronomy & Astrophysics, 400, 465–476, doi: 10.1051/0004-6361:20030044

[12] Bagchi, J., Enßlin, T. A., Miniati, F., et al. 2002, New Astronomy, 7, 249–277, doi: 10.1016/s1384-1076(02)00137-9

[13] Bahcall, N. A. 1977, Annual Review of Astronomy and Astrophysics, 15, 505, doi: 10.1146/annurev.aa.15.090177.002445

[14] Bartelmann, M., Meneghetti, M., Perrotta, F., Baccigalupi, C., & Moscardini, L. 2003, Astronomy & Astrophysics, 409, 449–457, doi: 10.1051/0004-6361:20031158

[15] Basu, K. 2012, Monthly Notices of the Royal Astronomical Society: Letters, 421, L112–L116, doi: 10.1111/j.1745-3933.2012.01217.x

[16] Bauer, F. E., Fabian, A. C., Sanders, J. S., Allen, S. W., & Johnstone, R. M. 2005, Monthly Notices of the Royal Astronomical Society, 359, 1481–1490, doi: 10.1111/j.1365-2966.2005.08999.x

[17] Bautz, L. P., & Morgan, W. W. 1970, The Astrophysical Journal, Letters, 162, L149, doi: 10.1086/180643

[18] Beduzzi, L., Vazza, F., Brunetti, G., et al. 2023, Exploring the origins of mega radio halos. https://arxiv.org/abs/2306.03764

[19] Beduzzi, L., Vazza, F., Cuciti, V., et al. 2024, Cosmological simulations of the generation of cluster-scale radio emission from turbulent re-acceleration. https://arxiv.org/abs/2406.09859

[20] Best, P. N., Von Der Linden, A., Kauffmann, G., Heckman, T. M., & Kaiser, C. R. 2007, Monthly Notices of the Royal Astronomical Society, 379, 894–908, doi: 10.1111/j.1365-2966.2007.11937.x

[21] Bezecourt, J., Hoekstra, H., Gray, M. E., et al. 2000, Strong and weak lensing analysis of cluster Abell 2219 based on optical and near infrared data. https://arxiv.org/abs/astro-ph/0001513

[22] Bildfell, C., Hoekstra, H., Babul, A., & Mahdavi, A. 2008, Monthly Notices of the Royal Astronomical Society, 389, 1637–1654, doi: 10.1111/j.1365-2966.2008.13699.x

[23] Birzan, L., Rafferty, D. A., McNamara, B. R., Wise, M. W., & Nulsen, P. E. J. 2004, The Astrophysical Journal, 607, 800–809, doi: 10.1086/383519

[24] Boehringer, H., Tanaka, Y., Mushotzky, R. F., Ikebe, Y., & Hattori, M. 1998, An ASCA-ROSAT Study of the Distant, Lensing Cluster A2390. https://arxiv.org/abs/astro-ph/9803325

[25] Bonafede, A., Feretti, L., Murgia, M., et al. 2010, Astronomy & Astrophysics, 513, A30, doi: 10.1051/0004-6361/200913696

[26] Bonafede, A., Vazza, F., Bruggen, M., et al. 2013, Monthly Notices of the Royal Astronomical Society, 433, 3208–3226, doi: 10.1093/mnras/stt960

[27] Bonafede, A., Brüggen, M., van Weeren, R., et al. 2012, Monthly Notices of the Royal Astronomical Society, 426, 40–56, doi: 10.1111/j.1365-2966.2012.21570.x

[28] Bonafede, A., Intema, H. T., Brüggen, M., et al. 2014, Monthly Notices of the Royal Astronomical Society: Letters, 444, L44–L48, doi: 10.1093/mnrasl/slu110

[29] Bonafede, A., Cassano, R., Brüggen, M., et al. 2017, Monthly Notices of the Royal Astronomical Society, 470, 3465–3475, doi: 10.1093/mnras/stx1475

[30] Boschin, W., Girardi, M., Barrena, R., et al. 2004, Astronomy & Astrophysics, 416, 839–851, doi: 10.1051/0004-6361:20034362

[31] Botteon, A., Brunetti, G., Ryu, D., & Roh, S. 2020, Astronomy & Astrophysics, 634, A64, doi: 10.1051/0004-6361/201936216

[32] Botteon, A., Gastaldello, F., & Brunetti, G. 2018, Monthly Notices of the Royal Astronomical Society, 476, 5591–5620, doi: 10.1093/mnras/sty598

[33] Botteon, A., van Weeren, R. J., Brunetti, G., et al. 2020, Monthly Notices of the Royal Astronomical Society: Letters, doi: 10.1093/mnrasl/slaa142

[34] —. 2022, Science Advances, 8, doi: 10.1126/sciadv.abq7623

[35] Botteon, A., Shimwell, T. W., Cassano, R., et al. 2022, Astronomy & Astrophysics, 660, A78, doi: 10.1051/0004-6361/202143020

[36] Boxelaar, J., van Weeren, R., & Botteon, A. 2021, Astronomy and Computing, 35, 100464, doi: 10.1016/j.ascom.2021.100464

[37] Brentjens, M. A., & de Bruyn, A. G. 2005, Astronomy & Astrophysics, 441, 1217–1228, doi: 10.1051/0004-6361:20052990

[38] Briel, U. G., Henry, J. P., Lumb, D. H., et al. 2001, Astronomy & Astrophysics, 365, L60–L66, doi: 10.1051/0004-6361:20000024

[39] Briggs, D. S. 1995, in American Astronomical Society Meeting Abstracts, Vol. 187, American Astronomical Society Meeting Abstracts, 112.02

[40] Brüggen, M., Bykov, A., Ryu, D., & Röttgering, H. 2012, Space Science Reviews, 166, 187, doi: 10.1007/s11214-011-9785-9

[41] Brunetti, G. 2003, in Astronomical Society of the Pacific Conference Series, Vol. 301, Matter and Energy in Clusters of Galaxies, ed. S. Bowyer & C.-Y. Hwang, 349, doi: 10.48550/arXiv.astro-ph/0208074

[42] Brunetti, G., & Jones, T. W. 2014, International Journal of Modern Physics D, 23, 1430007, doi: 10.1142/S0218271814300079

[43] Brunetti, G., Setti, G., Feretti, L., & Giovannini, G. 2001, Monthly Notices of the Royal Astronomical Society, 320, 365–378, doi: 10.1046/j.1365-8711.2001.03978.x

[44] Brunetti, G., & Vazza, F. 2020, Physical Review Letters, 124, doi: 10.1103/physrevlett.124.051101

[45] Brunetti, G., Giacintucci, S., Cassano, R., et al. 2008, Nature, 455, 944–947, doi: 10.1038/nature07379

[46] Bruno, L., Brunetti, G., Botteon, A., et al. 2023, Astronomy & Astrophysics, 672, A41, doi: 10.1051/0004-6361/202244552

[47] Buote, D. A., & Tsai, J. C. 1996, The Astrophysical Journal, 458, 27, doi: 10.1086/176790

[48] Böhringer, H., Chon, G., & Kronberg, P. P. 2016, Astronomy & Astrophysics, 596, A22, doi: 10.1051/0004-6361/201628873

[49] Böhringer, H., Pratt, G. W., Arnaud, M., et al. 2010, Astronomy & Astrophysics, 514, A32, doi: 10.1051/0004-6361/200913911

[50] Campitiello, M. G., Ettori, S., Lovisari, L., et al. 2022, Astronomy & Astrophysics, 665, A117, doi: 10.1051/0004-6361/202243470

[51] Canning, R. E. A., Allen, S. W., Applegate, D. E., et al. 2017, Monthly Notices of the Royal Astronomical Society, 464, 2896, doi: 10.1093/mnras/stw2384

[52] Carlstrom, J. E., Holder, G. P., & Reese, E. D. 2002, Annual Review of Astronomy and Astrophysics, 40, 643–680, doi: 10.1146/annurev.astro.40.060401.093803

[53] Cassano, R., & Brunetti, G. 2005, Monthly Notices of the Royal Astronomical Society, 357, 1313–1329, doi: 10.1111/j.1365-2966.2005.08747.x

[54] Cassano, R., Brunetti, G., Röttgering, H. J. A., & Brüggen, M. 2010, Astronomy & Astrophysics, 509, A68, doi: 10.1051/0004-6361/200913063

[55] Cassano, R., Ettori, S., Giacintucci, S., et al. 2010, The Astrophysical Journal, 721, L82–L85, doi: 10.1088/2041-8205/721/2/l82

[56] Cavaliere, A., & Fusco-Femiano, R. 1978, Astronomy & Astrophysics, 70, 677

[57] Churazov, E., Sunyaev, R., Forman, W., & Bohringer, H. 2002, Monthly Notices of the Royal Astronomical Society, 332, 729–734, doi: 10.1046/j.1365-8711.2002.05332.x

[58] Cimatti, A., Fraternali, F., & Nipoti, C. 2019, Introduction to Galaxy Formation and Evolution: From Primordial Gas to Present-Day Galaxies

[59] Condon, J. J., Cotton, W. D., Greisen, E. W., et al. 1998, The Astronomical Journal, 115, 1693, doi: 10.1086/300337

[60] Condon, J. J., & Ransom, S. M. 2016, Essential Radio Astronomy

[61] Cornwell, T. J. 2008, IEEE Journal of Selected Topics in Signal Processing, 2, 793, doi: 10.1109/JSTSP.2008.2006388

[62] Cuciti, V., Cassano, R., Brunetti, G., et al. 2015, Astronomy & Astrophysics, 580, A97, doi: 10.1051/0004-6361/201526420

[63] —. 2021, Astronomy & Astrophysics, 647, A50, doi: 10.1051/0004-6361/202039206

[64] —. 2021, Astronomy & Astrophysics, 647, A51, doi: 10.1051/0004-6361/202039208

[65] Cuciti, V., de Gasperin, F., Brüggen, M., et al. 2022, Nature, 609, 911–914, doi: 10.1038/s41586-022-05149-3

[66] Cuciti, V., Cassano, R., Sereno, M., et al. 2023, The Planck clusters in the LOFAR sky V. LoTSS-DR2: Mass - radio halo power correlation at low frequency. https://arxiv.org/abs/2305.04564

[67] Dasadia, S., Sun, M., Sarazin, C., et al. 2016, The Astrophysical Journal, 820, L20, doi: 10.3847/2041-8205/820/1/l20

[68] de Gasperin, F., van Weeren, R. J., Brüggen, M., et al. 2014, Monthly Notices of the Royal Astronomical Society, 444, 3130–3138, doi: 10.1093/mnras/stu1658

[69] de Gasperin, F., Intema, H. T., Shimwell, T. W., et al. 2017, Science Advances, 3, doi: 10.1126/sciadv.1701634

[70] Dennison, B. 1980, The Astrophysical Journal, Letters, 239, L93, doi: 10.1086/183300

[71] Douglass, E. M., Blanton, E. L., Randall, S. W., et al. 2018, The Astrophysical Journal, 868, 121, doi: 10.3847/1538-4357/aae9e7

[72] Ebeling, H., Edge, A. C., Bohringer, H., et al. 1998, Monthly Notices of the Royal Astronomical Society, 301, 881–914, doi: 10.1046/j.1365-8711.1998.01949.x

[73] Edwards, L. O. V., Fadda, D., Biviano, A., & Marleau, F. R. 2010, The Astronomical Journal, 139, 434–446, doi: 10.1088/0004-6256/139/2/434

[74] Ensslin, T. A., & Bruggen, M. 2002, Monthly Notices of the Royal Astronomical Society, 331, 1011–1019, doi: 10.1046/j.1365-8711.2002.05261.x

[75] Enßlin, T. A., & Gopal-Krishna. 2001, Astronomy & Astrophysics, 366, 26, doi: 10.1051/0004-6361:20000198

[76] Fabian, A. C. 1994, Annual Review of Astronomy and Astrophysics, 32, 277, doi: 10.1146/annurev.aa.32.090194.001425

[77] Fadda, D., Biviano, A., Marleau, F. R., Storrie-Lombardi, L. J., & Durret, F. 2008, The Astrophysical Journal, Letters, 672, L9, doi: 10.1086/526457

[78] Feretti, L., Giovannini, G., Govoni, F., & Murgia, M. 2012, The Astronomy and Astrophysics Review, 20, doi: 10.1007/s00159-012-0054-z

[79] Finoguenov, A., Reiprich, T. H., & Böhringer, H. 2001, Astronomy & Astrophysics, 368, 749–759, doi: 10.1051/0004-6361:20010080

[80] Ghirardini, V., Ettori, S., Amodeo, S., Capasso, R., & Sereno, M. 2017, Astronomy & Astrophysics, 604, A100, doi: 10.1051/0004-6361/201630209

[81] Giacintucci, S., Markevitch, M., Cassano, R., et al. 2017, The Astrophysical Journal, 841, 71, doi: 10.3847/1538-4357/aa7069

[82] Giovannini, G., Bonafede, A., Feretti, L., et al. 2009, Astronomy & Astrophysics, 507, 1257–1270, doi: 10.1051/0004-6361/200912667

[83] Giovannini, G., Feretti, L., Venturi, T., Kim, K. T., & Kronberg, P. P. 1993, The Astrophysical Journal, 406, 399, doi: 10.1086/172451

[84] Giovannini, G., Tordi, M., & Feretti, L. 1999, New Astronomy, 4, 141–155, doi: 10.1016/s1384-1076(99)00018-4

[85] Gitti, M., Brunetti, G., & Setti, G. 2002, Astronomy & Astrophysics, 386, 456–463, doi: 10.1051/0004-6361:20020284

[86] Gitti, M., Tozzi, P., Brunetti, G., et al. 2015, in Advancing Astrophysics with the Square Kilometre Array (AASKA14), 76, doi: 10.22323/1.215.0076

[87] Golovich, N., Dawson, W. A., Wittman, D. M., et al. 2019, The Astrophysical Journal, Supplement, 240, 39, doi: 10.3847/1538-4365/aaf88b

[88] Govoni, F., & Feretti, L. 2004, International Journal of Modern Physics D, 13, 1549, doi: 10.1142/S0218271804005080

[89] Govoni, F., Dolag, K., Murgia, M., et al. 2010, Astronomy & Astrophysics, 522, A105, doi: 10.1051/0004-6361/200913665

[90] Govoni, F., Orrù, E., Bonafede, A., et al. 2019, Science, 364, 981–984, doi: 10.1126/science.aat7500

[91] Hales, S. E. G., Baldwin, J. E., & Warner, P. J. 1988, Monthly Notices of the Royal Astronomical Society, 234, 919, doi: 10.1093/mnras/234.4.919

[92] Hales, S. E. G., Masson, C. R., Warner, P. J., & Baldwin, J. E. 1990, Monthly Notices of the Royal Astronomical Society, 246, 256

[93] Hardcastle, M. J., Gürkan, G., van Weeren, R. J., et al. 2016, Monthly Notices of the Royal Astronomical Society, 462, 1910–1936, doi: 10.1093/mnras/stw1763

[94] Hitomi Collaboration, Aharonian, F., Akamatsu, H., et al. 2016, Nature, 535, 117, doi: 10.1038/nature18627

[95] Hoeft, M., Rajpurohit, K., Wittor, D., di Gennaro, G., & Domínguez-Fernández, P. 2022, On the Polarisation of Radio Relics. https://arxiv.org/abs/2201.03208

[96] Hoeft, M., Dumba, C., Drabent, A., et al. 2021, Astronomy & Astrophysics, 654, A68, doi: 10.1051/0004-6361/202039725

[97] Hudson, D. S., Mittal, R., Reiprich, T. H., et al. 2010, Astronomy and Astrophysics, 513, A37, doi: 10.1051/0004-6361/200912377

[98] Jonas, J., & MeerKAT Team. 2016, in MeerKAT Science: On the Pathway to the SKA, 1, doi: 10.22323/1.277.0001

[99] Kale, R., Venturi, T., Giacintucci, S., et al. 2013, Astronomy & Astrophysics, 557, A99, doi: 10.1051/0004-6361/201321515

[100] Kempner, J. C., Blanton, E. L., Clarke, T. E., et al. 2004, in The Riddle of Cooling Flows in Galaxies and Clusters of galaxies, ed. T. Reiprich, J. Kempner, & N. Soker, 335, doi: 10.48550/arXiv.astro-ph/0310263

[101] Kravtsov, A. V., & Borgani, S. 2012, Annual Review of Astronomy and Astrophysics, 50, 353–409, doi: 10.1146/annurev-astro-081811-125502

[102] Kuchar, P., & Enßlin, T. A. 2011, Astronomy & Astrophysics, 529, A13, doi: 10.1051/0004-6361/200913918

[103] Lin, Y., Mohr, J. J., & Stanford, S. A. 2003, The Astrophysical Journal, 591, 749–763, doi: 10.1086/375513

[104] Malkov, M. A., & Drury, L. O. 2001, Reports on Progress in Physics, 64, 429, doi: 10.1088/0034-4885/64/4/201

[105] Markevitch, M., Sarazin, C. L., & Vikhlinin, A. 1999, The Astrophysical Journal, 521, 526–530, doi: 10.1086/307598

[106] Mazzotta, P., & Giacintucci, S. 2008, The Astrophysical Journal, 675, L9–L12, doi: 10.1086/529433

[107] McNamara, B., & Nulsen, P. 2007, Annual Review of Astronomy and Astrophysics, 45, 117–175, doi: 10.1146/annurev.astro.45.051806.110625

[108] Million, E. T., & Allen, S. W. 2009, Monthly Notices of the Royal Astronomical Society, 399, 1307–1327, doi: 10.1111/j.1365-2966.2009.15359.x

[109] Mohr, J. J., Fabricant, D. G., & Geller, M. J. 1993, The Astrophysical Journal, 413, 492, doi: 10.1086/173019

[110] Molendi, S., & Pizzolato, F. 2001, The Astrophysical Journal, 560, 194–200, doi: 10.1086/322387

[111] Murgia, M., Govoni, F., Markevitch, M., et al. 2009, Astronomy & Astrophysics, 499, 679–695, doi: 10.1051/0004-6361/200911659

[112] Neronov, A. 2019, Journal of Physics: Conference Series, 1263, 012001, doi: 10.1088/1742-6596/1263/1/012001

[113] Offringa, A. R., McKinley, B., Hurley-Walker, et al. 2014, Monthly Notices of the Royal Astronomical Society, 444, 606, doi: 10.1093/mnras/stu1368

[114] Offringa, A. R., & Smirnov, O. 2017, Monthly Notices of the Royal Astronomical Society, 471, 301, doi: 10.1093/mnras/stx1547

[115] Orrù, E., Murgia, M., Feretti, L., et al. 2007, Astronomy & Astrophysics, 467, 943–954, doi: 10.1051/0004-6361:20066118

[116] Pasini, T., de Gasperin, F., Brüggen, M., et al. 2024, Ultra-low frequency LOFAR spectral indices of cluster radio halos. https://arxiv.org/abs/2406.12005

[117] Pearce, C. J. J., van Weeren, R. J., Andrade-Santos, F., et al. 2017, The Astrophysical Journal, 845, 81, doi: 10.3847/1538-4357/aa7e2f

[118] Peebles, P. J. E. 1980, The large-scale structure of the universe

[119] Peterson, J. R., Kahn, S. M., Paerels, F. B. S., et al. 2003, The Astrophysical Journal, 590, 207–224, doi: 10.1086/374830

[120] Petrosian, V. 2001, The Astrophysical Journal, 557, 560–572, doi: 10.1086/321557

[121] Pfrommer, C., & Enßlin, T. A. 2004, Astronomy & Astrophysics, 413, 17, doi: 10.1051/0004-6361:20031464

[122] Pfrommer, C., Pakmor, R., Schaal, K., Simpson, C. M., & Springel, V. 2016, Monthly Notices of the Royal Astronomical Society, 465, 4500–4529, doi: 10.1093/mnras/stw2941

[123] Pierre, M., Le Borgne, J. F., Soucail, G., & Kneib, J. P. 1996, Astronomy & Astrophysics, 311, 413, doi: 10.48550/arXiv.astro-ph/9510128

[124] Pignataro, G. V., Bonafede, A., Bernardi, G., et al. 2023, Probing diffuse radio emission in bridges between galaxy clusters with uGMRT. https://arxiv.org/abs/2311.09287

[125] —. 2024, Astronomy & Astrophysics, 685, L10, doi: 10.1051/0004-6361/202450051

[126] Pizzo, R. F. 2010, PhD thesis, University of Groningen, Netherlands

[127] Planck Collaboration, Ade, P. A. R., Aghanim, N., et al. 2011, Astronomy & Astrophysics, 536, A8, doi: 10.1051/0004-6361/201116459

[128] —. 2014, Astronomy & Astrophysics, 571, A20, doi: 10.1051/0004-6361/201321521

[129] —. 2016, Astronomy & Astrophysics, 594, A27, doi: 10.1051/0004-6361/201525823

[130] Poole, G. B., Fardal, M. A., Babul, A., et al. 2006, Monthly Notices of the Royal Astronomical Society, 373, 881–905, doi: 10.1111/j.1365-2966.2006.10916.x

[131] Pratt, G. W., Croston, J. H., Arnaud, M., & Böhringer, H. 2009, Astronomy & Astrophysics, 498, 361–378, doi: 10.1051/0004-6361/200810994

[132] Rajpurohit, K., Hoeft, M., van Weeren, R. J., et al. 2018, The Astrophysical Journal, 852, 65, doi: 10.3847/1538-4357/aa9f13

[133] Rajpurohit, K., Hoeft, M., Vazza, F., et al. 2020, Astronomy & Astrophysics, 636, A30, doi: 10.1051/0004-6361/201937139

[134] Ricker, P. M., & Sarazin, C. L. 2001, The Astrophysical Journal, 561, 621–644, doi: 10.1086/323365

[135] Rizza, E., Burns, J. O., Ledlow, M. J., et al. 1998, Monthly Notices of the Royal Astronomical Society, 301, 328, doi: 10.1046/j.1365-8711.1998.01972.x

[136] Roger, R. S., Costain, C. H., & Bridle, A. H. 1973, The Astronomical Journal, 78, 1030, doi: 10.1086/111506

[137] Ruszkowski, M., & Oh, S. P. 2010, The Astrophysical Journal, 713, 1332–1342, doi: 10.1088/0004-637x/713/2/1332

[138] Santos, J. S., Rosati, P., Tozzi, P., et al. 2008, Astronomy & Astrophysics, 483, 35–47, doi: 10.1051/0004-6361:20078815

[139] Sarazin, C. L. 1988, X-ray emission from clusters of galaxies

[140] Sarazin, C. L. 2002, The Physics of Cluster Mergers (Springer Netherlands), 1–38, doi: 10.1007/0-306-48096-4_1

[141] Savini, F., Bonafede, A., Brüggen, M., et al. 2019, Astronomy & Astrophysics, 622, A24, doi: 10.1051/0004-6361/201833882

[142] Shimizu, M., Kitayama, T., Sasaki, S., & Suto, Y. 2003, The Astrophysical Journal, 590, 197–206, doi: 10.1086/367955

[143] Shimwell, T. W., Röttgering, H. J. A., Best, P. N., et al. 2017, Astronomy & Astrophysics, 598, A104, doi: 10.1051/0004-6361/201629313

[144] Shimwell, T. W., Tasse, C., Hardcastle, M. J., et al. 2019, Astronomy & Astrophysics, 622, A1, doi: 10.1051/0004-6361/201833559

[145] Shimwell, T. W., Hardcastle, M. J., Tasse, C., et al. 2022, Astronomy & Astrophysics, 659, A1, doi: 10.1051/0004-6361/202142484

[146] Simonte, M., Vazza, F., Brighenti, F., et al. 2022, Astronomy & Astrophysics, 658, A149, doi: 10.1051/0004-6361/202141703

[147] Smith, G. P., Kneib, J.-P., Smail, I., et al. 2005, Monthly Notices of the Royal Astronomical Society, 359, 417, doi: 10.1111/j.1365-2966.2005.08911.x

[148] Sommer, M. W., Basu, K., Intema, H., et al. 2017, Monthly Notices of the Royal Astronomical Society, 466, 996, doi: 10.1093/mnras/stw3015

[149] Stuardi, C., Bonafede, A., Rajpurohit, K., et al. 2022, Astronomy & Astrophysics, 666, A8, doi: 10.1051/0004-6361/202244179

[150] Sunyaev, R. A., & Zeldovich, I. B. 1980, Annual Review of Astronomy and Astrophysics, 18, 537, doi: 10.1146/annurev.aa.18.090180.002541

[151] Tasse, C., Shimwell, T., Hardcastle, M. J., et al. 2021, Astronomy & Astrophysics, 648, A1, doi: 10.1051/0004-6361/202038804

[152] Timmerman, R., van Weeren, R. J., McDonald, M., et al. 2021, Astronomy & Astrophysics, 646, A38, doi: 10.1051/0004-6361/202039075

[153] Vacca, V., Murgia, M., Govoni, F., et al. 2012, Astronomy & Astrophysics, 540, A38, doi: 10.1051/0004-6361/201116622

[154] van Haarlem, M. P., Wise, M. W., Gunst, A. W., et al. 2013, Astronomy & Astrophysics, 556, A2, doi: 10.1051/0004-6361/201220873

[155] van Weeren, R. J., de Gasperin, F., Akamatsu, H., et al. 2019, Space Science Reviews, 215, doi: 10.1007/s11214-019-0584-z

[156] van Weeren, R. J., Röttgering, H. J. A., Brüggen, M., & Cohen, A. 2009, Astronomy & Astrophysics, 508, 75–92, doi: 10.1051/0004-6361/200912501

[157] van Weeren, R. J., Brunetti, G., Brüggen, M., et al. 2016, The Astrophysical Journal, 818, 204, doi: 10.3847/0004-637x/818/2/204

[158] van Weeren, R. J., Shimwell, T. W., Botteon, A., et al. 2021, Astronomy & Astrophysics, 651, A115, doi: 10.1051/0004-6361/202039826

[159] Vazza, F., Brunetti, G., & Gheller, C. 2009, Monthly Notices of the Royal Astronomical Society, 395, 1333–1354, doi: 10.1111/j.1365-2966.2009.14691.x

[160] Vazza, F., Brunetti, G., Gheller, C., Brunino, R., & Brüggen, M. 2011, Astronomy & Astrophysics, 529, A17, doi: 10.1051/0004-6361/201016015

[161] Vazza, F., Roediger, E., & Brüggen, M. 2012, Astronomy & Astrophysics, 544, A103, doi: 10.1051/0004-6361/201118688

[162] Venturi, T., Giacintucci, S., Dallacasa, D., et al. 2008, Astronomy & Astrophysics, 484, 327–340, doi: 10.1051/0004-6361:200809622

[163] Vikhlinin, A., Kravtsov, A., Forman, W., et al. 2006, The Astrophysical Journal, 640, 691–709, doi: 10.1086/500288

[164] Weißmann, A., Böhringer, H., Šuhada, R., & Ameglio, S. 2013, Astronomy & Astrophysics, 549, A19, doi: 10.1051/0004-6361/201219333

[165] Wen, Z. L., Han, J. L., & Yuan, Z. S. 2024, A catalogue of merging clusters of galaxies: cluster partners, merging subclusters, and post-collision clusters. https://arxiv.org/abs/2406.00652

[166] Wilber, A., Brüggen, M., Bonafede, A., et al. 2019, Astronomy & Astrophysics, 622, A25, doi: 10.1051/0004-6361/201833884

[167] Willson, M. A. G. 1970, Monthly Notices of the Royal Astronomical Society, 151, 1, doi: 10.1093/mnras/151.1.1

[168] Yuan, Z. S., Han, J. L., & Wen, Z. L. 2015, The Astrophysical Journal, 813, 77, doi: 10.1088/0004-637x/813/1/77

[169] —. 2022, Monthly Notices of the Royal Astronomical Society, 513, 3013–3021, doi: 10.1093/mnras/stac1037

[170] Zhuravleva, I., Churazov, E., Schekochihin, A. A., et al. 2014, Nature, 515, 85–87, doi: 10.1038/nature13830

[171] ZuHone, J. A., Brunetti, G., Giacintucci, S., & Markevitch, M. 2015, The Astrophysical Journal, 801, 146, doi: 10.1088/0004-637x/801/2/146

[172] Zwicky, F. 1933, Helvetica Physica Acta, 6, 110